Hubble Space Telescope

Wide Field - Planetary Camera Instrument Handbook

Version 3.0

April 1992

Authors: John W. MacKenty, Richard E. Griffiths, William B. Sparks, Keith Horne, Roberto Gilmozzi, Shawn P. Ewald, Christine E. Ritchie, Sylvia M. Baggett, Lisa E. Walter, and Glenn Schneider.

Contents

Figures

Tables

1.0 INTRODUCTION

1.1 Brief Historical Background of the WF/PC

The development and construction of the Wide Field and Planetary Camera (WF/PC) was led by Prof. J. A. Westphal, Principal Investigator, of the California Institute of Technology. The Investigation Definition Team (IDT) also included J. E. Gunn (deputy P. I.), W. A. Baum, A. D. Code, D. G. Currie, G. E. Danielson, T. F. Kelsall, J. A. Kristian, C. R. Lynds, P. K. Seidelmann, and B. A. Smith. The instrument was built at the Jet Propulsion Laboratory, Caltech.

The WF/PC is a dual two-dimensional spectrophotometer with rudimentary polarimetric and transmission-grating capabilities. The instrument was designed to operate from 1150Å to 11,000Å with a resolution of 0.1 arcsec per pixel (wide field camera, f/12.9) or 0.043 arcsec per pixel (planetary camera, f/30) using an array of CCD detectors.

The WF/PC was launched aboard the HST in 1990 and is currently scheduled to be replaced by WF/PC II during the first Maintenance and Servicing Mission presently planned for late 1993.

Following the launch of HST the WF/PC underwent an initial checkout period, obtained the "First Light" images of the HST, and was central to the discovery and characterization of the OTA spherical aberration. In December 1990, the WF/PC detectors were conditioned (UV flood procedure) in preparation for the scientific observing program. During 1991 Science Verification (SV) tests and calibration data were obtained by the IDT concurrent with the Cycle 0 GTO science observations. Starting in mid-1991, GO science observations also become a significant part of the usage of the WF/PC.

The engineering handover of the WF/PC from JPL to the STScI was completed in November 1991. Observations for the IDT's SV program were completed in January 1992 and the formal SV Report delivered in February 1992. The ongoing STScI calibration program began during the fall of 1991.

1.2 Sources of Additional Information

The material contained in this Handbook is derived both from ground tests conducted by the WF/PC IDT and the engineering team at JPL and in-flight testing and calibration by the IDT, JPL, and the STScI. Other pertinent sources of information include:

1: HST Phase II Proposal Instructions (Version 4.0 January 1992).*

2: Wide Field/Planetary Camera Final Orbital/Science Verification Report (1992, S.M. Faber, editor). [Hereafter: IDT OV/SV Report]*

3: STSDAS Calibration Guide (November 1991).*

4: Lauer, T., "The Reduction of WF/PC Camera Images",1989, *P.A.S.P.* 101, 445.

4. Burrows, C.J., et al., "The Imaging Performance of the Hubble Space Telescope", 1991, *Ap.J. Lett.* 369, L21.

5. Interface Control Document (ICD) 19, "PODPS to SDAS"

6. Interface Control Document (ICD) 47, "PODPS to Calibration Database"

* These documents may be obtained from the STScI User Support Branch (USB).

The STScI Telescope and Instruments Branch (TIB) writes technical reports on the calibration and performance of the Science Instruments. Announcements of these reports appear on the STEIS electronic bulletin board system and are available by writing to the TIB Secretary. Questions relating to the scientific use and the calibration of the WF/PC may be directed to the STScI WF/PC Instrument Scientists as identified in the current "STScI Contacts List."

1.3 Organization of this Handbook

A brief description of the instrument is contained in Section 2, with a more detailed description of its individual components and parameters in Section 3. The performance of the instrument is described in Section 4. The details necessary to formulate an observing proposal are described in Section 5, using the information supplied in Sections 3 and 4. Data products and standard calibration methods are briefly summarized in Section 6. The Section and Sub-Section names and numbers have been retained from Version 2.1 because of the large number of cross references from other STScI documents. The Table and Figure numbers have been revised because of the large number of changes in Version 3.0.

The information contained in this document summarizes the performance of the WF/PC as known in April 1992 and supersedes all earlier versions of this Handbook.

1.4 Revision History

Version 1.0	October 1985	Edited by Richard Griffiths
Version 2.0	May 1989	Edited by Richard Griffiths
Version 2.1	May 1990	Edited by Richard Griffiths

2.0 INSTRUMENT OVERVIEW

2.1 BRIEF DESCRIPTION OF SCIENCE OBJECTIVES

The scientific objectives of the Wide Field and Planetary Camera (WF/PC) are to provide photometrically and geometrically accurate, multiband images of astronomical objects over a relatively wide field-of-view (FOV), with high angular resolution across a broad range of wavelengths.

The discovery of significant spherical aberration in the HST Optical Telescope Assembly (OTA) subsequent to the launch of the HST has severely compromised the expected capabilities of the WF/PC. Due to the central role in the overall HST mission of the WF/PC, a second version of the WF/PC was in the early stages of construction at JPL at the time of HST launch. Since the WF/PC optical design reimages the OTA focal plane, modification of the internal WF/PC optics can correct for the spherical aberration and restore most of the originally expected performance of the WF/PC. As of April 1992, construction of this camera, now known as "WF/PC II", is well advanced and installation in the orbiting HST is expected in late 1993.

2.2 OVERALL INSTRUMENT DESCRIPTION

The Wide-Field and Planetary Camera, illustrated in Figure 2.1, occupies the single radial bay allocated to a scientific instrument. Its field of view is centered on the optical axis of the telescope and it therefore receives the highest quality images. The WF/PC operates in two basic configurations. The Wide-Field Camera (WFC) at f/12.9 provides a field-of-view of 2.57 x 2.57 arc minutes with each 15 μm detector pixel subtending 0.10 arc seconds on the sky. In the Planetary Camera (PC) at f/30, the field-of-view is 66 x 66 arc seconds, and each pixel subtends 0.043 arc seconds. The WFC undersamples the point-spread function of the optical telescope assembly (OTA) by a factor of ~2 in the visible to provide an adequate field-of-view for studying galaxies, clusters of galaxies, etc. The PC has a resolution in the visible nearly at the OTA limit, a field-of-view that is more than adequate to provide full-disk images of the planets, and a focal ratio which permits the short exposure times required for some observations. It should be emphasized that the planetary camera has numerous extra-solar applications, including studies of galactic and extra-galactic objects in which high angular resolution and excellent red-light sensitivities are needed. The WF/PC can be used as the prime instrument, as a target acquisition 'finder,' and also for parallel observations.

Figure 2.1 Wide Field/Planetary Camera Concept Illustration

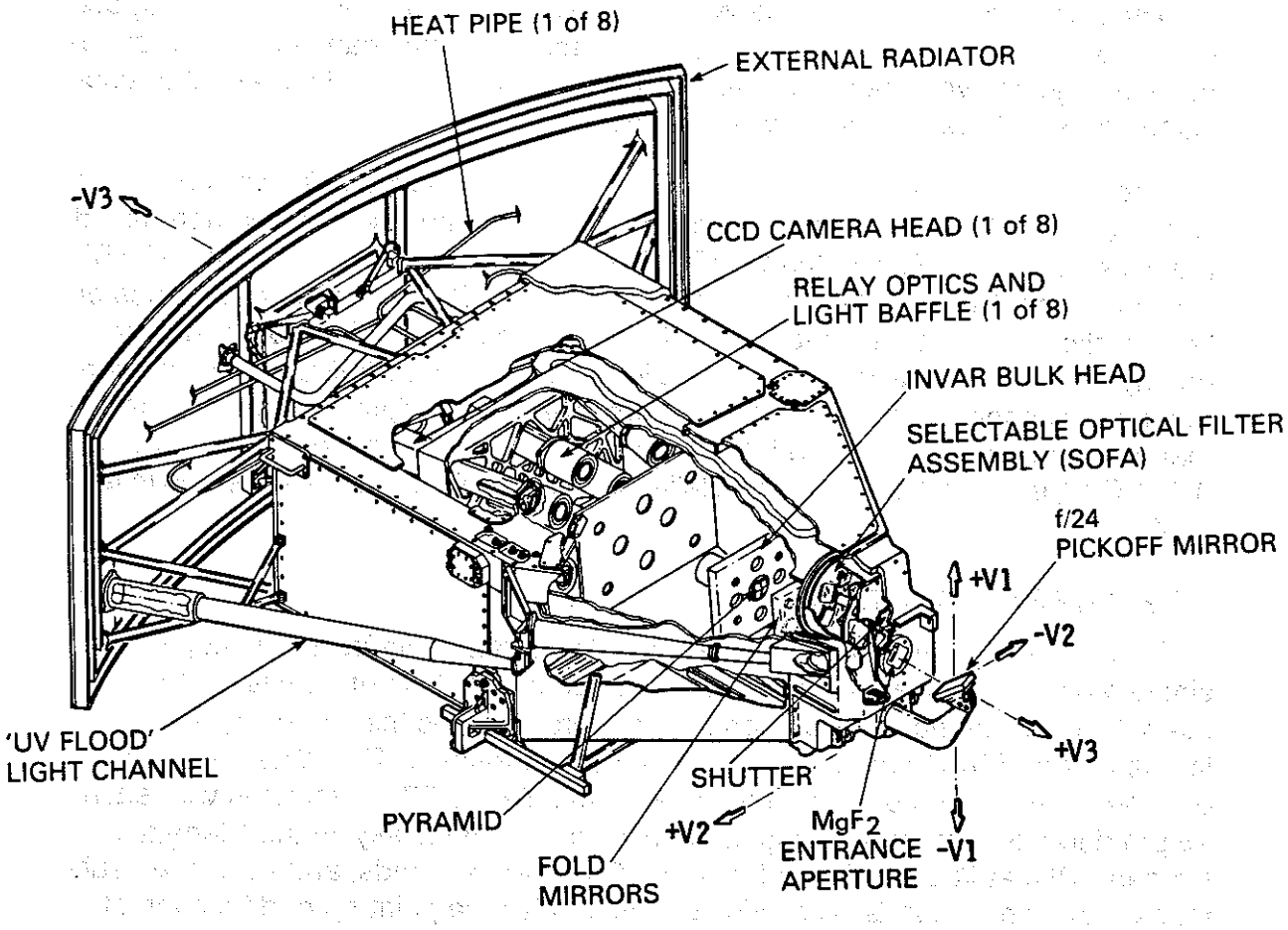

Figure 2.2 shows the optical arrangement (not to scale) of the WF/PC. The central portion of the OTA f/24 beam is intercepted by the pick-off mirror that is attached to the WF/PC and is diverted through an entry port into the instrument. For contamination control, the entry port is sealed with an afocal MgF_2 window. The beam then passes through an opened shutter and is reduced in spectral content by a filter or is dispersed by an objective grating or is analyzed for linear polarization by a polarizing filter. A total of 48 such elements are contained in a filter wheel assembly. The beam then falls on a shallow-angle, four-faceted pyramid located at the OTA focus, each face of the pyramid being a concave spherical surface. The pyramid divides the OTA image of the sky into four parts: after leaving the pyramid, each quarter of the full field-of-view is relayed by an optical flat to a Ritchey-Chretien repeater that forms a second field image on a charge-coupled device (CCD) of 800 x 800 pixels. Each detector is housed in a cell that is sealed by a MgF_2 window. This window is figured to serve as a field flattener. At the edge of the field-of-view (i.e., in the worst case) the computed modulation transfer func-

tion (MTF) of this optical system for the wide-field mode, combined with that of a diffraction-limited OTA at visible wavelengths, is 44% in the radial direction and 32% in the tangential direction at the 33 cycles mm^{-1} sampling frequency of the CCD detector.

Figure 2.2 WF/PC Optical Configuration

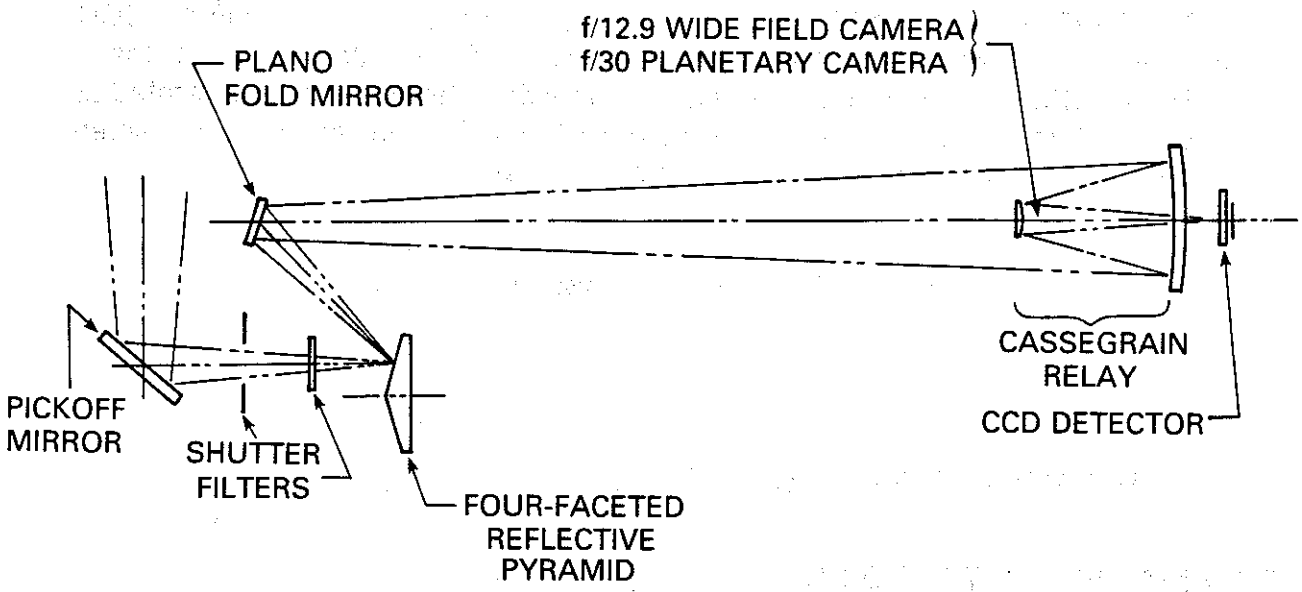

After a selected integration time (≥ 0.11 seconds), the camera shutter is closed, and the full 1600 x 1600 pixel field-format may be recovered by reading out and assembling the outputs from the four CCDs fed by the pyramid. Alternatively, any combination of 1, 2 or 3 CCDs may be read out in numerical order. In each configuration (WFC or PC) the CCDs are physically oriented and clocked such that the pixel readout direction is rotated approximately 90° in succession (see figure 3.5). The (1,1) pixel of each CCD array is thereby located near the apex of the pyramid. As a registration aid in assembling the four frames into a single picture, a light can be turned on at the pyramid to form a series of eleven fixed artificial "stars" (known as Kelsall spots or 'K'-spots) along the boundaries of each of the mosaic quadrants. This calibration is done in a separate exposure, because light also shines through the neutral-density or 'Baum' spot, causing blooming and residual image.

In total, the WF/PC contains eight relay mirror-repeater-CCD trains, four for the wide-field camera and four for the planetary camera. To place the desired camera into operation, the pyramid is commanded to rotate into one of two fixed orientations, separated by 45°. The pyramid can also be moved along the WF/PC optical axis if required to bring the WF/PC to a common focus with the other HST Science Instruments. As of April 1992, it is not expected that this feature will be used.

Each CCD is a thinned, backside-illuminated, silicon sensor, fabricated by Texas Instruments and clocked with 3 phases. A CCD, mounted on its header, is hermetically packaged in a ceramic-tube body that is filled with 0.1 atmosphere absolute of argon and sealed with a MgF_2 field flattener. This complete cell is connected with compliant silver straps to the cold junction of a thermoelectric cooler (TEC). The hot junction of the TEC is connected to the radial bay external radiator by an ammonia heat pipe. This sensor-head assembly is shown in Figure 2.3. During operation, each TEC cools its sensor package to a selected temperature of -82, -87, -92, -97, -102, -107, -111, or -115 °C to suppress dark current in the CCD to a level that does not inhibit long integration times. Prior to January 1991, the WF/PC CCDs were operated at -97°C; since that time they have been operated at a temperature of -87 °C. A readout noise of ~13 rms electrons $pixel^{-1}$ is characteristic of these CCDs with their associated signal chains.

Figure 2.3 Cooled Sensor Assembly

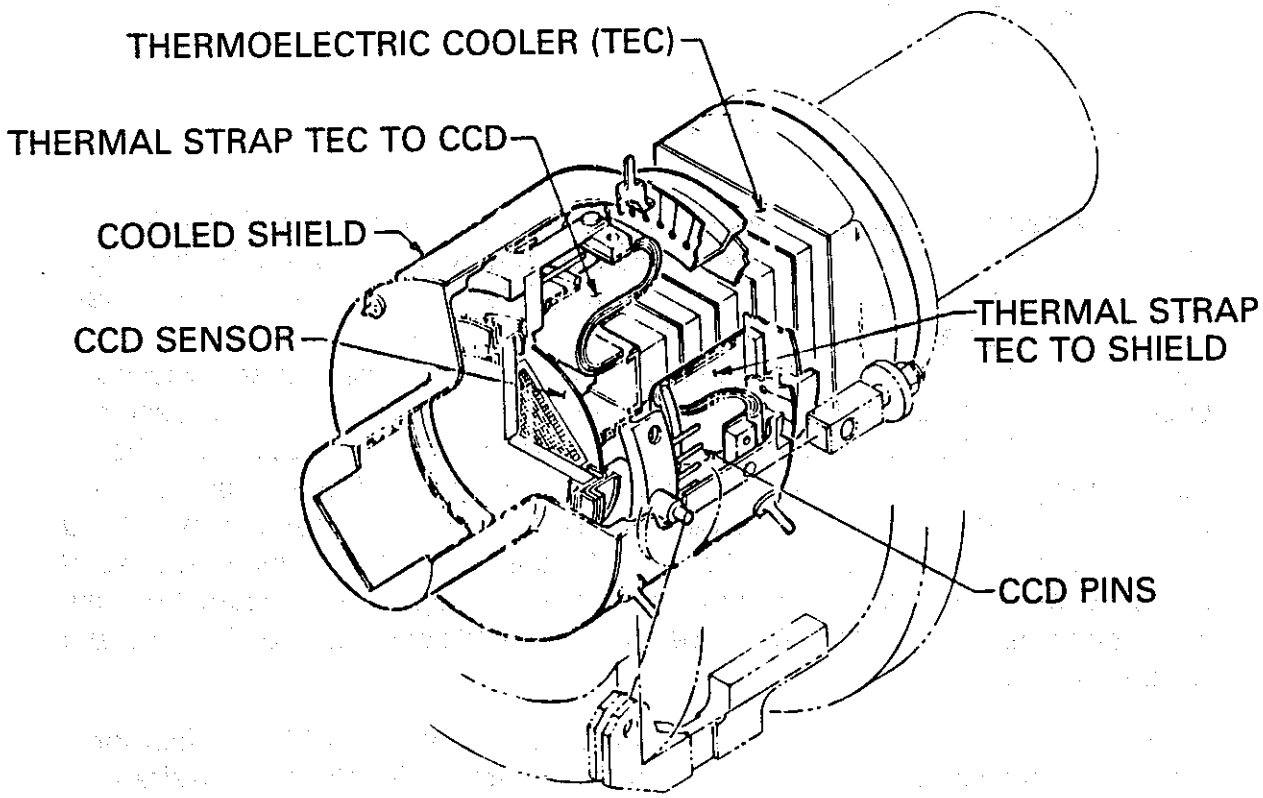

The WF/PC provides a useful sensitivity from 1150Å to 11000Å in the same detector. Specifically, the full throughput detective quantum efficiency of the instrument (exclusive of filters) is shown in Figure 4.1. The visible and red sensi-

tivity of the WF/PC is a property of the thickness of the silicon from which the CCDs are fabricated (~8μm). To achieve good ultraviolet response each CCD is coated with a thin (≈160 nm) film of coronene, an organic phosphor. Coronene converts photons with wavelengths ≤3800 Å into visible photons with wavelengths peaked near 5200 Å. The CCD detects these visible photons with good sensitivity. Longward of 3800 Å, the coronene becomes transparent and acts to some degree as an antireflection coating. Thus, the full wavelength response is determined by the MgF_2 cutoff on the short-wavelength end, and the silicon band-gap in the infra-red at 1.1 eV (~11000 Å).

With such CCD sensors, images may be obtained in any spectral subregion defined by the chosen filter with high photometric quality, wide dynamic range, and excellent spatial resolution. The bright end of the dynamic range is limited by the 0.11 seconds minimum exposure time, and by the saturation level of the analog to digital converter, which has been set electronically to about 30,000 electrons per pixel. The bright end of the dynamic range can be extended by using the low-reflectance spot (approximately 1.23 arc seconds in diameter) which has been placed on one of the four pyramid faces (see section 3.3; the OTA spherical aberration greatly reduces the utility of this element of the WF/PC design). The faint end is limited by photon noise, instrument noise, and, for the wide-band visible and infra-red filters, the sky background. The minimum signal-to-noise ratio corresponding to a fully exposed pixel will be about 200.

Table 2.1 gives characteristic values of the expected dynamic range in visual magnitudes for point sources, in the absence of the OTA Spherical Aberration. The minimum brightness is given for a S/N ratio of 3, and the maximum corresponds to full well. The quoted values assume an effective bandwidth of 900Å centered on 5500Å. The effect of the OTA spherical aberration is to decrease (in magnitudes) all of these values by 2 to 3 magnitudes in a manner dependent upon the source morphology and other sources in the scene which lie within the extended point spread function (see also Section 4.5.1).

Note that, because the Planets are not point sources, they will be observable with short exposure times even though their integrated brightness may greatly exceed the 8.4 magnitude limit.

Table 2.1 Dynamic Range in a Single Exposure without OTA Aberration

Configuration	Exposure (seconds)	Min. V Magnitude	Max V. Magnitude
Wide Field	0.11	9.3	16.6
Wide Field	3000.	20.4	27.5
Planetary	0.11	8.4	16.0
Planetary	3000.	19.5	27.0

3.0 INSTRUMENT DESCRIPTION

3.1 WF/PC CONFIGURATIONS, FIELDS OF VIEW AND RESOLUTION

The fields of view and angular resolutions of the wide field and planetary cameras are approximately as follows:

Camera	Pixel and CCD Format	Field of View	Pixel Scale	f/ratio
Wide Field	800 x 800 x 4 CCDs	2.6 x 2.6 arc minutes	100 mas	12.9
Planetary	800 x 800 X 4 CCDs	66 x 66 arc seconds	43 mas	30

Calibration of the WF/PC pixel scale on-orbit yields 0.1016″± 0.0001″ for the WFC and 0.0439″± 0.0001″ for the PC (IDT OV/SV Report; Chapter 7).

3.2 OPTICAL FILTERS AND SPECTRAL ELEMENTS

The optical filters define the spectral bandpass of light which is allowed to reach the CCDs. The filters are located within the Selectable Optical Filter Assembly (SOFA) placed between the shutter and the reflecting pyramid. The SOFA contains 12 filter wheels, each of which has 4 filters and a clear "home" position. A listing of all optical elements in the SOFA mechanism and the location of each element (by wheel number 1 –12, and position A – D) is shown in Table 3.1. Wheel number 1 is located closest to the WF/PC shutter.

Each of the Type "A" filters is equivalent to 5mm of quartz in terms of optical path length, with compensation for wavelength such that focus is maintained on the CCDs. A configuration with no filters in the beam results in out-of-focus images and will not generally be used. With the exception of the Polarizers and the Neutral Density (Type "B") filters, all filters are designed to be used alone — combinations of Type "A" filters will result in out-of-focus images.

The three basic categories of spectral elements are as follows:

Filters (F)

These include long-pass (LP), wide (W), medium (M), narrow (N), or Neutral density (ND). Most of these filters are either flat single substrates or sandwiches. The Neutral Density filter (F8ND) provides 7.5 magnitudes of attenuation (i.e. a factor of 1000) and is designed for use in combination with a Type "A" filter.

Polarizers (POL)

Relative polarization angles of 0°, 60° and 120° are available (Table 3.1). The polarizers are constructed with curved substrates, and should be used with any one of the Type A filters, over the wavelength range from 2800Å to 8000Å.

Gratings (G)

A limited spectroscopic capability is provided by transmission gratings mated to wedged substrates or prisms (i.e. "grisms"). The blue and red gratings have prismatic substrates wedged in one dimension only, and therefore produce linear spectra. The UV grating is wedged along two orthogonal axes and thus produces cross-dispersed spectra which are partially overlapped due to the OTA spherical aberration.

Table 3.1 Filter Elements

NAME	TYPE	WHEEL/ HOLE	$\bar{\lambda}$ (Å)		Δλ (Å)	PEAK T (%)	PEAK λ (Å)
F122M	B	2-A	2329	RED LEAK	2824	15.5	1200
F128LP	A	11-A	1275	CaF_2 LP		92.5	
F157W	B	4-A	1682		1019	16.3	1455
F194W	B	4-B	1961		436	17.5	1870
F230W	A	4-C	2313		366	21.5	2220
F284W	A	4-D	2814		524	23.7	2820
F336W	A	2-B	3360		411	51.7	3346
F368M	A	8-A	3687		230	37.2	3577
F375N	A	7-A	3755	3727 RS	82	37.1	3734
F413M	A	8-B	4125		248	56.3	4090
F437N	A	7-C	4366	[OIII]	22	46.3	4366
F439W	A	2-C	4352		465	60.3	4094
F469N	A	11-B	4687	HeII	27	56.8	4688
F487N	A	11-C	4869	Hβ	31	55.7	4867
F492M	A	8-D	4906		364	60.9	4712
F502N	A	7-B	5018	[OIII]	29	60.3	5016
F517N	A	11-D	5170	C_2, MgII	87	62.1	5155
F547M	A	9-A	5454		438	64.8	5418
F555W	A	9-B	5416		1205	91.5	5150
F569W	A	5-A	5598		967	90.1	5320
F588N	A	7-D	5880	HeI, NaD	43	54.6	5877

Table 3.1 Filter Elements

NAME	TYPE	WHEEL/ HOLE	$\bar{\lambda}$ (Å)		$\Delta\lambda$ (Å)	PEAK T (%)	PEAK λ (Å)
F606W	A	12-B	5844	Wide V	1553	95.4	6444
F622W	A	8-C	6140		964	96.5	6030
F631N	A	6-A	6306	[OI]	29	43.5	6310
F648M	A	9-C	6469		371	53.1	6467
F656N	A	6-B	6559	Hα	19	40.9	6559
F658N	A	5-D	6576	[NII]	20	41.2	6577
F664N	A	6-C	6637	Hα RS	131	53.9	6634
F673N	A	1-A	6723	SII	50	83	6731
F675W	A	5-B	6684		910	94.9	6753
F702W	A	6-D	6898		1493	97.1	6920
F718M	A	9-D	7160		595	55.5	7120
F725LP	A	12-C	8496	(7320) LP	1987	90.0	
F785LP	A	10-C	8922	(7850) LP	1571	95.6	
F791W	A	5-C	7906		1322	86.4	7556
F814W	A	10-A	8137		1768	93.9	8580
F850LP	A	12-A	9298	(8600) LP	1153	93.0	
F875M	A	10-B	8762		556	88.5	8747
F889N	A	12-D	8888	CH_4	51	83.5	8884
F1042M	A	10-D	10167		481	91.4	10828
F1083N	A	3-D	10831	HeI	80	59.2	10847
F8ND	B	1-B	7.5 mag Neutral Density			00.1	
POL0	B	3-A	Polarizer 0°				
POL60	B	3-B	Polarizer 60°				
POL120	B	3-C	Polarizer 120°				

Table 3.1 Filter Elements

NAME	TYPE	WHEEL/ HOLE	$\bar{\lambda}$ (Å)	$\Delta\lambda$ (Å)	PEAK T (%)	PEAK λ (Å)
G200		2-D	UV Grating	1600-4000 1300-2000		
G450		1-C	Blue Grating	3000-6000		
G800		1-D	Red Grating	6000-10000		

Notes:

F = filter
POL = polarizer (must be used with a filter for focus)
G = grating (most be used by itself for focus)
LP = longwavelength pass
RS = red shifted
N means <3% (FWHM / Effective Wavelength).
M means between 3% to 15% (FWHM / Effective Wavelength).
W means >15% (FWHM / Effective Wavelength).

The number given in parenthesis for LP is the 50% cut-on point. The mean wavelength is similar to that defined in Schneider, Gunn and Hoessel (Ap. J. 264, 337) – see Section 5.1. It includes the CCD QE and the transmission of OTA, WF/PC and filters (based on pre-launch values). The width is the FWHM of a Gaussian filter with the same second moment and is reasonably close to the FWHM.

The WF/PC is designed to permit coverage of a wide spectral range. Figure 3.1 summarizes the normalized transmission curves for narrow, medium and wide-band spectral filters. Filter transmission curves are shown in the Appendix in Figures A.1 (filters alone) and A.2 (system response included). A few of the curves required extrapolation to zero in the wings and removal of extraneous non-real wing spikes.

Figure 3.1 Normalized Spectral Response Curves

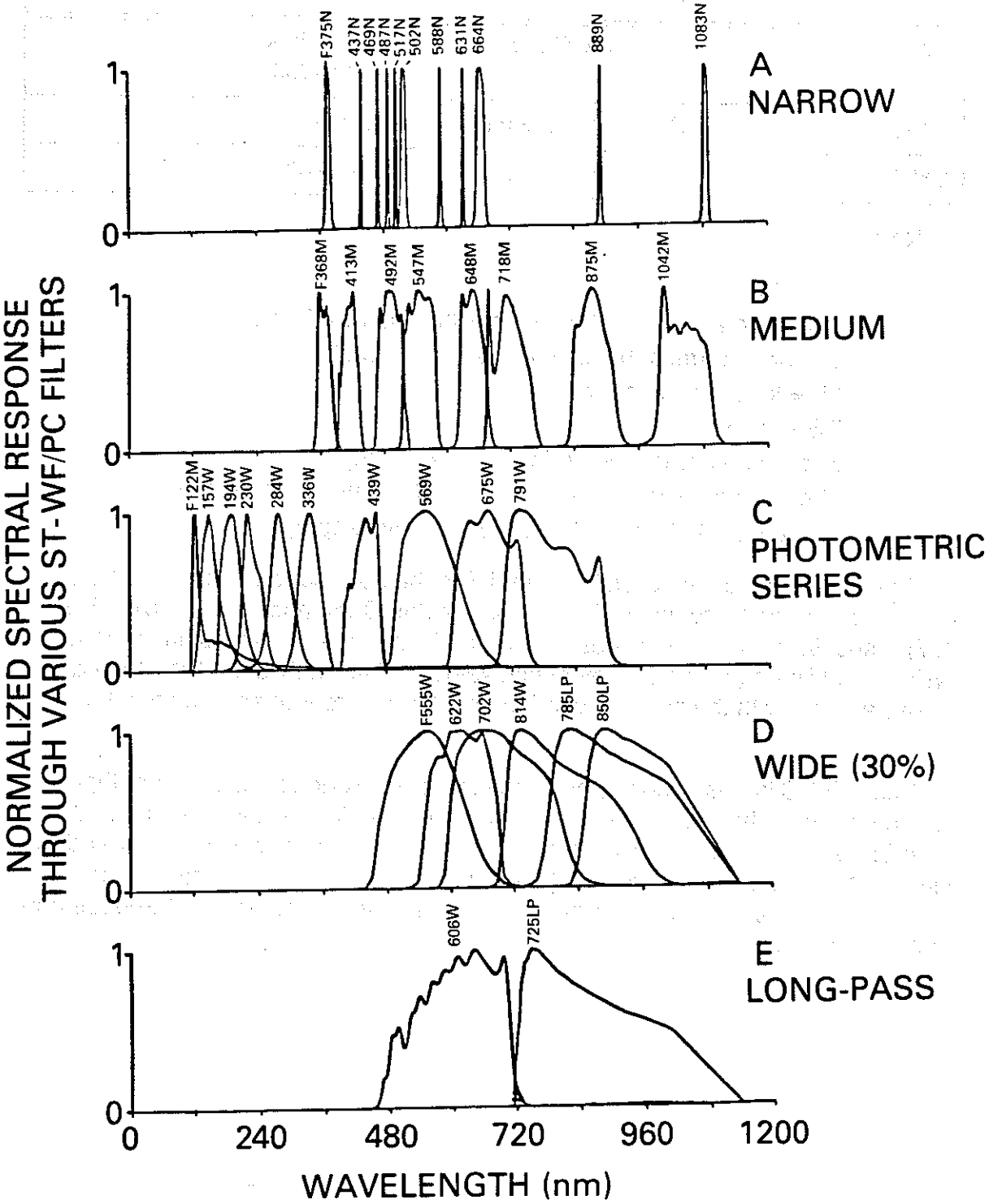

Figure 3.1 divides the filters into the following groups:

(A) Narrowband filters for isolating individual spectral lines or bands. An Hα filter (for z ~ 0) at 656 nm and an N [II] filter at 658 nm have been omitted from the plot to avoid graphical crowding.

(B) Mediumband filters with FWHM ~10% of the central wavelength. Note that F368M and F413M cover the region of falling coronene response and increasing silicon response. Their usefulness, therefore, depends on the success of UV flood and the absence of hysteresis.

(C) A photometric set including approximations to UBVRI passbands and extending that series in the ultraviolet down to Ly α (see Harris et al. 1991, *A.J.* **101**, 677). Note, however, that the WF/PC UBVRI series is not the Johnson photometric series. In particular, the CCD response in the U and B bands is a strong function of wavelength, so that differences from Johnson U and B may be large. F439W spans the region of CCD response in the critical region where silicon absorption length is changing rapidly with wavelength; its response is, therefore, improved by UV flood, and is particularly subject to any remaining hysteresis.

(D) Wideband filters with FWHM ~25% of the central wavelength.

(E) "Wide-V" and "Wide-I."

Not shown is the pure CaF_2 filter whose response function resembles Figure 4.1 except for cutting off Ly α at the extreme left end. (Also not shown are the three afocal Polaroids and the three grisms.)

The WFC CCDs view essentially the full dimensions of any given filter. The PC CCDs, however, see only the central portion of any filter. This is a consequence of that camera's narrowed field of view. This narrower field is skewed 45° with respect to the wide field when the pyramid is rotated to switch the incoming image to the PC (see Figure 3.5).

Note that the UV filters have some degree of "red leak". These are quantified in Table 4.3 and illustrated in Figure 4.6 for F122M, F157W, F194W, F230W and F284W.

The transmission of the three polarizers (POL0, POL60, and POL120) is shown in Figure 3.2. The polarizers are afocal and must therefore be used in combination with another filter which largely defines the shape of the passband. An observation without any filters in the beam would result in an out-of-focus image.

Figure 3.2 Polarizer Transmission

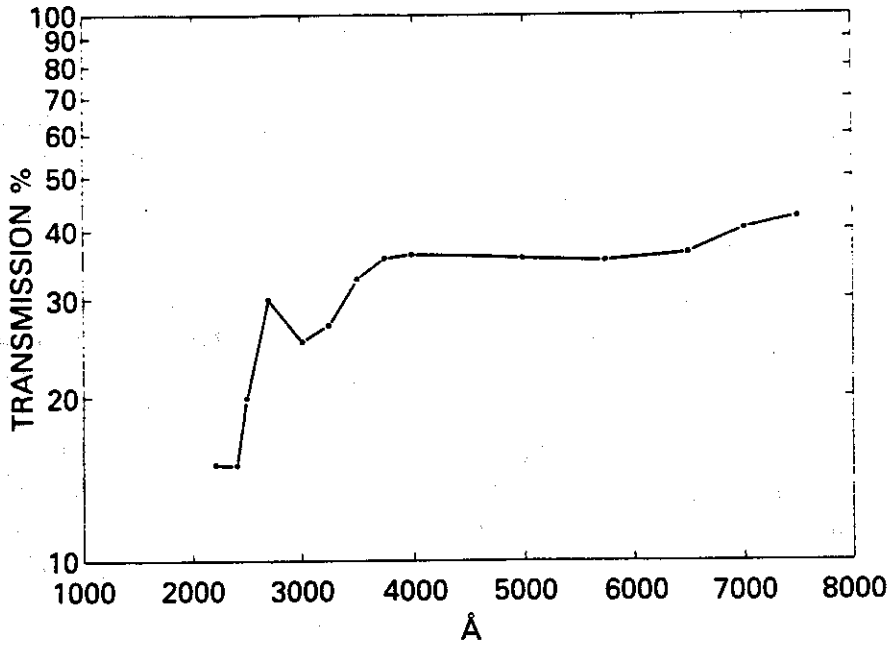

Throughput curves for the gratings (figure A.3) include the blaze envelope as well as OTA, WF/PC optics and CCD response. The grating dispersions, which are optimized for the WFC, are listed in Table 3.2. The zero order image can be used as a wavelength fiducial with any of the gratings.

For the second order UV grating, if d is the groove spacing, N is the order, and n is the index of refraction of the CaF_2 substrate, the equation for the position of the image at λ for an axial star, measured along the direction of dispersion and at right angles to the dispersion, respectively, is given by

$$x_{\|} = D\theta_{\|} = D\left(\frac{N\lambda}{d} - (n-1)\,\Upsilon\right)$$

$$x_{\perp} = D\theta_{\perp} = D\,(n-1)\,\zeta$$

where D is the distance between the grating and the focal plane = 277 mm, $\Upsilon = 0.727°$ is the wedge angle in the dispersion direction, $\zeta = 0.47°$ is the wedge angle across the dispersion, $d = 0.04$ mm, and n is the refractive index.

The spectra will have displacements in pixels of

$$P_{\|} = \frac{D\theta_{\|}}{P} = 0.025\lambda N - 125\,(n-1)$$

$$P_{\perp} = \frac{D\theta_{\perp}}{P} = 80\,(n-1)$$

where ***P*** is the WFC pixel size projected back to the OTA focus on the WF/PC pyramid (28 μm). The template for the spectra is illustrated in Figure 3.3.

Table 3.2 Grating Properties

Grating		G200 (UV)	G450 (Blue)	G800 (Red)
Substrate		CaF_2	BG–38	OG–570
Blaze angle (rads)		0.01269	0.0152	0.0137
Lines mm		25	16.2	8.22
Focal Distance (mm)		277	287	287
Central λ (Å)	1st order	2400	5000	8850
	2nd order	1500		
Wavelength Range (Å)	1st order	1600–4000	3000–6000	6000–10000
	2nd order	1300–2000		
Dispersion Å/pixel (WFC)	1st order	15.0	55.5	110.8
	2nd order	12.1		
Peak Efficiency	1st order	25%	65%	65%
	2nd order	15%		

Figure 3.3 Dispersed spectra with UV grating and WFC

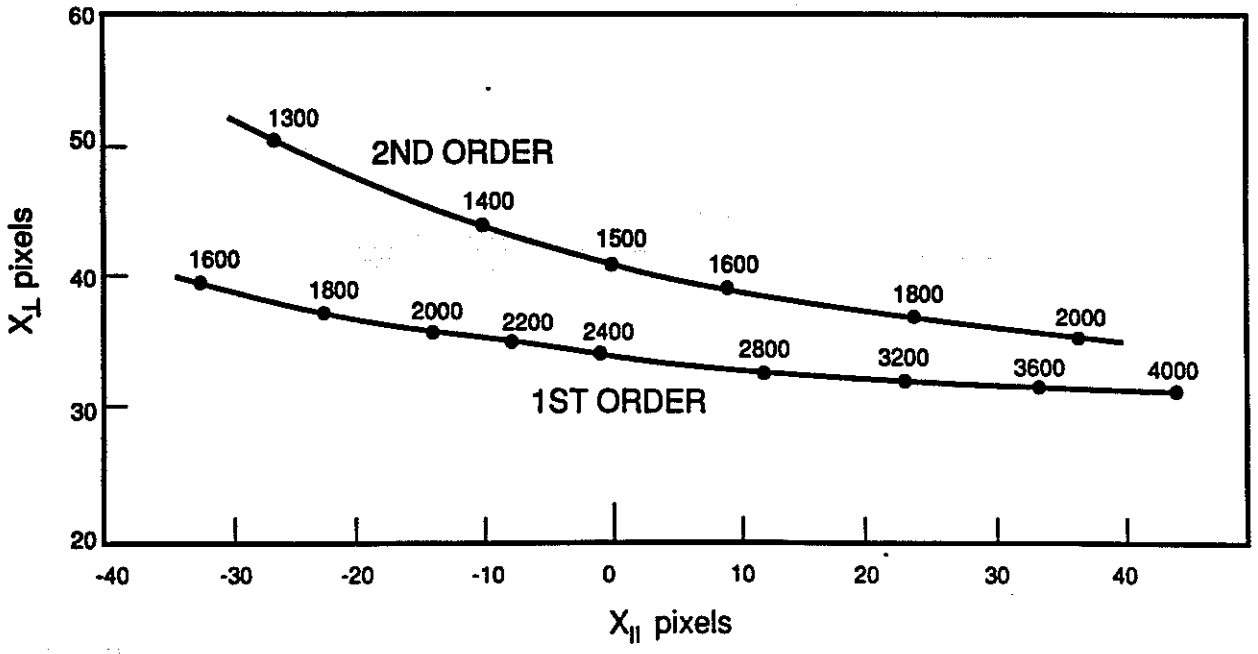

3.3 NEUTRAL DENSITY OR 'BAUM' SPOT

One facet of the pyramid has a low-reflectance spot approximately 1.23 arc seconds in diameter with a reflectance approximately 0.1 percent of the other portions of the optical surface over the wavelength range 5000Å to 7000Å. This low reflectance spot was designed to allow observation of faint images in the presence of bright point sources and to extend the useful dynamic range of one CCD in each of the wide field and planetary cameras. It appears near the center (x=416, y=417) of PC CCD 8 and at x=195, y=197 in WFC CCD 4. The prelaunch measured reflectance vs. wavelength is shown in Fig. 3.4.

In addition to its obvious impact on observations of faint targets near bright sources, the OTA Spherical Aberration greatly limits the utility of the Baum Spot because the extended PSF of a bright star may still saturate the CCDs at the edges of the spot. Consequently, the on-orbit calibration of the position, reflectance, and underlying flat field of the Baum Spot has not been undertaken.

Figure 3.4 Reflectance of the Baum Spot

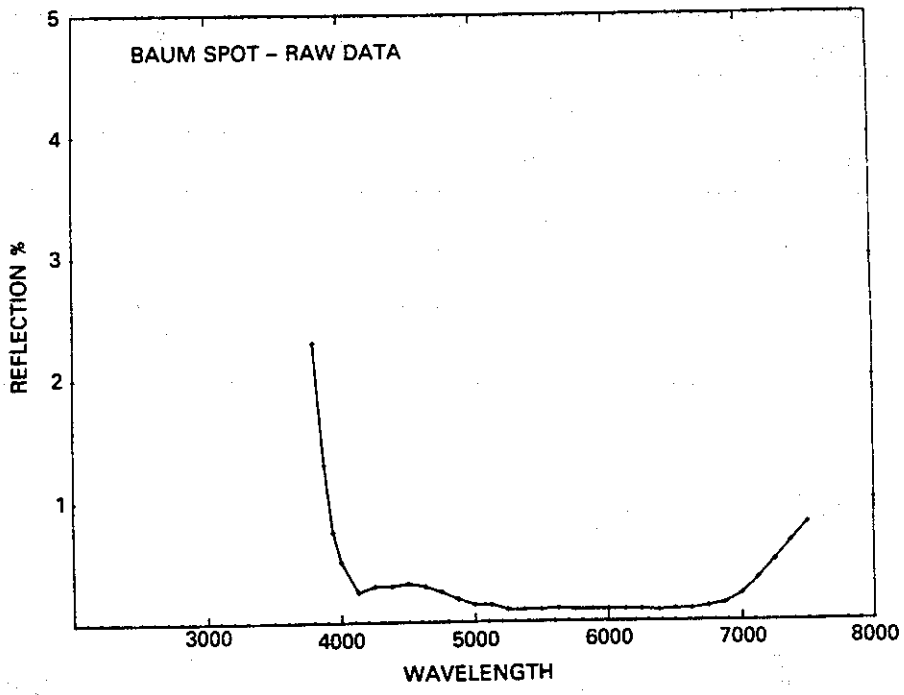

3.4 SHUTTER

The shutter is a two-blade mechanism used to control the duration of the exposure. A listing of the possible exposure times is contained in Table 3.3. These are the only exposure times which can be commanded. Current policy is to round down non-valid exposure times to the next valid value.

For the shortest exposure times, it is possible to determine the time of flight of the shutter blades. The necessary information is contained in the WF/PC engineering data stream: encoder disks, attached to the shutter blade arms, are timed by means of a photo-transistor. The accuracy of shutter timing is 5 milliseconds (average minus minimum or maximum). For short-exposure observations, it is not generally possible to repeat exposures on time scales less than 3 minutes (see section 4.7.4)

When obtaining very short exposures ($\leq$ 0.2s), diffraction effects arising from the finite time of flight of the shutter blades will affect the point spread function. Especially when using short exposures to obtain point spread functions in support of long exposure observations, it is important to use exposure times greater than or equal to 0.2s (see IDT OV/SV Report, Chapter 9 for further discussion).

The control of the initial opening of the WF/PC shutter during an observation is held by the internal WF/PC microprocessor in all cases. However, control over when the shutter is closed is held by the microprocessor only for exposures less than 300 seconds in duration. For longer exposures the control over when the shutter is closed resided with the Application Processor (AP-17) in the NSSC-1 Spacecraft computer. The consequence of this arrangement is that loss of guide star lock will result in the WF/PC shutter being closed only for those observations with planned durations longer than 300 seconds (longer than 1 second if the serial clocks on mode is selected – see 4.7.2). If guide star lock is reacquired prior to the end of the planned observation time, the shutter will re-open to obtain a portion of the planned integration times.

Table 3.3 Quantized Exposure Times (Seconds)

0.11	0.12	0.14	0.16	0.18	0.20	0.23
0.26	0.30	0.35	0.40	0.5	0.6	0.7
0.8	1.0	1.2	1.4	1.6	1.8	2.0
2.3	2.6	3.0	3.5	4.0	5.0	6.0
7.0	8.0	10.	12.	14.	16.	18.
20.	23.	26.	30.	35.	40.	50.
60.	70.	80.	100	120	140.	160.
180.	200.	230.	260.	300.	350.	400.
500.	600.	700.	800.	900.	1.0E3	1.1E3
1.2E3	1.3E3	1.4E3	1.5E3	1.6E3	1.7E3	1.8E3
1.9E3	2.0E3	2.1E3	2.2E3	2.3E3	2.4E3	2.5E3
2.6E3	2.7E3	2.8E3	2.9E3	3.0E3	3.1E3	3.2E3
3.3E3	3.4E3	3.5E3	3.6E3	3.7E3	3.8E3	3.9E3
4.0E3	4.1E3	4.2E3	4.3E3	4.4E3	4.5E3	4.6E3
4.7E3	4.8E3	4.9E3	5.0E3	5.1E3	5.2E3	5.3E3
5.4E3	5.5E3	5.6E3	5.8E3	6.0E3	6.2E3	6.4E3
6.6E3	6.8E3	7.0E3	7.5E3	8.0E3	8.5E3	9.0E3
1.0E4	1.5E4	2.0E4	2.5E4	3.0E4	4.0E4	5.0E4
7.5E4	1.0E5					

3.5 CCD ORIENTATION AND READ-OUT

The relation between the pixels and lines for the four CCDs associated with each camera is shown in Figure 3.5. The 45° difference between the WFC and PC reflects the pyramid rotational difference for the two cameras. The counts for pixels and lines increase for the indicated CCDs in the manner described in Figure 3.5. Note that each CCD is similarly sequenced, so that their axes are defined by a 90° rotation from the adjacent CCD. If a given image were displayed from all the CCDs of a given camera (with pixels in the "X" direction and lines in the "Y" direction), each successive display would appear rotated by 90° from its predecessor.

Figure 3.5 Overlay of the FOV of the WF/PC CCDs on the sky.

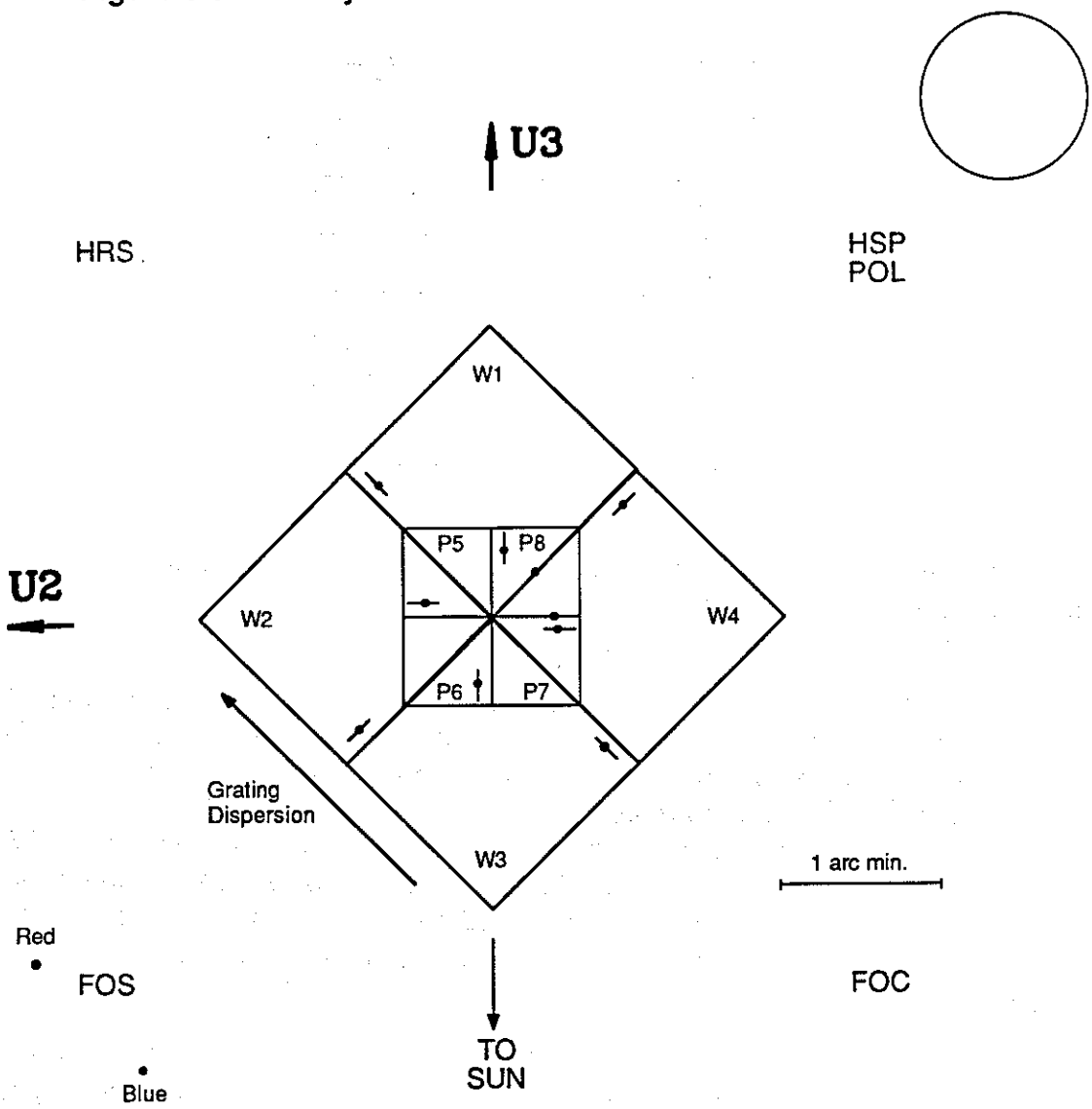

There is an optically inactive border of approximately 25 pixels along the two edges of each CCD which butt against the fields of view of neighboring CCDs. The square area completely covered on the sky by the 4-part mosaic is thus 1543 x1543 pixels in the WFC (154.5 x154.5 arc seconds) and 1531 x1531 pixels in the PC (65.8 x 65.8 arc seconds). Figure 3.5 illustrates the projected orientation of the WF/PC CCDs onto the sky. The Kelsall spots are imaged at the boundaries of the optically active and inactive areas of each CCD, where the optically active areas are approximately defined by the pixel dimensions given in Table 3.4.

U2 ~ -V2
U3 ~ -V3 / fraction of degree

Table 3.4 Optically Active Dimensions

	x	y
WF 1	783	767
WF 2	783	773
WF 3	772	770
WF 4	773	769
PC 5	767	757
PC 6	774	763
PC 7	768	771
PC 8	781	770

Registration of images from more than one CCD is aided by a series of 11 pinholes along each of the common pyramid edges ('Kelsall' spots), which can be illuminated in a special calibration exposure.

The WF/PC has two readout formats, namely full single-pixel resolution (FULL Mode), and (2 x 2) pixel summation (AREA Mode). Each line of science data is started with two words of engineering data, followed by 799 (FULL) or 400 (AREA) 16-bit positive numbers as read from the CCDs. In FULL Mode the CCD pixels are followed by12 "bias" words ("overclocked" pixels), making a total of 813 words per line for 800 lines. In AREA Mode, there are 402 words per line for 400 lines. Either pixel format may be used to read out the WFC or PC. These outputs are reformatted into the science image and extracted engineering data files during processing in the HST ground system prior to delivery to the observer.

The advantage of the AREA Mode (2 x 2) 'on-chip' pixel summation is that readout noise is maintained at 13 electrons rms for the summed (i.e., larger) pixels. This pixel summation is useful for some photometric observations of extended sources. Note, however, that cosmic ray removal may be more difficult in AREA Mode. Note also that the electronic bias is not as well determined in AREA Mode, because there are no "overclocked" or extended register pixels. For each line of data, the bias value for one pixel is contained in the engineering data, but without the least significant bit. During the first two years of HST operation, AREA Mode has rarely been used and a comprehensive calibration of this mode is not presently anticipated.

In a fundamental way, the WF/PC has a single science mode: it acts as a photometric, area imager. The Operating Mode in the Exposure Logsheet will, therefore, always read IMAGE. By choice of elements from the SOFA that are included in the light beam, however, three distinct photometric modes are permitted, *viz.*, filter photometry (using wide, medium or narrow band filters), photopolarimetry

(using a polarizer plus a filter in the 2500 Å – 8000 Å range), and slitless spectroscopy (using a transmission grating).

The direction of blooming along the columns of each CCD (see Section 4.7.2) is indicated by the bars on either side of the (saturated) solid dot. Each CCD is read out from the corner nearest the center of the diagram, with column (pixel) and row (line) numbers increasing from the diagram center. Columns and rows are parallel and orthogonal to the bar, respectively. The direction of wavelength dispersion is also indicated, when the gratings are used. Diffraction spikes caused by the Optical Telescope Assembly and by the internal Cassegrain optics of the WF/PC are parallel to the edges of the Planetary Camera CCDs. The neutral density or 'Baum' spot is at the center of PC8 and one-quarter of the way along each axis from the origin of WFC4. The default pointing positions when all 4 CCDs of each camera are used are on PC6 and WFC2, approximately 10 arc seconds along each axis from the origin.

For many observations, only the field of view of a single CCD detector is actually required. However, the default operational mode is to read out all four CCDs from the relevant camera. This may result in serendipitous discoveries, recovery of useful observations in the case of small pointing or coordinate errors, and will identify regions of saturated pixels which might have an impact on subsequent exposures.

Observations which require only the field of view of a single CCD are best made with the target placed near the center of a single CCD rather than near the center of the 4 CCD mosaic. This will result in a better point spread function. As of April 1992, the CCDs WFC2 and PC6 are the preferred detectors and are the CCDs being used in the maintenance of the photometric calibration. These CCDs have the most uniform flat fields, do not contain the "Baum" spot, and, in the presence of low level contaminants (see Section 4.7.8), are the cleanest detectors.

It is possible to command the WF/PC to read only a subset of the CCDs from either camera (but they must be read in numerical order). This does not result in a decrease in the readout overhead time (see Section 4.7.4) but does conserve limited space on the HST on-board science tape recorder. The capacity of this tape recorder is slightly over 7 full (4 CCD) WF/PC observations and 18 single CCD WF/PC observations on a single side (of two). Switching sides of the tape recorder without a pause will result in the loss of part of a single CCD readout. Since an interval of ~30 minutes normally must be allowed for the tape recorder to be copied to the ground, readout of only a subset of the WF/PC CCDs is advantageous when many frames need to be obtained in rapid succession.

Multiple exposures may be obtained with or without spacecraft motion between them followed by a readout with the restriction that the WF/PC will be read out at least once per orbit.

4.0 INSTRUMENT PERFORMANCE

4.1 QUANTUM EFFICIENCY

The overall spectral response of the system is shown in Figure 4.1 (not including filter transmissions). The data presented here represent the UV-flooded response of the CCDs and are based on observations of the spectrophotometric standard star BD+75D325 obtained in early February 1992 immediately subsequent to a decontamination of the WF/PC. At this time the on-orbit UV flood was ≈13 months old.

The quantum efficiency (QE) of the system combined with each filter is tabulated in Tables 5.1 and A.1 and shown in Figure A.3.

Compared to their unflooded state, the QE of the UV flooded CCDs is enhanced in the UV and blue with smaller improvements at $\lambda > 7000$Å. In particular, the response trough which previously existed around 4000Å is filled in for some CCDs so that the QE rises monotonically from the 2000Å – 3000Å region (where QE enhancement is relatively small following UV flood) to 6000Å, where the enhancement is again relatively small.

QE at Ly α was measured during ground tests to be less than or equal to 0.3%, several times less than the expected value. In addition to the internal contaminants (see Section 4.2.2), the Magnesium Fluoride entrance aperture has lower transmission than the design goal at Ly α.

The sensitivity of PC8 is sufficiently greater than that of the other CCDs (particularly between 3000Å and 5000Å) that, for the same exposure time, use of PC8 will give similar S/N as that from any of the WFC CCDs (if the observations are readout-noise limited). However, observers are strongly cautioned that PC8 also has the most pronounced flat field structure, the most marked changes in its flat field structure during a decontamination, and the "Baum" spot at its center. Also, when the WF/PC is in a contaminated state, the structure is strongest on PC8.

Figure 4.1 WF/PC + OTA Quantum Efficiency

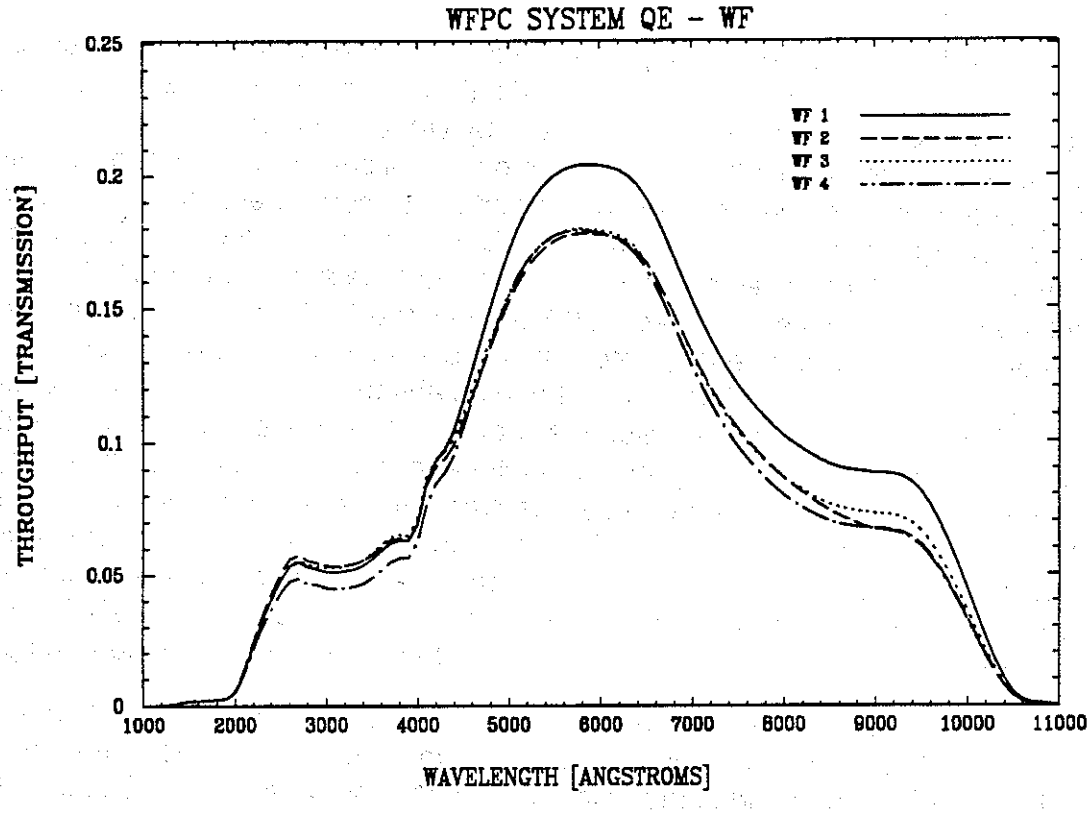

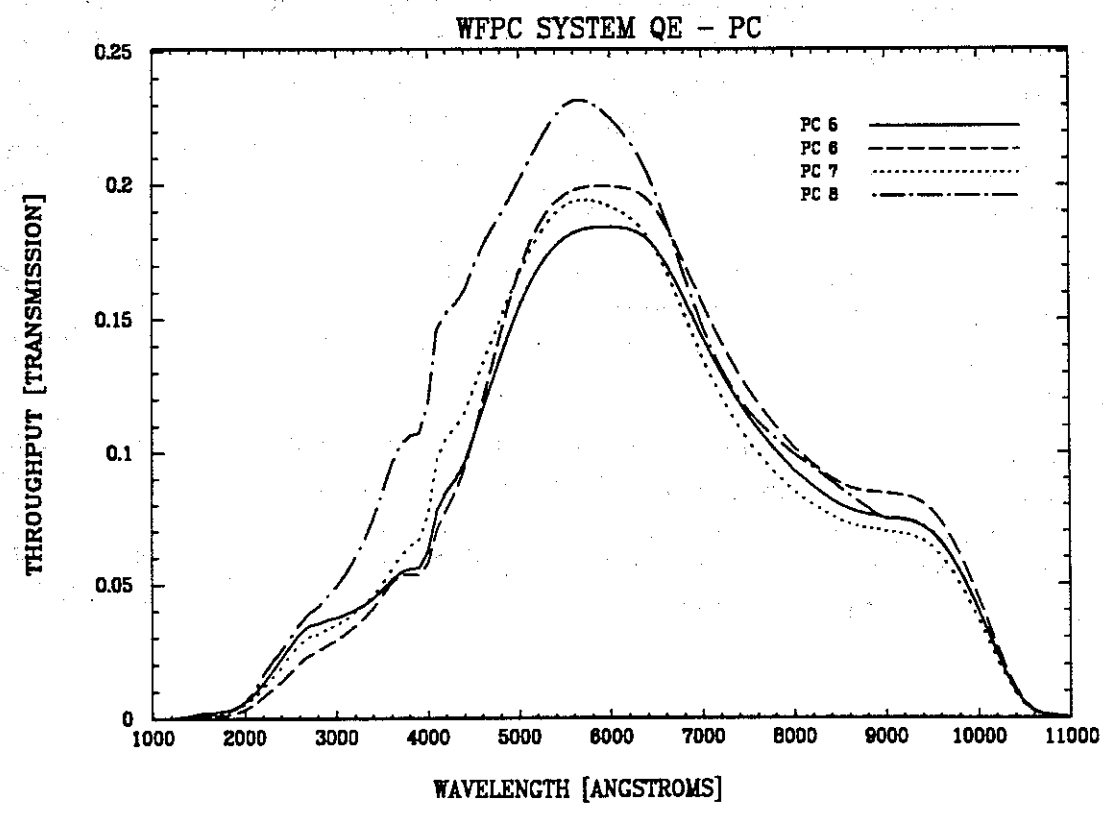

4.2 QUANTUM EFFICIENCY STABILITY

4.2.1 QEH and UV flood

The WF/PC CCDs have a "depletion layer" at their back surfaces and suffer the effect of 'quantum efficiency hysteresis' if they have not been exposed to light for a long period. The depletion layer arises by virtue of 'holes' (i.e., electron vacancies), located within the native oxide on the silicon surface and, predominantly, at the interface between the oxide and the silicon. These holes cause the electron energy levels at the back of the CCD to bend downwards, i.e., a potential gradient exists which collects electrons in the interface and oxide traps. The resulting potential well extends about 0.6 μm into the CCD, and the problem is, therefore, especially severe for photons which are not converted by the coronene, i.e., photons with $\lambda \geq 3700$Å, and which have an absorption length in silicon of less than 0.6 μm, i.e., photons with $\lambda \leq 5000$Å. For a CCD with a depletion layer at the surface, incoming photons will produce photo-electrons which start to fill the traps. As the traps become full, further photo-electrons are collected in the buried channel at the front of the CCD, i.e., the CCD responds as it should. If the light source is now removed, the trapped electrons will be released on timescales dependent on the energy level of the trap, as well as temperature. The quantum efficiency of such a device thus varies depending on the history of previous exposure to light.

The solution to this problem for the WF/PC is to apply a "UV flood." Photons of $1800 < \lambda < 3000$Å generate photo-electrons in the silicon of sufficient energy to reach the conduction band in the oxide. At the back surface of the CCD, the electrons fill the traps and are attracted by oxygen atoms on the surface, thus charging the surface. A negative charge layer at the surface of the CCD produces an 'accumulation' layer in the silicon, i.e., a potential gradient which repels photo-electrons from the back surface so that they can be collected in the buried channel. The facility to UV flood the CCDs is provided within the WF/PC by a light channel from a mirror on the external radiator (Figure 2.1). The UV flood procedure involves bringing sunlight through the light channel by orienting HST to an anti-sun pointing and allowing UV photons to accumulate the CCD surfaces for ~1 day. The timescale for loss of the negative charge on the coronene is very long at their normal operating temperature of -87° C. The initial on-orbit UV flood of the WF/PC was applied in late December 1990 and has survived through ~10 warm-ups to ~0°C.

The UV flood procedure has the side effect of increasing the Quantum Efficiency of the CCDs slightly (~10%) in the 3000Å to 5000Å region. Any improvement in sensitivity is more than offset by the fact that this QE increase is highly position dependent across the individual CCD detectors. Hence, a partial loss of the charge from the UV flood results in a change in the structure of the flat field (especially in this spectral region).

4.2.2 Internal Contamination

During testing of the WF/PC prior to launch of the HST, the absolute QE of the camera at 1500Å was observed to decline from 3% to 1% on the time scale of 2 to 3 days with the CCDs cooled to normal operating temperature. During the same interval, the QE at 2400Å declined from 6.4% to about 6.1%, while there was no significant change in the QE at 4100Å or longer wavelengths. The cause of the QE decline shortward of 2000Å is believed to have been contamination by at least two undetermined molecules, but not H_2O, as determined using measurements made with a thermal quartz-crystal microbalance placed inside the camera housing. One contaminant had an accumulation temperature of 8 to 10°C (i.e. the contaminant can be boiled off at temperatures above this), and the second contaminant had an accumulation temperature of -40 to -50°C. On-orbit performance has not been fully consistent with the results of the ground based testing.

On-orbit operation of the WF/PC revealed that the contaminants cause attenuation at wavelengths at least as long at 5000Å. Figure 4.2 shows the decline in throughput at a variety of wavelengths over many months. The flux ratios are based on observations of BD+75D325 (a blue spectrophotometric standard star) compared to a set of observations made in early February 1992 immediately following a decontamination (except for F230W in the WFC which is ratioed to July 1991 --about 10 days after a decontamination). Figure 4.2 covers the period during which routine photometric monitoring has been conducted. The individual decontaminations are indicated with vertical dashed lines.

The loss of throughput over time is accompanied by an increase in scattered light as shown in Figure 4.3. This Figure shows the ratio of the intensity along a region beyond the pyramid vertex to the center of the CCD in a series of internal flat field ("cal lamp") exposures. The decontaminations during the period plotted are indicated as in Figure 4.2.

Both the loss of throughput and the increase in scattered light are believed to result from the growth of a low temperature contaminant on the field flattening windows directly in front of the CCDs.

Figure 4.2 Quantum Efficiency versus Time

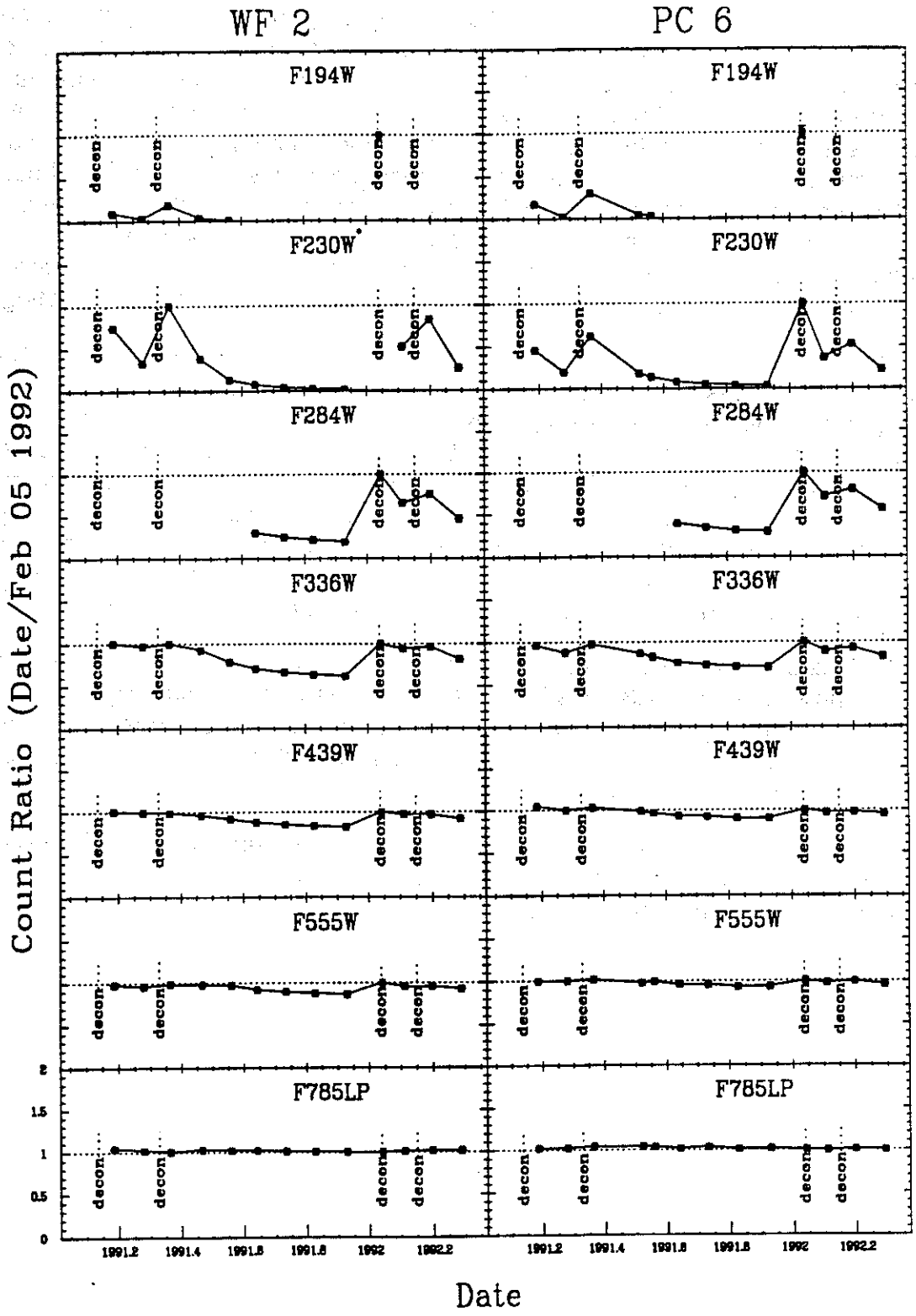

Figure 4.3 Scattered Light versus Time

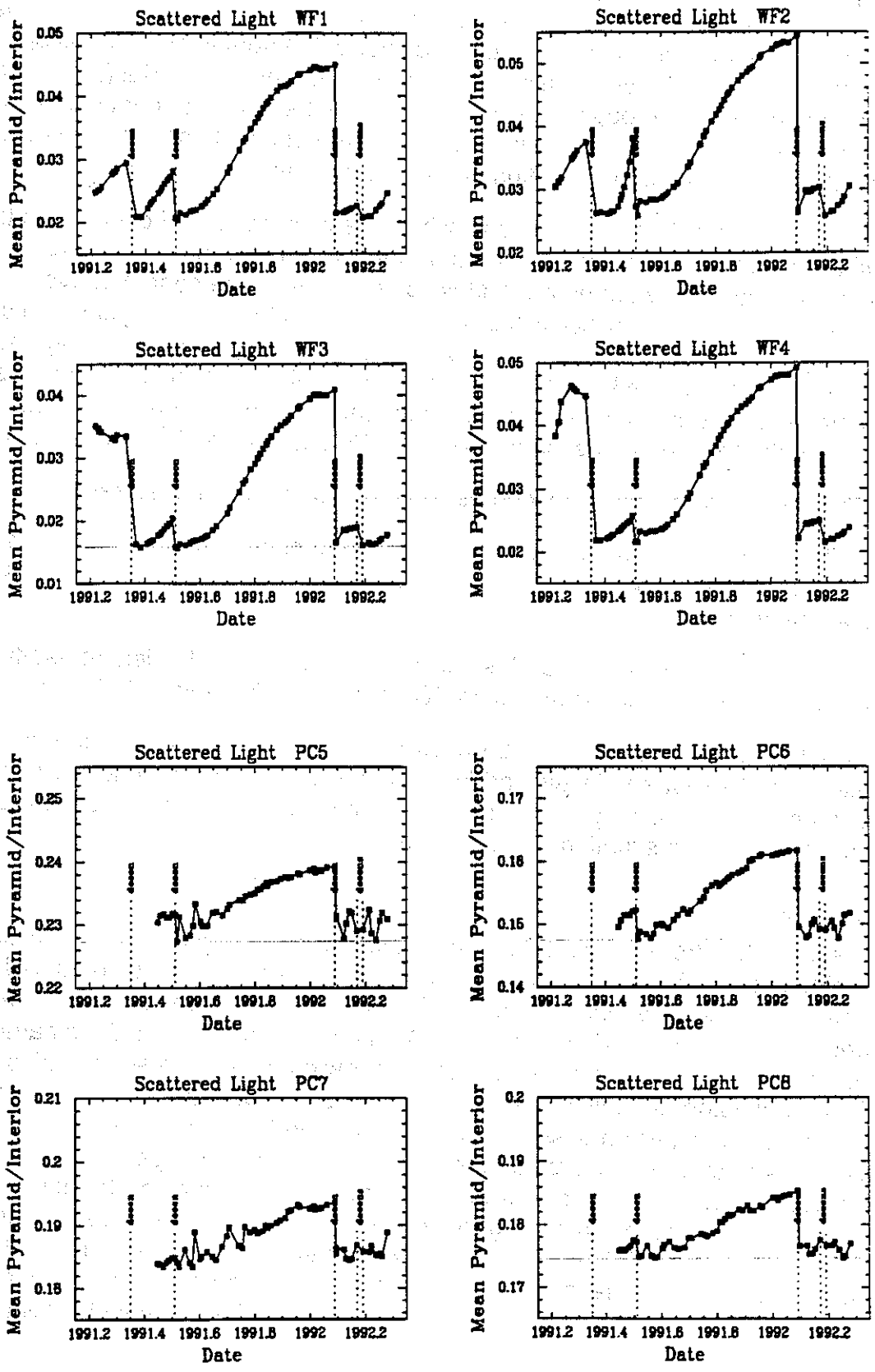

4.2.3 Decontamination Procedures

Procedures have been developed and used on orbit to decontaminate the WF/PC. These procedures are based on warming the camera heads (CCDs, Field Flattening Windows, the Thermal-Electric cooler units) above their normal operating temperatures. This results in a boil off of the contaminants and a (temporary) restoration of the UV throughput. It is believed that the boiled off contaminants mostly remain in the instrument and that the instrument contains various sources to the degree that the contamination problem is permanent.

Spacecraft or WF/PC safing events which result in the turnoff of power to the WF/PC's Thermal-Electric coolers for more than 1 - 2 hours result in the camera heads warming up to a temperature at which the state of the contaminants changes. In place of the optically featureless UV absorbing and polychromatic scattering layer (see Section 4.2.2), images thereafter display a mottled appearance which has become known as the "measles". This situation has required a decontamination procedure to remove these features. The temperature required to remove the "measles" has increased from -20°C to above +5°C since launch.

These decontamination procedures have several negative features:

A. They erode the charging applied by the UV flood and therefore advance the date at which a new UV flood will be required. A UV flood costs nearly 2 days of spacecraft time.

B. The erosion of the UV flood results in a change in the flat field at nearly all wavelengths. This change is largest in PC8 and from 3000Å to 6000Å.

C. After 1.5 years of cold operation, decontaminations which elevated the temperatures of the CCDs to levels and for periods thought consistent with preservation of the UV flood no longer were able to entirely remove the "measles" features. As of April 1992 this situation is being assessed.

4.2.4 UV Observations

As is evident from Figure 4.2 and from the known red leaks in the UV filters (see Section 4.7.3), nearly all UV science observations can only be obtained shortly after a decontamination. However, since frequent decontaminations are undesirable (as explained in Section 4.2.3) and most decontaminations have been executed with real-time commanding following unplanned spacecraft or WF/PC safings,opportunities to schedule UV observations are very infrequent. Such observations, when possible, will have only moderate quality flat fields since the earth is a rather red source and the internal calibration lamps have no useful UV output. Also, UV observations will have limited photometric calibration because of the rapid loss of throughput (especially at the shortest wavelengths). In light of this, the STScI does not believe observations at F122M or F157W are practical and cautions that other UV observations are inherently risky, may be extremely difficult to schedule, and should be discussed with the Instrument Scientists.

4.3 LINEARITY

The linearity (Υ)of the WF/PC response is dependent on both the absence of QE hysteresis and deferred charge (see Sections 4.2 and 4.7.1). The camera system follows the transfer function given below over the range from full scale of the analog to digital converter (ADC) down to a S/N = 3.

$$\log (DN_{out}) = A\Upsilon \log (P_{in})$$

Where DN_{out} is the output signal in ADC counts, A is a constant incorporating both the QE of the instrument and the electrons to DN conversion ratio, and P_{in} is the number of input photons. Both ground-based calibration and on-orbit observations using the Orion Nebula as a target give consistent results and indicate good performance. These results are tabulated in Table 4.1 (see Section 4.4).

4.4 CCD READOUT NOISE, FULL WELL AND "GAIN"

The CCDs and their associated signal chains have readout noise levels (in the absence of signal shot noise or interference) as tabulated in Table 4.1. The conversion factors from detected electrons (QE x number of incident photons) to data numbers (DN) are also listed. As is the case for the linearity determination (see Section 4.3), the on-orbit values are consistent with the pre-launch calibration. Table 4.1 represents the somewhat more accurate ground based calibration and is taken from the IDT OV/SV Report. The on-orbit WFC results are also included. But see also Section 4.7.5.

Table 4.1 Noise, Gain, and Linearity

Camera	$N_{ro}(e^-)$	Gain (e^-/DN)	Υ
W1	13.09	7.21	1.002
W2	13.72	8.22	1.003
W3	13.25	8.57	1.003
W4	13.56	8.07	1.003
P5	12.74	8.17	1.005
P6	14.45	8.18	0.999
P7	15.56	7.93	1.004
P8	13.65	8.38	1.003
W1 orbit	13.1±2.5	7.1±1.2	0.998±.002
W2 orbit	11.7±3.4	7.2±1.4	1.001±.002
W3 orbit	12.9±2.3	7.8±1.2	1.002±.002
W4 orbit	11.4±2.8	6.8±1.3	1.004±.003

4.5 POINT-SPREAD FUNCTION

4.5.1 Effects of OTA Spherical Aberration

The OTA Spherical Aberration problem greatly changed the expected Point Spread Function (PSF) observed by the WF/PC. The fraction of the light within the central 0.1 arc second is reduced by a factor of ~5. The resulting PSF has "wings" which extend to large radii (several arc seconds) and greatly reduce the contrast of the images and degrade the measurements of sources near bright objects or in crowded fields. Burrows et al. (1991, *Ap.J. Lett.* **369**, L21) provide a more complete description of the HST PSF. Their "Case 3", an observation of the star HD124063 on PC6 in F487N is reproduced as Figures 4.4 and 4.5. These Figures show the radial surface brightness profile and the encircled energy, respectively.

Figure 4.4 PSF Surface Brightness

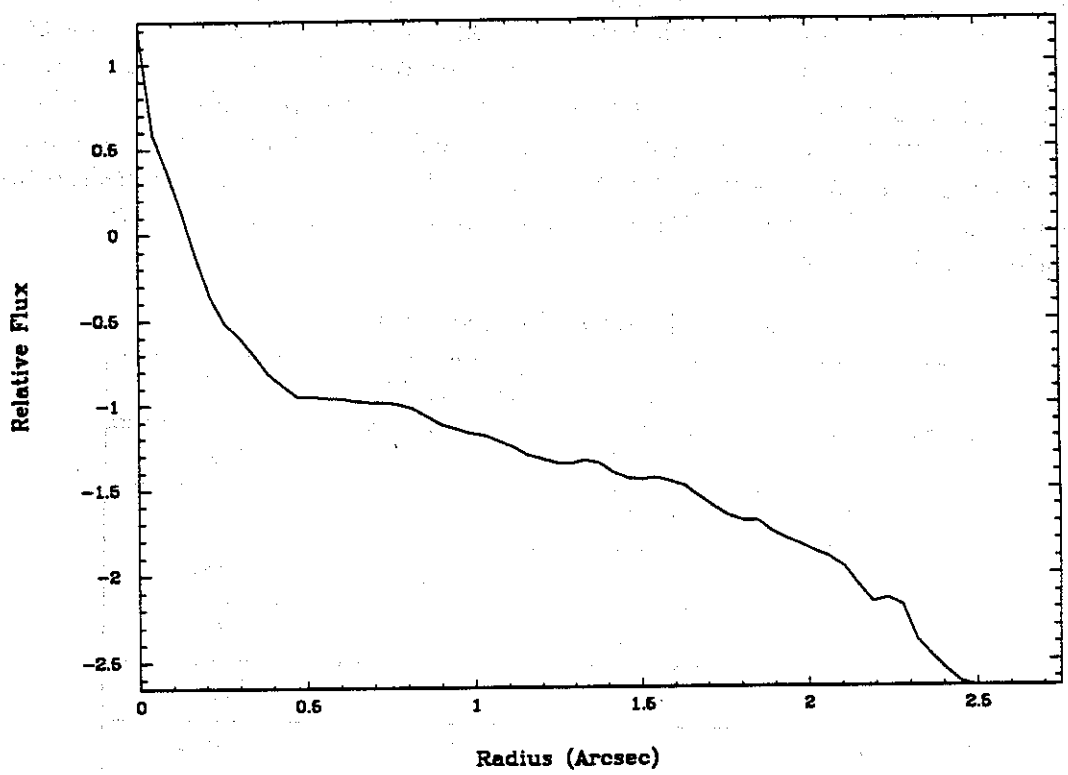

The PSF as observed with the WF/PC has an additional level of complication because the WF/PC reimages the OTA focal plane (which is approximately coincident with surfaces of the WF/PC pyramid). The reimaging is accomplished with Cassegrain repeater optics which have their own central obscurations. Since these are co-aligned with the central obscuration of the OTA only at the field centers, the core of the PSF changes with location within the field of view of each WF/PC CCD. The field centers for each CCD as reported in the IDT OV/SV Report are listed in Table 4.2 in pixel coordinates.

Figure 4.5 PSF Encircled Energy

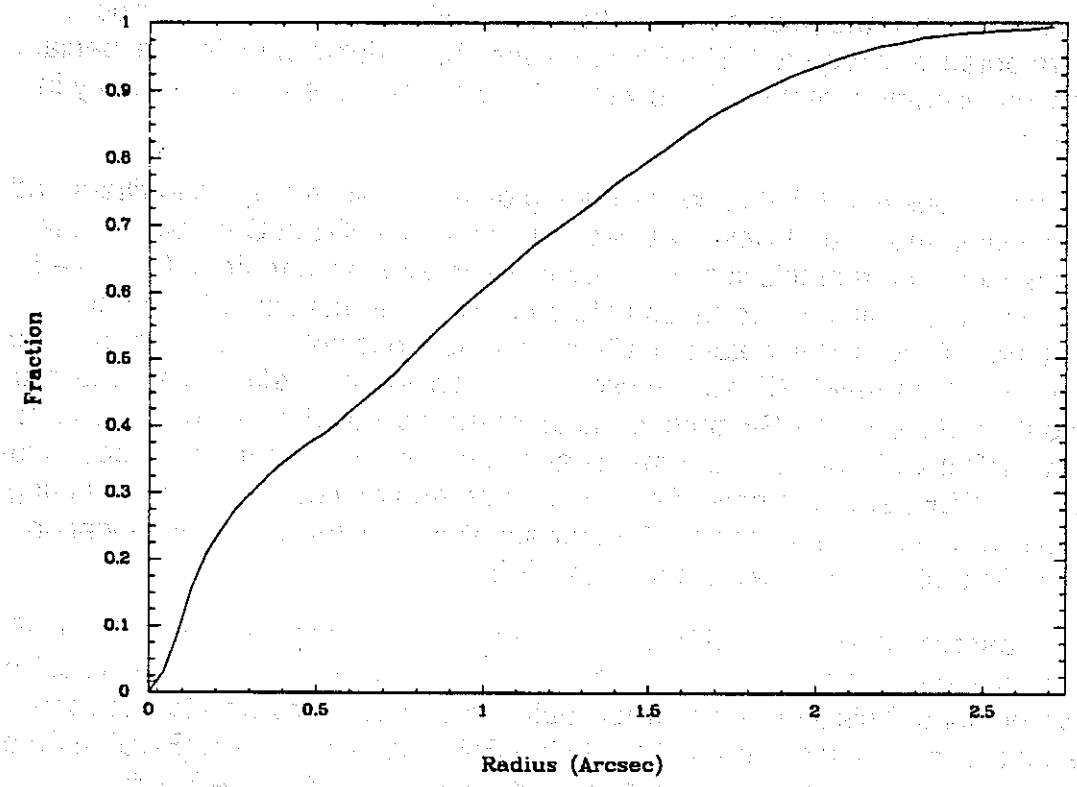

Table 4.2 Field Centers

Camera	Row	Column
W1	300	575
W2	260	425
W3	380	400
W4	500	500
P5	200	500
P6	310	245
P7	680	370
P8	520	520

4.5.2 Observed and Modeled PSFs

Some WF/PC observations can be significantly improved by the application of image deconvolution techniques. These techniques require knowledge of the PSF of the scene to be restored. Since the PSF depends upon both the wavelength of the observation and the position within the field of view, a very large number of PSFs are potentially required. The PSF may also be variable with time, especially if the optical alignment of the HST is varied (as was the case frequently early in the mission).

A library of observed PSFs, concentrating on the most heavily used filters and locations within the field of view, has been placed in the STScI Calibration Data Base. It is expected that this library will continue to expand with time. Observed PSFs have low signal to noise ratios at large radii due to the limited dynamic range of the WF/PC. PSFs obtained with the shortest possible exposures may not properly reflect the true PSF (see Section 3.4). Considerable effort has gone into the modeling of the HST PSF, both to measure the optical aberrations in support of the WF/PC II and Co-Star Instruments and to provide PSFs for image deconvolution. Such PSFs are both noise free and do not require valuable HST observing time. Software to generate model PSFs for any WF/PC filter and at any location within the field of view is available from the STScI.

Both observed and modeled PSFs will not provide a perfect match to the PSF in actual science observations except for very short exposures due to the "jitter" in the HST pointing. This jitter is not predictable but can be recovered to a reasonable extent for observations obtained with the Point Control System (PCS) in Fine Lock. It can only be estimated for observations obtained in Coarse Track.

4.6 COSMIC-RAY BACKGROUND

For a faint-object observation, special efforts may have to be made to remove the time-integrated effects of charged particles. Long observations are particularly impacted by cosmic ray events and dividing the exposure into two or more integrations is recommended in many cases. Since the WF/PC CCDs must be readout upon entry into earth occultation, exposures which span more than one target visibility period must always be split into multiple integrations. Currently, by defaults, any exposure longer than 10 minutes will be "CR-SPLIT" unless specified otherwise by the observer.

Due to the finite thickness of the CCD detectors, cosmic ray events often deposit significant quantities of charge in more than one pixel. At low count levels the cosmic ray events become undetectable in the readnoise. To provide a count of rate of cosmic ray events requires that a pixel or an event threshold be specified. Several cases are analyzed in the IDT OV/SV Report. A rate of 4.7 pixels second^{-1} CCD^{-1} above a threshold of 9 DN and 3.2 pixels second^{-1} CCD^{-1} above 20 DN was observed. At these levels an average of 2.7 and 1.88 pixels, respectively, were involved in each event. This yields an event rate of 1.7 events second^{-1}CCD^{-1}.

4.7 INSTRUMENT ANOMALIES

4.7.1 Deferred Charge

The TI CCDs in the WF/PC suffer from a low level non-linearity called "deferred charge," which results from a spurious potential pocket between the transfer gate and serial register. The effects are complex but basically very low level charge (≤ 250 e^- $pixel^{-1}$) is transferred poorly and tends to cause tails behind faint images. Some charge (~50e^-) is lost entirely so that it is not feasible to recover the photometry accurately even in uncrowded fields.

The solution is to "preflash" the CCDs with the internal calibration lamps located behind the shutter. A signal level of ~30 to 40 e^- $pixel^{-1}$ is sufficient to suppress the deferred charge effect. The cost of the photon noise in the preflash is that the effective readout noise increases from ~13 e^- rms without the preflash to ~15 e^- rms. A preflash also imposes a cost by increasing the overhead time. When several exposures are required in rapid succession, a trade-off between charge transfer efficiency and time resolution may be necessary.

The structure of the preflash "image" is dependent upon which shutter blade is in the beam prior to the exposure. Blade "B" has several reflective spots which result in a ~25% higher preflash level and some additional structure in the illumination pattern. Due to limitations in the flight software it is not possible in all cases to be certain which blade was in the beam at the time of the preflash. Subject to this limitation, the calibrated "preflash" image will be removed, as part of the routine data reduction (see section 6.2).

Observers are advised to preflash all WF/PC images which are not predicted to have at least 4 DN in every pixel on the CCD(s) containing targets of interest. The small projected pixel size, low background levels, and relatively short exposure times typical of WF/PC observations rarely provide sufficient signal per pixel to suppress the deferred charge effect. Exceptions may include very long exposures with the WFC in broad band red filters and observations of extended sources such as Orion. Note that extended sources such as planets generally do not qualify since the image of the planet must be transferred across regions of the CCD which will not have a sufficient signal level.

4.7.2 Overexposure: Blooming and Residual Image

The usable signal level in the WF/PC CCDs is limited to approximately 30,000 e^- due to the combination of the 12 bit analog to digital converter (max value 4095) and the ~8 e^-/DN quantization of the signal.

Blooming up and down a CCD column occurs when more than about ~80,000 e^- (the "full well" capacity) are collected in any pixel. When the adjacent pixels up and down the column are full, the charge will flow into the next pixels along the column, and so on. The orientation of the bloomed column(s) on the sky depends on the readout direction of the particular CCD (see Figure 3.5) and the

roll angle of the spacecraft.

Residual images occur for pixels which collect more than about 200,000 e^- (this threshold varies by about a factor of 2 depending on location and CCD). Electrons are trapped at the interface between the buried channel and the insulating oxide beneath the electrodes, and are released later. The time constants for electron release are on the order of minutes to hours. The intensity of the residual image depends on the integration ("exposure") time and the length of time since the overexposure. Most of the CCDs have residuals which decay after about an hour. There is some non-uniformity along the column in the level of residual image from bloomed images on some of the CCDs. On long (~half-orbit) exposures through the wide V or wide I filters, stellar objects brighter than V ~19 (with spherical aberration) can leave residual images in the WFC.

In ground-based thermal-vacuum tests, the CCDs were overexposed to a maximum of several thousand times the nominal pixel well capacity, and the decay of the resulting residual images was monitored, typically for several hours. In particular, it was found that, following an over-exposed image of point sources, a uniform residual level could be introduced by over-exposure to the internal flat-field lamps. The decay of this uniform residual level is such that, after such a "purging" and a wait of 20 to 60 minutes, the remaining residual is very uniform at the 1 to 2 DN level. It was therefore planned to carry out such a residual image purge following those observations expected to leave residual images which would compromise the subsequent images. The residual image from the purge can be subtracted from subsequent images, as necessary, during the routine data reduction. The presence of spherical aberration in the OTA greatly decreases the frequency of extreme overexposure of the WF/PC CCDs in addition to reducing the importance of faint residual images. Therefore this capability has been infrequently used and observers concerned about extreme overexposures are advised to consult the Instrument Scientists.

Extreme overexposure of the CCDs is not believed to cause any permanent effects in the WF/PC CCD and therefore the WF/PC does not have any bright object limits other than those imposed by the HST as a whole.

The WF/PC CCDs can be operated in a non-standard mode during the integration phase of an exposure in order to limit the blooming to only those columns containing the bright sources. This is accomplished by operating the serial transfer register clocks during the integration. This will result in an enhanced dark current rate over much of the CCDs and is only necessary for overexposures expected to have signal levels of ~few x 10^7 e^- within a single column. This mode is only possible for exposure times $\geq$ 1 second.

4.7.3 Red Leaks in UV Filters

The "red leaks" in the UV filters are shown in Figure 4.6 for F122M, F157W, F194W, F230W and F284W. The presence of significant red leaks in the UV filters, together with the much greater sensitivity and wavelength coverage in the red part of the spectrum, makes calibration of UV observations difficult. Furthermore, the internal contamination (see Section 4.2.2) adds a time variable factor.

Figure 4.6 UV Filter Red Leaks

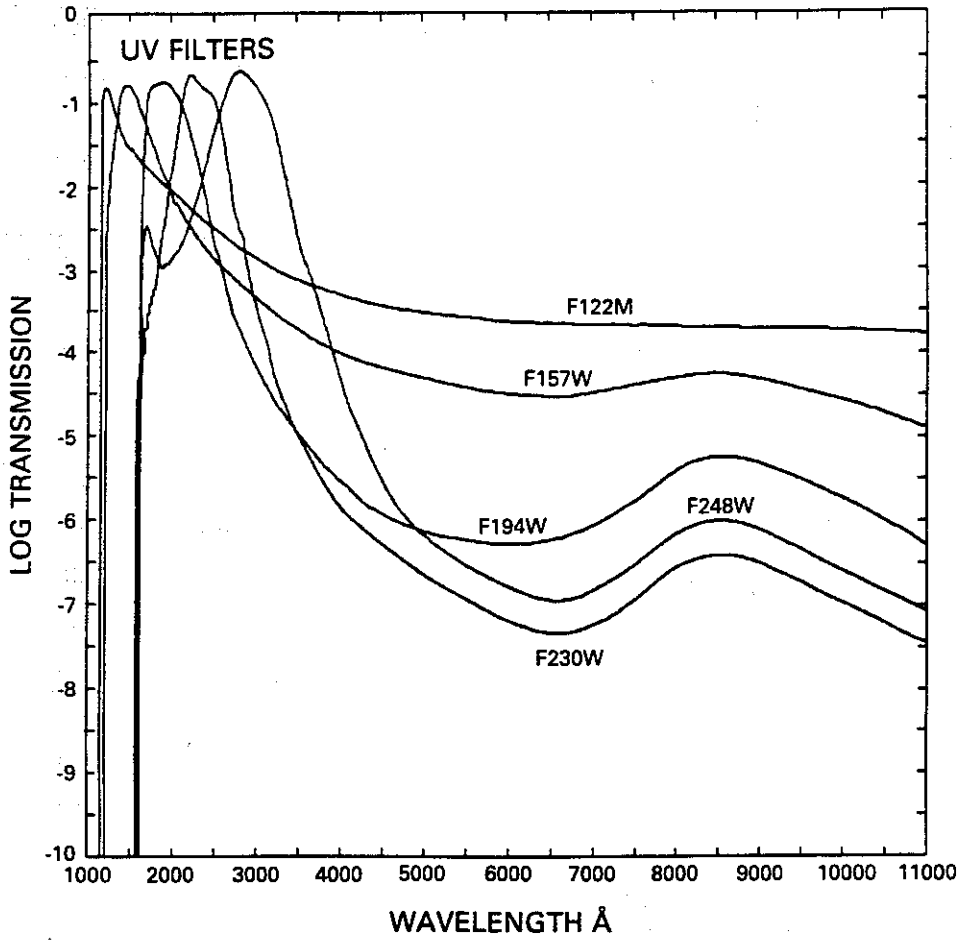

Table 4.3 shows the red leak as a percentage of the total detected flux from the source. In the middle column, the red leak is defined as the percentage of the detected flux longward of 3800Å; in the forth column, the red leak is defined as the percentage of the detected flux longward of the wavelengths shown in the rightmost column. These values do not reflect the impact of the internal contaminants.

Table 4.3 Red Leak in UV Filters

Object	Filter	Red Leak (%) ($\lambda > 3800$Å)	Red Leak (%) $\lambda > \lambda_c$	λ_c (Å)
BOV	F122M	5.3	76.2	1400
	F157W	0.4	6.1	2000
	F194W	0.0	0.2	2600
	F230W	0.0	0.0	2900
	F284W	0.0	0.0	3600
AOV	F122M	56.0	97.6	1400
	F157W	10.5	21.6	2000
	F194W	0.1	0.4	2600
	F230W	0.0	0.2	2900
	F284W	0.1	0.3	3600
GOV	F122M	94.5	100.0	1400
	F157W	90.3	99.8	2000
	F194W	18.2	23.2	2600
	F230W	0.4	1.9	2900
	F284W	0.3	0.8	3600
KOIII	F122M	98.6	100.0	1400
	F157W	96.3	98.6	2000
	F194W	34.0	35.5	2600
	F230W	1.2	2.0	2900
	F284W	1.0	2.0	3600
E gal. (z=1)	F122M	98	100	1400
	F157W	95	98	2000
	F194W	55	58	2600
	F230W	3	2	2900
	F284W	0	1	3600
Sbc gal (z=1)	F122M	89	99	1400
	F157W	77	92	2000
	F194W	19	28	2600
	F230W	0	3	2900
	F284W	0	0	3600
Scd gal (z=1)	F122M	51	83	1400
	F157W	14	24	2000
	F194W	1	1	2600
	F230W	1	1	2900
	F284W	0	0	3600

Table 4.3 Red Leak in UV Filters

Object	Filter	Red Leak (%) ($\lambda > 3800$Å)	Red Leak (%) $\lambda > \lambda_c$	λ_c (Å)
QSO (z=2)	F122M	60	98	1400
	F157W	29	63	2000
	F194W	1	2	2600
	F230W	0	1	2900
	F284W	0	1	3600

4.7.4 Overhead Time

Commands to the WF/PC are processed at spacecraft "major frame" intervals of one minute. A filter wheel may be returned to its "clear" position and another filter selected in one minute. An exposure takes a minimum of one minute, and a readout of the CCDs takes one minute. There is no overhead time advantage in reading out a subset of the CCD except when the WF/PC readout occurs in parallel with the operation of a second instrument (where 2 minutes may be required to readout all 4 CCDs).

If a preflash is necessary to give enough signal to avoid deferred charge, then 2 minutes need to be allowed for filter change, a minute for the exposure with the internal lamps, and a minute to return to the filter to be used for observation. note that the RPSS Resource Estimator should be used in developing Phase 2 proposals.

4.7.5 Missing Codes in the A/D Converter

The analog to digital (A/D) converters for both the WFC and PC produce 12-bit words. A problem in the A/D converters results in small errors in the bit codes which cause the least significant bit to be lost entirely and certain values to be more likely to occur than neighboring values.

This problem is addressed in the data reduction process. It is important to note, however, that no attempt is made to "correct" the digitization process. Rather a statistical correction is applied to remove the biases introduced by this problem. The primary impact on observations is an increase in the effective readout noise to ~15 to 20 e^- (i.e. slightly more than 2 DN).

4.7.6 Filter Anomalies

A number anomalies of have been observed in the filter set including:

A: F122M has a significant number of pinholes.

B: F656N exhibits a fringe or ring-like pattern but still appears to be perform-

ing satisfactorily as an interference filter (this may be a substrate problem).

C: F1042M has a degraded point spread function. This is probably the result of transmission of light through the CCD silicon, reflection by the electrodes, and subsequent detection in the silicon. F1083N may be presumed to share this effect.

D: Some filters have significant tilts which displace images by a few pixels. Observations with the F785LP filter are offset by ~0.3 arc seconds from the F555W filter. Most filters have tilts significantly less than this case.

Observers are also cautioned that the ground based calibration of the filter passband wavelengths was only accurate to ~3Å and was carried out in the early 1980s. It is not advisable to place narrow emission lines at the half power points of the narrow band filters and expect to know the throughput to within a factor of 2.

4.7.7 Internal Scattered Light due to Contaminants

In Section 4.2.2, the growth in scattered light resulting from the internal contaminants is discussed. The time variability of the scattered light causes changes in the level of flat field exposures near the corners and edges of the CCDs. This decreases the accuracy of the flat fields (see Chapter 6 of the IDT OV/SV Report).

Also, there are features in the images arising from dust particles which change in appearance with changes in the amount of scattered light. Observers are strongly cautioned to examine the flat field calibration files appropriate to their observations. Strong flat field features coincident with targets of interest may present problems in flat field calibration due to the time variable nature of the scatter light. Internal flat field calibrations are being obtained frequently and may be used to make a differential correction to some extent.

4.7.8 Image Structure due to Residual Contaminants (Measles)

The internal contaminants (see Sections 4.2.2 and 4.2.3) can leave residual structures on the optical surfaces above the CCD detectors. These features are typically at the 1% level with somewhat brighter or darker cores.

Although during the first year of on-orbit operation of the WF/PC, it was possible to remove the measles with decontamination procedures (see Section 4.2.3), starting in February 1992 the same procedures were unsuccessful in removing all of the measles. The status of the WF/PC with regard to these features is presently uncertain and announcements will be made in the STScI Newsletter and on the Space Telescope Electronic Information System (STEIS). Figure 4.7 shows at high contrast an example of one of the worst regions on PC8. This figure is the average of 10 F517N observations of the sunlit earth obtain during March and April 1992.

Figure 4.7 Measles Example: PC8 Earth-Flat in F517N

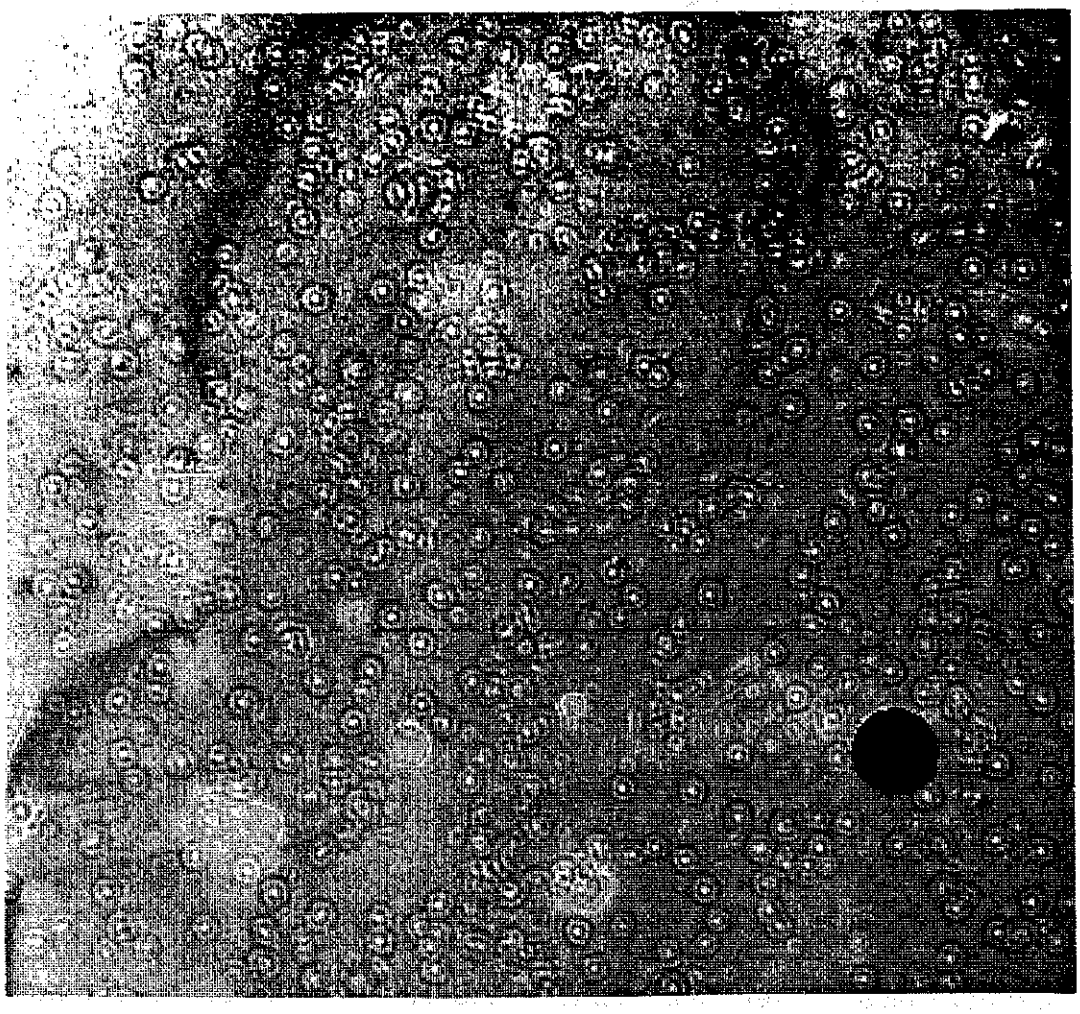

5.0 ESTIMATION OF EXPOSURE TIME

5.1 POINT SOURCES

Accurate predictions of exposure time will require knowledge of:

a. Overall spectral response of the system (Section 4.1).

b. Spectral transmission of 48 filters and grisms (Section 3.2).

c. Spectral energy distribution and spatial profile of the target.

d. Criteria for specifying desirable charge levels.

When the transmissions of filters are combined with the overall system response of Figure 4.1, we obtain detective-quantum-efficiency plots (electrons-per-photon, Q_λ, as a function of λ) for each filter as shown in Figure A.3. These DQE plots link the output of the CCD to the photon flux at the input to the telescope.

These calibrations exist in the STScI Calibration Data Base and are accessible with the STSDAS Synphot package. The Synphot Users Guide should be consulted for further details. Included in the WF/PC Instrument Handbook is a sufficient calibration for exposure planning. Since the analysis of existing data often will require a more precise calibration and since such analysis must account for the normalization of the flat field calibrations, this Handbook is not intended to be used for such analysis.

In Table 5.1 the dimensionless efficiency and the mean wavelength for each filter and CCD is tabulated. In Appendix A.1 the dimensionless efficiency, mean wavelength, width of the bandpass, equivalent Gaussian, the maximum value of QE transmission over the bandpass of the filter, the derivative of the mean wavelength with the spectral index, the pivot wavelength, average wavelength, and wavelength of maximum transmission are Tabulated. The last three parameters are specific to Synphot and will not be considered further here.

The remaining parameters are defined as follows:

The dimensionless efficiency is

$$\int Q(\lambda)\, T(\lambda)\, d\lambda/\lambda$$

where $Q(\lambda)$ is the QE of the camera + OTA and $T(\lambda)$ is the filter transmission, both as functions of the wavelength λ.

The mean wavelength is similar to that defined in Schneider, Gunn, and Hoessel (1983, *Ap. J.*, **264**, 337):

$$\bar{\lambda} = exp\left[\frac{\int Q(\lambda)\,T(\lambda)\,ln(\lambda)\,d\lambda/\lambda}{\int Q(\lambda)\,T(\lambda)\,d\lambda/\lambda}\right]$$

This rather unconventional definition has the property that the correspondingly defined mean frequency is just $c/\bar{\lambda}$; it is in some sense halfway between the conventional frequency mean and the wavelength mean.

The effective Gaussian is given by

$$\sigma^2 = \frac{\int Q(\lambda)\,T(\lambda)\left[\,ln\frac{\lambda}{\bar{\lambda}}\,\right]^2\frac{d\lambda}{\lambda}}{\int Q(\lambda)\,T(\lambda)\,\frac{d\lambda}{\lambda}}$$

The effective width of the bandpass is then

$$\delta\bar{\lambda} = 2\,[2ln(2)]^{1/2}\sigma\bar{\lambda}$$

and it can be shown that

$$\frac{d\bar{\lambda}}{d\alpha} = \bar{\lambda}\sigma^2$$

Of rather more interest is the camera-to-camera variation of the mean wavelength, due to the variations in QE. One would expect this to be most serious in the long-wavelength bands, where the fall of the CCD QE is used to define the long-wavelength cutoff; the effect is not too bad, however. In the **I** (F785LP) band in the WFC, the range is only 23Å, from 8907Å (WF4) to 8930Å (WF1). In **V** (F555W), the effect is predictably much smaller, 10Å; in the PC, however, the effect of the much higher response of PC8 in the blue takes its toll, and there is a 55Å spread. A 100Å uncertainty in the 3500Å lever arm is about a 3% color uncertainty in **V-I** (which can, of course, be calibrated).

The WF/PC **U**, **V** and **I** system is fairly close as regards effective wavelengths to the Johnson **UVI** system, but cross-calibration will be necessary to convert to Johnson magnitudes (see the IDT OV/SV Report and Harris et al. 1991, *A.J.* **101**, 677).

Note that grating exposure times are not determined by the full passband; they are determined instead by the $\Delta\lambda$ falling within a single pixel in the vicinity of the blaze wavelength. Gratings can therefore be treated as narrowband filters with FWHM equal to the number of Å pixel^{-1} (Table 3.2). Grating images can then be treated as stellar images (except for a spread-function adjustment) when comput-

ing signal levels. Altogether, the three WF/PC gratings give rise to eight possible passband widths and therefore simulate eight different "filters" for which exposure times are to be calculated. Specifically, the $\Delta\lambda$ of each grating is different for f/12.9 than for f/30. Additionally, the ultraviolet grating has different $\Delta\lambda$'s when used in the second-order spectrum than when used in the first order (see Section 3.2).

To estimate the number of electrons collected from a point source of apparent visual magnitude (V), one can use the equation:

$$N_{el} = Ct\left[\int QT d\lambda/\lambda\right] \times 10^{-0.4\,(V + AB_{\nu})}$$

where, $C = 2.5 \times 10^{11}$, t is the exposure time in seconds, the QT integral is given in Tables 5.1 and A.1, and AB_{ν} is given in Table 5.2 as a function of spectral type and wavelength.

$V + AB_{\nu}$ is the monochromatic magnitude on the Oke system at the mean wavelength of the filter, *viz.*,

$$(V + AB_{\nu}) = -2.5 \log F_{\nu} - 48.6$$

where F_{ν} is the flux in ergs cm^{-2} s^{-1} Hz^{-1} (Oke and Gunn, 1983, *Ap. J.*, **266**, 713).

In terms of F_{ν},

$$N_{el} = Ct\left[\int QT d\lambda/\lambda\right] F_{\nu}$$

where $C = 6.9 \times 10^{30}$.

The last equation assumes a flat continuum. For a source of spectral index α, the shift in mean wavelength for each filter may be calculated from the tabulated $d\bar{\lambda}/d\alpha$. The value of F_{ν} should then be calculated at the appropriate wavelength for insertion into the above equation.

Table 5.1 Summary of System Throughputs $\int QT d\lambda/\lambda$

	W1	W2	W3	W4	P5	P6	P7	P8
F122M	0.000123	0.000123	0.000118	0.000111	0.000099	0.000075	0.000095	0.000113
$\bar{\lambda}$	3023.27	2909.33	2978.55	2946.95	3046.88	3669.81	3133.16	3349.59
F128LP	0.156659	0.141458	0.142671	0.134928	0.137361	0.141405	0.140181	0.173929
$\bar{\lambda}$	5346.23	5181.04	5215.70	5259.76	5474.49	5680.78	5426.38	5267.19
F157W	0.000090	0.000094	0.000086	0.000086	0.000085	0.000042	0.000078	0.000068
$\bar{\lambda}$	1974.85	1943.41	1979.01	1934.95	1885.19	2195.08	1902.45	2136.73
F194W	0.000269	0.000284	0.000263	0.000251	0.000231	0.000125	0.000203	0.000236
$\bar{\lambda}$	2069.10	2067.94	2071.40	2064.76	2006.52	2030.14	2004.70	2035.34
F230W	0.001162	0.001223	0.001154	0.001058	0.000660	0.000412	0.000575	0.000772
$\bar{\lambda}$	2348.24	2347.86	2349.48	2346.24	2344.65	2350.28	2345.36	2341.66
F284W	0.002333	0.002439	0.002374	0.002060	0.001570	0.001144	0.001424	0.001952
$\bar{\lambda}$	2821.84	2821.39	2823.96	2820.32	2841.08	2859.07	2848.21	2859.85
F336W	0.004206	0.004357	0.004364	0.003674	0.003470	0.003134	0.003523	0.005683
$\bar{\lambda}$	3353.53	3352.45	3353.83	3353.73	3361.98	3372.60	3369.38	3378.02
F368M	0.001922	0.001959	0.001991	0.001698	0.001696	0.001649	0.001884	0.003176
$\bar{\lambda}$	3687.64	3687.06	3687.33	3688.46	3687.96	3687.20	3691.09	3689.08
F375N	0.000675	0.000685	0.000698	0.000600	0.000598	0.000581	0.000680	0.001135
$\bar{\lambda}$	3755.34	3755.26	3755.31	3755.45	3755.41	3755.25	3755.86	3755.50
F413M	0.003913	0.003858	0.003972	0.003545	0.003603	0.003333	0.004449	0.006606
$\bar{\lambda}$	4124.70	4123.40	4123.47	4125.05	4125.42	4125.69	4125.59	4122.27
F437N	0.000255	0.000243	0.000250	0.000232	0.000236	0.000229	0.000284	0.000400
$\bar{\lambda}$	4365.78	4365.76	4365.76	4365.78	4365.78	4365.80	4365.76	4365.74
F439W	0.010020	0.009569	0.009836	0.009112	0.009257	0.008974	0.011089	0.015633
$\bar{\lambda}$	4353.17	4347.63	4347.26	4353.68	4353.20	4361.85	4347.14	4338.06
F469N	0.000478	0.000436	0.000447	0.000436	0.000439	0.000458	0.000495	0.000641
$\bar{\lambda}$	4687.16	4687.15	4687.14	4687.16	4687.15	4687.18	4687.13	4687.09
F487N	0.000628	0.000563	0.000575	0.000570	0.000571	0.000613	0.000626	0.000773
$\bar{\lambda}$	4868.56	4868.55	4868.54	4868.56	4868.55	4868.57	4868.53	4868.49
F492M	0.010044	0.008995	0.009173	0.009094	0.009125	0.009797	0.009998	0.012351
$\bar{\lambda}$	4908.78	4907.05	4906.62	4908.01	4907.96	4910.26	4905.36	4900.92

Table 5.1 Summary of System Throughputs $\int QT d\lambda/\lambda$

	W1	W2	W3	W4	P5	P6	P7	P8
F502N	0.000651	0.000578	0.000588	0.000588	0.000589	0.000640	0.000636	0.000767
$\bar{\lambda}$	5018.53	5018.52	5018.52	5018.52	5018.53	5018.53	5018.52	5018.50
F517N	0.002609	0.002301	0.002336	0.002339	0.002355	0.002572	0.002526	0.003011
$\bar{\lambda}$	5170.14	5170.09	5170.07	5170.08	5170.13	5170.15	5170.08	5170.04
F547M	0.014827	0.012993	0.013154	0.013149	0.013382	0.014578	0.014268	0.017015
$\bar{\lambda}$	5455.85	5455.18	5454.91	5454.62	5455.87	5455.37	5455.10	5455.11
F555W	0.051936	0.045801	0.046426	0.046144	0.047083	0.050904	0.050251	0.060354
$\bar{\lambda}$	5426.27	5419.56	5416.77	5417.74	5426.20	5429.61	5411.15	5394.80
F569W	0.038977	0.034144	0.034536	0.034431	0.035264	0.038327	0.037255	0.044115
$\bar{\lambda}$	5599.23	5596.89	5595.39	5593.83	5600.68	5599.77	5592.21	5585.60
F588N	0.000886	0.000771	0.000779	0.000776	0.000800	0.000866	0.000840	0.000993
$\bar{\lambda}$	5879.83	5879.83	5879.83	5879.82	5879.83	5879.83	5879.81	5879.79
F606W	0.068987	0.060471	0.061009	0.060434	0.062883	0.068153	0.065197	0.076240
$\bar{\lambda}$	5844.45	5839.19	5834.57	5830.22	5850.31	5851.48	5822.46	5797.69
F622W	0.041917	0.036557	0.036794	0.036417	0.038226	0.041421	0.039146	0.045212
$\bar{\lambda}$	6129.90	6129.26	6127.33	6124.51	6134.14	6134.40	6120.14	6107.34
F631N	0.000446	0.000388	0.000391	0.000386	0.000407	0.000440	0.000413	0.000471
$\bar{\lambda}$	6306.26	6306.26	6306.26	6306.26	6306.27	6306.27	6306.25	6306.24
F648M	0.008108	0.007070	0.007091	0.006981	0.007453	0.008072	0.007437	0.008365
$\bar{\lambda}$	6467.88	6467.99	6467.60	6466.93	6468.93	6469.08	6466.42	6464.26
F656N	0.000242	0.000211	0.000211	0.000207	0.000223	0.000241	0.000220	0.000246
$\bar{\lambda}$	6558.84	6558.84	6558.84	6558.84	6558.84	6558.84	6558.83	6558.83
F658N	0.000239	0.000209	0.000209	0.000205	0.000221	0.000239	0.000218	0.000243
$\bar{\lambda}$	6576.45	6576.45	6576.45	6576.45	6576.46	6576.46	6576.45	6576.44
F664N	0.002703	0.002359	0.002360	0.002313	0.002503	0.002713	0.002455	0.002721
$\bar{\lambda}$	6637.00	6637.01	6636.96	6636.86	6637.14	6637.16	6636.81	6636.57
F673N	0.001105	0.000965	0.000964	0.000942	0.001027	0.001114	0.000999	0.001100
$\bar{\lambda}$	6722.56	6722.56	6722.56	6722.54	6722.58	6722.59	6722.54	6722.51
F675W	0.031871	0.027767	0.027762	0.027116	0.029512	0.032011	0.028851	0.032174
$\bar{\lambda}$	6674.73	6674.40	6672.29	6667.30	6679.57	6680.43	6665.71	6658.00

Table 5.1 Summary of System Throughputs $\int QT d\lambda/\lambda$

	W1	W2	W3	W4	P5	P6	P7	P8
F702W	0.049598	0.042984	0.042981	0.041618	0.045807	0.049755	0.044336	0.049853
$\bar{\lambda}$	6867.70	6861.76	6859.79	6845.56	6870.61	6872.95	6843.74	6840.00
F718M	0.008244	0.007166	0.007119	0.006835	0.007735	0.008413	0.007248	0.007936
$\bar{\lambda}$	7154.60	7153.64	7153.04	7150.20	7155.03	7155.34	7150.60	7152.01
F725LP	0.030443	0.024684	0.025457	0.023559	0.027256	0.030108	0.025116	0.028181
$\bar{\lambda}$	8424.25	8378.15	8407.60	8395.87	8401.82	8412.20	8402.84	8395.24
F785LP	0.021863	0.017199	0.018088	0.016584	0.019176	0.021329	0.017699	0.019887
$\bar{\lambda}$	8874.66	8845.22	8864.53	8860.66	8869.83	8876.38	8870.05	8852.73
F791W	0.023267	0.019548	0.019720	0.018435	0.021209	0.023235	0.019566	0.022073
$\bar{\lambda}$	7880.78	7860.49	7872.84	7863.73	7862.70	7867.12	7862.43	7870.66
F814W	0.031137	0.025738	0.026255	0.024471	0.028074	0.030888	0.025939	0.029089
$\bar{\lambda}$	8086.40	8049.53	8072.87	8060.33	8058.69	8067.49	8058.26	8059.06
F850LP	0.013966	0.010650	0.011451	0.010468	0.012101	0.013562	0.011194	0.012309
$\bar{\lambda}$	9266.84	9256.64	9261.41	9259.14	9276.09	9277.39	9273.01	9268.67
F875M	0.006612	0.005185	0.005486	0.005035	0.005698	0.006350	0.005295	0.005937
$\bar{\lambda}$	8755.66	8749.57	8754.41	8754.59	8752.68	8754.67	8753.42	8746.07
F889N	0.000441	0.000338	0.000365	0.000336	0.000378	0.000423	0.000352	0.000381
$\bar{\lambda}$	8888.01	8887.95	8888.00	8888.01	8887.99	8888.02	8888.00	8887.90
F1042M	0.000867	0.000645	0.000698	0.000631	0.000813	0.000910	0.000741	0.000818
$\bar{\lambda}$	10161.00	10160.50	10160.40	10160.10	10170.30	10170.00	10169.50	10170.10
F1083N	0.000005	0.000004	0.000004	0.000003	0.000005	0.000006	0.000005	0.000005
$\bar{\lambda}$	10830.20	10830.10	10830.20	10830.20	10830.70	10830.50	10830.40	10830.70

Table 5.2 AB_V As a Function of Spectral Type and Wavelength

λ (Å)	sky	B0	A0	F0	G0	K0II	M0II	gE	Sa	Sbc	Scd	Irl
B-V	1.10	-0.31	0.00	0.27	0.58	1.07	1.60	1.00	0.80	0.60	0.45	0.30
1500	2.45	-1.60	2.22	7.22	8.90	13.0	15.0	6.82	5.40	4.03	2.67	1.77
2000	5.46	-1.50	1.35	4.10	6.35	10.3	12.3	6.41	4.80	3.18	2.29	1.40
2500	5.46	-1.20	1.11	3.11	4.61	8.11	9.36	5.43	4.10	2.86	2.15	1.36
3000	3.12	-0.78	1.21	1.99	2.46	5.46	6.21	3.63	3.00	2.46	1.76	1.24
3500	2.00	-0.62	1.00	1.38	1.63	2.13	4.63	2.49	2.01	1.54	1.35	0.94
4000	1.03	-0.46	-0.23	0.29	0.67	1.16	2.26	1.40	1.12	0.84	0.65	0.43
4500	0.55	-0.36	-0.16	0.06	0.26	0.46	0.96	0.55	0.44	0.34	0.28	0.34
5000	0.18	-0.22	-0.09	0.03	0.08	0.20	0.51	0.21	0.19	0.17	0.13	0.17
6000	-0.11	0.16	0.11	0.03	-0.04	-0.24	-0.46	-0.19	-0.17	-0.14	-0.11	0.13
7000	-0.33	0.46	0.22	0.05	-0.12	-0.42	-0.76	-0.52	-0.44	-0.37	-0.26	-0.04
8000	-0.55	0.76	0.33	0.08	-0.21	-0.61	-1.06	-0.81	-0.70	-0.60	-0.39	-0.21
9000	-0.65	0.96	0.36	0.09	-0.23	-0.66	-1.12	-1.07	-0.95	-0.84	-0.47	-0.33
10000	-0.75	1.17	0.40	0.10	-0.25	-0.72	-1.19	-1.29	-1.16	-1.04	-0.58	-0.45
11000	-1.01	1.37	0.43	0.11	-0.27	-0.75	-1.25	-1.51	-1.36	-1.21	-0.66	-0.51
12000	-1.11	1.57	0.45	0.12	-0.29	-0.78	-1.31	-1.69	-1.52	-1.35	-0.70	-0.54

In this system, the HST background (sky) may be estimated as

WFC ~ 28.0 + AB magnitudes $pixel^{-1}$

PC ~ 29.8 + AB magnitudes $pixel^{-1}$

Where the surface brightness of the sky has been taken as V = 23 magnitude $arcsec^{-2}$. The actual sky brightness depends on the heliocentric ecliptic latitude and longitude ($\lambda - \lambda_o$), in a manner summarized in Table 5.3 (taken from an early version of the F.O.S. Instrument Handbook by H. Ford).

Table 5.3 Sky Brightness

Ecliptic Latitude

$\lambda - \lambda_o$	0	30	60	90
180	22.1	22.7	23.2	23.3
145	22.4	22.9	23.3	23.3
110	22.3	22.9	23.3	23.3

5.2 EXTENDED SOURCES

For high-z galaxies, a much smaller fraction of light falls in the central pixel than for a stellar source. The magnitude difference between the light falling in the central pixel and the entire galaxy (without compensation for the OTA spherical aberration) is plotted against redshift in Figure 5.1, for giant elliptical galaxies. For other types of galaxies, a morphological term can be added to the values in Figure 5.1; for example, 0.6 magnitudes for lenticulars, 0.7 for S, 0.8 for Sab, 0.9 for Sbc, 1.2 for Scd, and 1.8 for Im. These values must be increased by an additional 1.2 magnitudes for the PC.

Figure 5.1 Giant Elliptical Galaxy

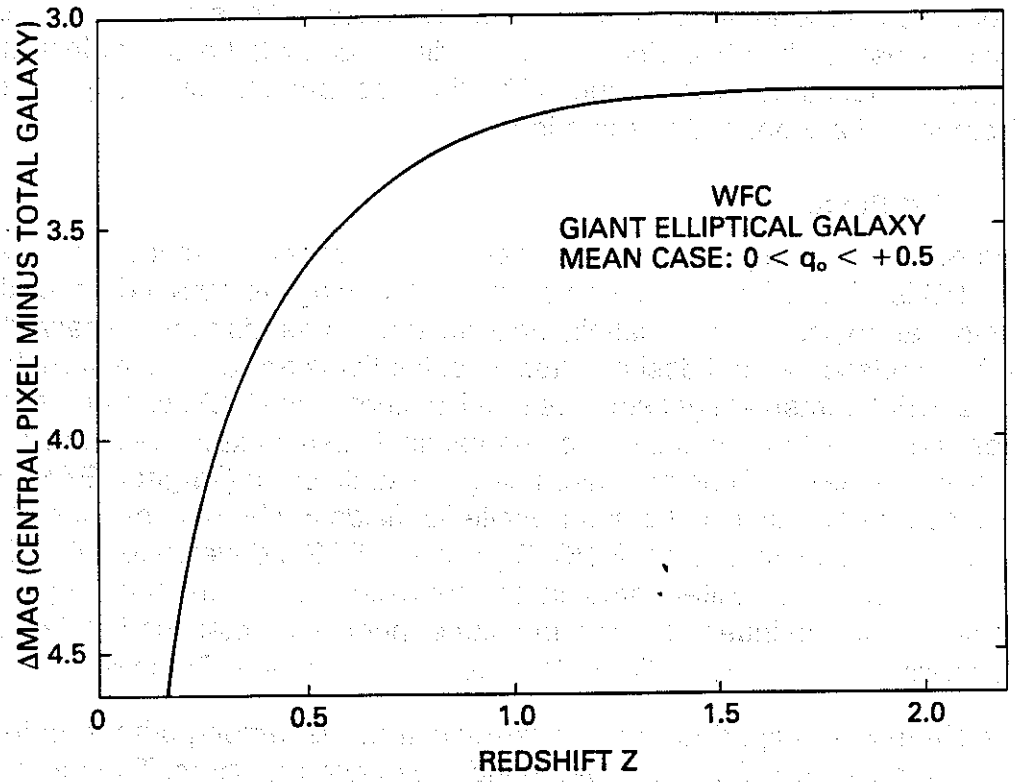

5.3 Compensation for Spherical Aberration

From the perspective of obtaining a given signal level, the inclusion of the effects of the Spherical Aberration in the calculation of exposure times are a straightforward aperture problem. Observations of isolated point sources require increases of a factor of ~5 in exposure time while observations of extended targets (e.g. a planet) require no increase in exposure time. However, what actually must be determined is the signal to noise (S/N) of the source of interest. This will usually require an understanding of the scene to be imaged. Obtaining archival images of similar scenes and constructing models using the PSF modeling software available from the STScI (the software packages "TIM" and "tinytim") is suggested.

6.0 CALIBRATION AND DATA REDUCTION

6.1 CALIBRATION OBSERVATIONS AND REFERENCE DATA

Standard calibration observations will be obtained and maintained in the calibration data base at the STScI. This includes those frames needed to operate the Post Observation Data Processing System (PODPS; usually just called the "pipeline"), a photometric calibration derived from standard star observations, and derived determinations of the plate scale distortion, grating dispersions, etc. The first set of these calibrations has been provided to the STScI by the WF/PC IDT from the Science Verification (SV) period, and will be maintained and updated thereafter by the STScI as part of the long term calibration program. These reference data will be maintained to a precision which is routinely attainable. For especially precise measurements, special calibration observations may need to be obtained as part of the observing proposal. Please consult the STScI Instrument Scientists for guidance if the routine calibration appears unlikely to support the requirements of a proposed observation.

6.1.1 Flat Fields

The removal of the pixel-to-pixel variation in the optical/electrical sensitivity of the WF/PC is usually known as flat-fielding or flattening. To obtain data for this, a "flat field" (an exposure of a spatially uniform source) needs to be observed through the telescope and desired filter. Real flat fields are always external; however, the WF/PC internal light sources that illuminate the CCDs can be used to monitor and correct for the stability of the flat fields using exposures called INTFLATs. Flat fields will be obtained using the sunlit earth (Target = EARTH-CALIB), as part of routine calibration. While flat fields will be obtained for all filters being used by observers, the WF/PC IDT and the STScI developed a list of frequently used Camera - Filter combinations for calibration during the SV period. These filters will continue to receive the higher priority in obtaining flat field and will generally have a better calibration. This list is included in Table 6.1.

The Earth is an imperfect flat field target in that it is, among other problems, too bright for the WF/PC in the broad-band green and red filters. Therefore it has been necessary to combine the broad-band filters with neutral density filters (either F8ND or F122M) and attempt to remove the artifacts introduced by these filters with image processing. The rapid motion of the HST also creates streaks across the flat field images. The removal of the streaks requires the combination of multiple earth observations with the streaks at different angles on the CCDs. An extensive discussion of the generation of flat fields is available in Chapter 6 of the IDT OV/SV Report.

Table 6.1 WFC Flat Field SV Calibrations

F194W	F230W	F284W	F336W	F375N	F439W	F487N
F502N	F547M	F555W	F622W	F631N	F656N	F658N
F664N	F673N	F702W	F785LP	F889N		

Table 6.2 PC Flat Field SV Calibrations

F230W	F284W	F336W	F375N	F439W	F469N	F487N
F502N	F517N	F547M	F555W	F622W	F656N	F658N
F664N	F673N	F702W	F718M	F785LP	F889N	

6.1.2 Dark Frames

Dark frames are long exposures that are taken with no light incident on the CCDs. They are used to detect CCD counts (the dark current) caused by thermal generation (at the interfaces between the silicon and oxide layers) as well as the rate of charged particle and secondary radiation events. At the normal CCD operating temperature, the "dark current" is 0.003 electrons/pixel/second, except for several hours after a "purge" used to ameliorate the residual image problem (see Section 4.7.2).

6.1.3 Bias Frames

Bias frames are readouts of the CCDs without an exposure (so the dark current is negligible). They are used to measure the bias built into the system to ensure that the ADC input is above zero and, hence, to determine the pedestal for a zero signal.

6.1.4 Kelsall Spots (K-spots)

Kelsall spots can be imposed on any type of frame to find relative motions between CCDs. They also aid in registration of four frames (one per CCD) as a celestial scene. Normally, however, a separate frame will be taken for them because the "Baum Spot" badly saturates WFC4 or PC8.

6.2 DATA REDUCTION AND DATA PRODUCTS

The routine processing of WF/PC science data consists of the pipeline functions described in Section 6.2.1. The resulting images will be available on magnetic tape in FITS format, and as photographic prints. The reformatted raw data will also be available, along with the relevant calibration data. The STSDAS Calibration Guide should be consulted for a more complete description than the summary presented here.

6.2.1 Pipeline Processing

The PODPS pipeline processing of WF/PC datasets reformats the telemetry received from HST into STSDAS format images, generates headers containing a large number of keywords taken from both the HST and WF/PC telemetry streams in addition to various STScI ground system databases, and applies the calibration described below. This calibration is done with a module known as "calwfp" which is written in the IRAF SPP language and is available, in identical form, to users of the STSDAS system. Therefore, off-line recalibration of observations is fairly easy and will use the same program as the PODPS system.

CALWFP currently performs the following operations if required by the observation:

- Statistical Correction for problem in analog-to-digital conversion
- Bias level removal (with Odd&Even columns corrected in FULL Mode)
- Bias image subtraction
- Preflash image scaling and subtraction
- Charge Transfer Efficiency (CTE) Fixup (for images without Preflash)
- Dark image scaling and subtraction
- Purge residual image scaling and subtraction
- Flat field image correction
- Population of various photometric calibration keywords

In addition, the following conditions are flagged in the Data Quality File (DQF):

- Transmission failures and possible failures
- Known bad pixels (e.g. blocked columns)
- Pixels at the maximum A/D converter level (i.e. saturated)
- Bad pixels in reference images

The following histograms are generated:

- Input image
- After A to D fixup
- Output image

6.2.2 Data Formats

Data will be supplied to observers on FITS tapes. The following are currently considered part of a data set:

• Edited Image and DQF (uncalibrated)	.d0h, .q0h
• Standard Header Packet	.shh
• Extracted Engineering Data and DQF	.x0h,.q1h
• Trailer File (ascii file)	.trl
• Calibrated Image and DQF	.c0h, .c1h
• Histograms File	.c2h

Further data reduction and analysis may be performed under the STScI's science data analysis software system (STSDAS). Standard routines are or will be available, operating under IRAF, for the analysis of data for image photometry, spectral analysis, astrometry, and the generation of the calibration data files.

A. Appendix

A.1 Complete Photometric Parameters for Each Filter

F122M	W1	W2	W3	W4	P5	P6	P7	P8
$\int QT d\lambda/\lambda$	0.000123	0.000123	0.000118	0.000111	0.000099	0.000075	0.000095	0.000113
$\bar{\lambda}$	3023.27	2909.33	2978.55	2946.95	3046.88	3669.81	3133.16	3349.59
$\delta\bar{\lambda}$	3560.54	3314.90	3392.70	3452.60	3847.38	4420.64	3941.88	3744.36
σ	0.50013	0.48386	0.48371	0.49753	0.53623	0.51155	0.53427	0.47471
QT_{max}	0.000164	0.000172	0.000164	0.000149	0.000091	0.000060	0.000080	0.000103
$d\bar{\lambda}/d\alpha$	756.207	681.132	696.903	729.464	876.111	960.310	894.354	754.829
λ_p	3933.98	3750.12	3828.68	3828.45	4054.49	4650.16	4119.29	4182.02
$\langle\lambda\rangle$	4490.30	4269.23	4349.82	4367.81	4658.58	5192.79	4695.46	4661.25
λ_{max}	2465.00	2350.00	2465.00	2341.00	2515.00	2585.00	2585.00	2320.00

F128LP	W1	W2	W3	W4	P5	P6	P7	P8
$\int QT d\lambda/\lambda$	0.156659	0.141458	0.142671	0.134928	0.137361	0.141405	0.140181	0.173929
$\bar{\lambda}$	5346.23	5181.04	5215.70	5259.76	5474.49	5680.78	5426.38	5267.19
$\delta\bar{\lambda}$	4627.73	4577.64	4569.90	4525.10	4486.36	4270.07	4275.59	4162.18
σ	0.36759	0.37520	0.37208	0.36535	0.34801	0.31920	0.33460	0.33557
QT_{max}	0.202880	0.176779	0.178635	0.178044	0.183317	0.198531	0.193528	0.230696
$d\bar{\lambda}/d\alpha$	722.392	729.376	722.081	702.061	663.024	578.824	607.529	593.125
λ_p	5999.11	5846.60	5877.46	5896.24	6072.53	6212.57	5986.24	5831.17
$\langle\lambda\rangle$	6324.61	6180.58	6210.24	6214.14	6369.71	6478.12	6267.37	6119.14
λ_{max}	5800.00	5800.00	5800.00	5760.00	6050.00	5800.00	5720.00	5700.00

F157W	W1	W2	W3	W4	P5	P6	P7	P8
$\int QT d\lambda/\lambda$	0.0000090	0.000094	0.000086	0.000086	0.000085	0.000042	0.000078	0.000068
$\bar{\lambda}$	1974.85	1943.41	1979.01	1934.95	1885.19	2195.08	1902.45	2136.73
$\delta\bar{\lambda}$	1810.20	1689.72	1773.92	1709.74	1687.99	2477.94	1758.82	2140.14
σ	0.38925	0.36922	0.38065	0.37523	0.38024	0.47938	0.39260	0.42534
QT_{max}	0.000277	0.000296	0.000259	0.000277	0.000298	0.000109	0.000275	0.000164
$d\bar{\lambda}/d\alpha$	299.229	264.940	286.750	272.443	272.563	504.447	293.233	386.562
λ_p	2502.20	2404.41	2472.38	2416.61	2404.88	3016.37	2448.42	2758.40
$\langle\lambda\rangle$	2882.28	2731.85	2822.74	2761.97	2790.85	3605.01	2851.50	3192.26
λ_{max}	1490.00	1490.00	1490.00	1490.00	1490.00	1490.00	1490.00	1493.00

F194W	W1	W2	W3	W4	P5	P6	P7	P8
$\int QT d\lambda/\lambda$	0.000269	0.000284	0.000263	0.000251	0.000231	0.000125	0.000203	0.000236
$\bar{\lambda}$	2069.10	2067.94	2071.40	2064.76	2006.52	2030.14	2004.70	2035.34
$\delta\bar{\lambda}$	502.63	496.35	499.48	497.93	487.13	522.59	490.98	487.62
σ	0.10316	0.10193	0.10240	0.10241	0.10310	0.10931	0.10401	0.10174
QT_{max}	0.001273	0.001344	0.001247	0.001183	0.000946	0.000527	0.000828	0.001019
$d\bar{\lambda}/d\alpha$	22.019	21.485	21.720	21.655	21.327	24.259	21.686	21.067
λ_p	2096.04	2093.21	2097.37	2090.55	2033.68	2065.47	2032.64	2062.29
$\langle\lambda\rangle$	2111.29	2107.23	2111.89	2104.94	2049.33	2087.10	2048.83	2077.85
λ_{max}	2120.00	2120.00	2120.00	2119.00	2035.00	2040.00	2035.00	2047.00

F230W	W1	W2	W3	W4	P5	P6	P7	P8
$\int QT d\lambda/\lambda$	0.001162	0.001223	0.001154	0.001058	0.000660	0.000412	0.000575	0.000772
$\bar{\lambda}$	2348.24	2347.86	2349.48	2346.24	2344.65	2350.28	2345.36	2341.66
$\delta\bar{\lambda}$	357.36	357.05	357.71	356.65	375.84	378.94	377.52	373.44
σ	0.06463	0.06458	0.06466	0.06455	0.06807	0.06847	0.06835	0.06772
QT_{max}	0.006207	0.006522	0.006189	0.005613	0.003408	0.002149	0.002972	0.004023
$d\bar{\lambda}/d\alpha$	9.807	9.792	9.821	9.777	10.864	11.018	10.958	10.740
λ_p	2358.21	2357.80	2359.46	2356.17	2355.71	2361.60	2356.54	2352.65
$\langle\lambda\rangle$	2363.25	2362.82	2364.50	2361.19	2361.32	2367.37	2362.20	2358.23
λ_{max}	2425.00	2425.00	2430.00	2425.00	2435.00	2440.00	2437.00	2230.00

F284W	W1	W2	W3	W4	P5	P6	P7	P8
$\int QT d\lambda/\lambda$	0.002333	0.002439	0.002374	0.002060	0.001570	0.001144	0.001424	0.001952
$\bar{\lambda}$	2821.84	2821.39	2823.96	2820.32	2841.08	2859.07	2848.21	2859.85
$\delta\bar{\lambda}$	485.70	485.46	485.58	486.80	493.79	498.67	500.20	506.89
σ	0.07309	0.07307	0.07302	0.07330	0.07381	0.07407	0.07458	0.07527
QT_{max}	0.013707	0.014321	0.013907	0.012040	0.009107	0.006484	0.008088	0.010842
$d\bar{\lambda}/d\alpha$	15.076	15.064	15.057	15.153	15.477	15.685	15.842	16.202
λ_p	2836.95	2836.47	2839.05	2835.49	2856.55	2874.83	2864.05	2876.08
$\langle\lambda\rangle$	2844.54	2844.05	2846.63	2843.11	2864.31	2882.77	2872.01	2884.23
λ_{max}	2790.00	2790.00	2790.00	2785.00	2810.00	2820.00	2815.00	2820.00

F336W	W1	W2	W3	W4	P5	P6	P7	P8
$\int QT d\lambda/\lambda$	0.004206	0.004357	0.004364	0.003674	0.003470	0.003134	0.003523	0.005683
$\bar{\lambda}$	3353.53	3352.45	3353.83	3353.73	3361.98	3372.60	3369.38	3378.02
$\delta\bar{\lambda}$	409.83	409.32	409.35	410.71	408.37	405.78	409.33	406.31
σ	0.05190	0.05185	0.05183	0.05201	0.05158	0.05109	0.05159	0.05108
QT_{max}	0.029323	0.030414	0.030478	0.025552	0.024350	0.022269	0.024727	0.040323
$d\bar{\lambda}/d\alpha$	9.032	9.012	9.010	9.071	8.945	8.804	8.968	8.813
λ_p	3362.55	3361.45	3362.83	3362.78	3370.90	3381.37	3378.32	3386.79
$<\lambda>$	3367.06	3365.95	3367.33	3367.31	3375.36	3385.75	3382.79	3391.17
λ_{max}	3360.00	3360.00	3360.00	3360.00	3380.00	3380.00	3380.00	3390.00

F368M	W1	W2	W3	W4	P5	P6	P7	P8
$\int QT d\lambda/\lambda$	0.001922	0.001959	0.001991	0.001698	0.001696	0.001649	0.001884	0.003176
$\bar{\lambda}$	3687.64	3687.06	3687.33	3688.46	3687.96	3687.20	3691.09	3689.08
$\delta\bar{\lambda}$	196.80	195.37	198.36	195.53	203.70	214.07	210.33	215.75
σ	0.02266	0.02250	0.02284	0.02251	0.02346	0.02465	0.02420	0.02484
QT_{max}	0.025600	0.026047	0.026502	0.022657	0.022629	0.022123	0.025315	0.042842
$d\bar{\lambda}/d\alpha$	1.894	1.867	1.924	1.869	2.029	2.241	2.161	2.275
λ_p	3689.72	3689.12	3689.43	3690.53	3690.15	3689.54	3693.38	3691.44
$<\lambda>$	3690.80	3690.19	3690.52	3691.61	3691.29	3690.72	3694.56	3692.64
λ_{max}	3710.00	3710.00	3710.00	3710.00	3710.00	3710.00	3710.00	3710.00

F375N	W1	W2	W3	W4	P5	P6	P7	P8
$\int QT d\lambda/\lambda$	0.000675	0.000685	0.000698	0.000600	0.000598	0.000581	0.000680	0.001135
$\bar{\lambda}$	3755.34	3755.26	3755.31	3755.45	3755.41	3755.25	3755.86	3755.50
$\delta\bar{\lambda}$	83.46	83.45	83.46	83.47	83.49	83.43	83.56	83.47
σ	0.00944	0.00944	0.00944	0.00944	0.00944	0.00944	0.00945	0.00944
QT_{max}	0.024926	0.025317	0.025785	0.022125	0.022064	0.021489	0.024960	0.041862
$d\bar{\lambda}/d\alpha$	0.335	0.334	0.334	0.335	0.335	0.334	0.335	0.335
λ_p	3755.67	3755.60	3755.64	3755.79	3755.74	3755.58	3756.20	3755.83
$\langle\lambda\rangle$	3755.84	3755.77	3755.81	3755.96	3755.91	3755.75	3756.36	3756.00
λ_{max}	3740.00	3740.00	3740.00	3740.00	3740.00	3740.00	3740.00	3740.00

F413M	W1	W2	W3	W4	P5	P6	P7	P8
$\int QT d\lambda/\lambda$	0.003913	0.003858	0.003972	0.003545	0.003603	0.003333	0.004449	0.006606
$\bar{\lambda}$	4124.70	4123.40	4123.47	4125.05	4125.42	4125.69	4125.59	4122.27
$\delta\bar{\lambda}$	250.00	249.65	249.49	249.92	249.41	251.21	247.92	248.33
σ	0.02574	0.02571	0.02569	0.02573	0.02567	0.02586	0.02552	0.02558
QT_{max}	0.053577	0.052386	0.053961	0.048696	0.049468	0.045478	0.061389	0.088745
$d\bar{\lambda}/d\alpha$	2.733	2.726	2.722	2.731	2.719	2.759	2.687	2.698
λ_p	4127.43	4126.12	4126.19	4127.78	4128.14	4128.45	4128.27	4124.96
$\langle\lambda\rangle$	4128.79	4127.48	4127.55	4129.15	4129.50	4129.83	4129.62	4126.31
λ_{max}	4200.00	4200.00	4200.00	4200.00	4200.00	4200.00	4200.00	4100.00

F437N	W1	W2	W3	W4	P5	P6	P7	P8
$\int QT d\lambda/\lambda$	0.000255	0.000243	0.000250	0.000232	0.000236	0.000229	0.000284	0.000400
$\bar{\lambda}$	4365.78	4365.76	4365.76	4365.78	4365.78	4365.80	4365.76	4365.74
$\delta\bar{\lambda}$	21.92	21.93	21.93	21.92	21.92	21.92	21.93	21.93
σ	0.00213	0.00213	0.00213	0.00213	0.00213	0.00213	0.00213	0.00213
QT_{max}	0.050400	0.048032	0.049396	0.045887	0.046749	0.045236	0.056193	0.079056
$d\bar{\lambda}/d\alpha$	0.020	0.020	0.020	0.020	0.020	0.020	0.020	0.020
λ_p	4365.80	4365.78	4365.78	4365.80	4365.80	4365.82	4365.78	4365.76
$<\lambda>$	4365.81	4365.79	4365.79	4365.81	4365.81	4365.83	4365.79	4365.77
λ_{max}	4366.00	4366.00	4366.00	4366.00	4366.00	4366.00	4366.00	4366.00

F439W	W1	W2	W3	W4	P5	P6	P7	P8
$\int QT d\lambda/\lambda$	0.010020	0.009569	0.009836	0.009112	0.009257	0.008974	0.011089	0.015633
$\bar{\lambda}$	4353.17	4347.63	4347.26	4353.68	4353.20	4361.85	4347.14	4338.06
$\delta\bar{\lambda}$	467.44	467.38	467.19	467.11	466.46	467.73	464.58	464.44
σ	0.04560	0.04565	0.04564	0.04556	0.04550	0.04554	0.04538	0.04546
QT_{max}	0.073829	0.067997	0.069689	0.067290	0.067997	0.069966	0.079042	0.110662
$d\bar{\lambda}/d\alpha$	9.052	9.061	9.054	9.038	9.014	9.045	8.954	8.967
λ_p	4362.19	4356.66	4356.29	4362.68	4362.18	4370.85	4356.07	4347.02
$<\lambda>$	4366.69	4361.18	4360.81	4367.18	4366.67	4375.34	4360.54	4351.50
λ_{max}	4610.00	4610.00	4610.00	4610.00	4610.00	4610.00	4400.00	4390.00

F469N	W1	W2	W3	W4	P5	P6	P7	P8
$\int QT d\lambda/\lambda$	0.000478	0.000436	0.000447	0.000436	0.000439	0.000458	0.000495	0.000641
$\bar{\lambda}$	4687.16	4687.15	4687.14	4687.16	4687.15	4687.18	4687.13	4687.09
$\delta\bar{\lambda}$	27.61	27.61	27.61	27.61	27.61	27.61	27.61	27.60
σ	0.00250	0.00250	0.00250	0.00250	0.00250	0.00250	0.00250	0.00250
QT_{max}	0.083413	0.076095	0.077916	0.075993	0.076496	0.079958	0.086248	0.111784
$d\bar{\lambda}/d\alpha$	0.029	0.029	0.029	0.029	0.029	0.029	0.029	0.029
λ_p	4687.19	4687.18	4687.17	4687.19	4687.18	4687.21	4687.16	4687.12
$<\lambda>$	4687.21	4687.19	4687.19	4687.20	4687.20	4687.22	4687.17	4687.13
λ_{max}	4688.00	4688.00	4688.00	4688.00	4688.00	4688.00	4688.00	4688.00

F487N	W1	W2	W3	W4	P5	P6	P7	P8
$\int QT d\lambda/\lambda$	0.000628	0.000563	0.000575	0.000570	0.000571	0.000613	0.000626	0.000773
$\bar{\lambda}$	4868.56	4868.55	4868.54	4868.56	4868.55	4868.57	4868.53	4868.49
$\delta\bar{\lambda}$	31.09	31.10	31.10	31.09	31.09	31.09	31.10	31.12
σ	0.00271	0.00271	0.00271	0.00271	0.00271	0.00271	0.00271	0.00271
QT_{max}	0.093861	0.084149	0.085880	0.085182	0.085290	0.091572	0.093513	0.115569
$d\bar{\lambda}/d\alpha$	0.036	0.036	0.036	0.036	0.036	0.036	0.036	0.036
λ_p	4868.60	4868.58	4868.58	4868.59	4868.59	4868.61	4868.57	4868.53
$<\lambda>$	4868.61	4868.60	4868.60	4868.61	4868.61	4868.63	4868.58	4868.54
λ_{max}	4868.00	4868.00	4868.00	4868.00	4868.00	4868.00	4868.00	4868.00

F492M	W1	W2	W3	W4	P5	P6	P7	P8
$\int QT d\lambda/\lambda$	0.010044	0.008995	0.009173	0.009094	0.009125	0.009797	0.009998	0.012351
$\bar{\lambda}$	4908.78	4907.05	4906.62	4908.01	4907.96	4910.26	4905.36	4900.92
$\delta\bar{\lambda}$	364.47	364.65	364.60	364.21	364.63	364.05	365.03	365.63
σ	0.03153	0.03156	0.03156	0.03151	0.03155	0.03148	0.03160	0.03168
QT_{max}	0.102141	0.091510	0.093389	0.092644	0.092758	0.099994	0.101723	0.126467
$d\bar{\lambda}/d\alpha$	4.880	4.887	4.886	4.874	4.885	4.868	4.899	4.919
λ_p	4913.66	4911.95	4911.51	4912.89	4912.85	4915.13	4910.26	4905.84
$\langle\lambda\rangle$	4916.11	4914.39	4913.96	4915.33	4915.30	4917.57	4912.71	4908.31
λ_{max}	4910.00	4870.00	4870.00	4870.00	4870.00	4930.00	4860.00	4840.00

F502N	W1	W2	W3	W4	P5	P6	P7	P8
$\int QT d\lambda/\lambda$	0.000651	0.000578	0.000588	0.000588	0.000589	0.000640	0.000636	0.000767
$\bar{\lambda}$	5018.53	5018.52	5018.52	5018.52	5018.53	5018.53	5018.52	5018.50
$\delta\bar{\lambda}$	29.67	29.67	29.67	29.67	29.67	29.66	29.67	29.69
σ	0.00251	0.00251	0.00251	0.00251	0.00251	0.00251	0.00251	0.00251
QT_{max}	0.110620	0.098224	0.099952	0.099858	0.100056	0.108762	0.108135	0.130325
$d\bar{\lambda}/d\alpha$	0.032	0.032	0.032	0.032	0.032	0.032	0.032	0.032
λ_p	5018.56	5018.55	5018.55	5018.55	5018.56	5018.57	5018.55	5018.53
$\langle\lambda\rangle$	5018.58	5018.57	5018.57	5018.57	5018.57	5018.58	5018.56	5018.55
λ_{max}	5015.00	5015.00	5015.00	5015.00	5015.00	5015.00	5015.00	5015.00

F517N	W1	W2	W3	W4	P5	P6	P7	P8
$\int QT d\lambda/\lambda$	0.002609	0.002301	0.002336	0.002339	0.002355	0.002572	0.002526	0.003011
$\bar{\lambda}$	5170.14	5170.09	5170.07	5170.08	5170.13	5170.15	5170.08	5170.04
$\delta\bar{\lambda}$	88.23	88.23	88.23	88.23	88.23	88.22	88.24	88.26
σ	0.00725	0.00725	0.00725	0.00725	0.00725	0.00725	0.00725	0.00725
QT_{max}	0.121721	0.107395	0.109045	0.109195	0.109881	0.120018	0.117878	0.140568
$d\bar{\lambda}/d\alpha$	0.272	0.272	0.272	0.272	0.272	0.271	0.272	0.272
λ_p	5170.41	5170.36	5170.34	5170.35	5170.40	5170.42	5170.36	5170.31
$<\lambda>$	5170.55	5170.50	5170.48	5170.49	5170.54	5170.56	5170.49	5170.45
λ_{max}	5160.00	5160.00	5160.00	5160.00	5160.00	5160.00	5160.00	5160.00

F569W	W1	W2	W3	W4	P5	P6	P7	P8
$\int QT d\lambda/\lambda$	0.038977	0.034144	0.034536	0.034431	0.035264	0.038327	0.037255	0.044115
$\bar{\lambda}$	5599.23	5596.89	5595.39	5593.83	5600.68	5599.77	5592.21	5585.60
$\delta\bar{\lambda}$	967.47	968.43	967.43	964.36	970.77	969.12	962.22	955.54
σ	0.07338	0.07348	0.07342	0.07321	0.07361	0.07349	0.07307	0.07265
QT_{max}	0.189915	0.166323	0.168342	0.168368	0.171396	0.186793	0.182914	0.218444
$d\bar{\lambda}/d\alpha$	30.146	30.218	30.164	29.982	30.344	30.246	29.857	29.479
λ_p	5629.95	5627.68	5626.13	5624.39	5631.60	5630.61	5622.64	5615.62
$<\lambda>$	5645.49	5643.27	5641.68	5639.86	5647.25	5646.22	5638.03	5630.80
λ_{max}	5460.00	5460.00	5420.00	5420.00	5460.00	5460.00	5460.00	5460.00

F588N	W1	W2	W3	W4	P5	P6	P7	P8
$\int QT d\lambda/\lambda$	0.000886	0.000771	0.000779	0.000776	0.000800	0.000866	0.000840	0.000993
$\bar{\lambda}$	5879.83	5879.83	5879.83	5879.82	5879.83	5879.83	5879.81	5879.79
$\delta\bar{\lambda}$	42.64	42.64	42.64	42.64	42.64	42.64	42.63	42.63
σ	0.00308	0.00308	0.00308	0.00308	0.00308	0.00308	0.00308	0.00308
QT_{max}	0.119791	0.104330	0.105385	0.104922	0.108223	0.117202	0.113658	0.134333
$d\bar{\lambda}/d\alpha$	0.056	0.056	0.056	0.056	0.056	0.056	0.056	0.056
λ_p	5879.89	5879.88	5879.88	5879.88	5879.89	5879.88	5879.87	5879.85
$<\lambda>$	5879.91	5879.91	5879.91	5879.91	5879.92	5879.91	5879.90	5879.88
λ_{max}	5877.00	5877.00	5877.00	5877.00	5877.00	5877.00	5877.00	5877.00

F606W	W1	W2	W3	W4	P5	P6	P7	P8
$\int QT d\lambda/\lambda$	0.068987	0.060471	0.061009	0.060434	0.062883	0.068153	0.065197	0.076240
$\bar{\lambda}$	5844.45	5839.19	5834.57	5830.22	5850.31	5851.48	5822.46	5797.69
$\delta\bar{\lambda}$	1536.94	1541.29	1540.21	1533.85	1544.17	1541.62	1533.38	1526.83
σ	0.11168	0.11209	0.11210	0.11172	0.11209	0.11188	0.11184	0.11184
QT_{max}	0.209153	0.182077	0.183587	0.182330	0.189580	0.205076	0.196185	0.228465
$d\bar{\lambda}/d\alpha$	72.888	73.367	73.322	72.772	73.502	73.244	72.825	72.513
λ_p	5916.77	5912.00	5907.37	5902.52	5923.18	5924.12	5894.86	5869.94
$<\lambda>$	5952.96	5948.46	5943.83	5938.74	5959.64	5960.47	5931.14	5906.19
λ_{max}	6080.00	6080.00	6080.00	6080.00	6080.00	6080.00	6080.00	6080.00

F622W	W1	W2	W3	W4	P5	P6	P7	P8
$\int QT d\lambda/\lambda$	0.041917	0.036557	0.036794	0.036417	0.038226	0.041421	0.039146	0.045212
$\bar{\lambda}$	6129.90	6129.26	6127.33	6124.51	6134.14	6134.40	6120.14	6107.34
$\delta\bar{\lambda}$	984.22	987.45	987.06	982.86	987.34	985.15	985.50	987.30
σ	0.06818	0.06841	0.06841	0.06815	0.06835	0.06820	0.06838	0.06865
QT_{max}	0.211607	0.184207	0.185830	0.184679	0.191593	0.207272	0.199047	0.232746
$d\bar{\lambda}/d\alpha$	28.498	28.688	28.675	28.444	28.659	28.531	28.618	28.782
λ_p	6158.21	6157.72	6155.78	6152.76	6162.59	6162.75	6148.53	6135.86
$<\lambda>$	6172.35	6171.93	6169.98	6166.87	6176.80	6176.92	6162.71	6150.09
λ_{max}	6030.00	6030.00	6030.00	6030.00	6030.00	6030.00	6030.00	6030.00

F631N	W1	W2	W3	W4	P5	P6	P7	P8
$\int QT d\lambda/\lambda$	0.000446	0.000388	0.000391	0.000386	0.000407	0.000440	0.000413	0.000471
$\bar{\lambda}$	6306.26	6306.26	6306.26	6306.26	6306.27	6306.27	6306.25	6306.24
$\delta\bar{\lambda}$	29.76	29.76	29.76	29.77	29.76	29.76	29.77	29.77
σ	0.00200	0.00200	0.00200	0.00200	0.00200	0.00200	0.00200	0.00200
QT_{max}	0.095885	0.083546	0.084011	0.083068	0.087523	0.094696	0.088804	0.101340
$d\bar{\lambda}/d\alpha$	0.025	0.025	0.025	0.025	0.025	0.025	0.025	0.025
λ_p	6306.29	6306.29	6306.29	6306.28	6306.29	6306.29	6306.28	6306.26
$<\lambda>$	6306.30	6306.30	6306.30	6306.29	6306.31	6306.31	6306.29	6306.28
λ_{max}	6305.00	6305.00	6305.00	6305.00	6305.00	6305.00	6305.00	6305.00

F648M	W1	W2	W3	W4	P5	P6	P7	P8
$\int QT d\lambda/\lambda$	0.008108	0.007070	0.007091	0.006981	0.007453	0.008072	0.007437	0.008365
$\bar{\lambda}$	6467.88	6467.99	6467.60	6466.93	6468.93	6469.08	6466.42	6464.26
$\delta\bar{\lambda}$	371.00	371.01	370.89	370.63	371.32	371.39	370.57	370.10
σ	0.02436	0.02436	0.02435	0.02434	0.02438	0.02438	0.02434	0.02431
QT_{max}	0.112892	0.098358	0.098926	0.097847	0.102991	0.111426	0.104645	0.119585
$d\bar{\lambda}/d\alpha$	3.838	3.838	3.836	3.831	3.844	3.845	3.830	3.821
λ_p	6471.73	6471.83	6471.44	6470.77	6472.79	6472.94	6470.26	6468.09
$\langle\lambda\rangle$	6473.65	6473.76	6473.37	6472.70	6474.72	6474.87	6472.18	6470.01
λ_{max}	6290.00	6290.00	6290.00	6290.00	6290.00	6290.00	6290.00	6290.00

F656N	W1	W2	W3	W4	P5	P6	P7	P8
$\int QT d\lambda/\lambda$	0.000242	0.000211	0.000211	0.000207	0.000223	0.000241	0.000220	0.000246
$\bar{\lambda}$	6558.84	6558.84	6558.84	6558.84	6558.84	6558.84	6558.83	6558.83
$\delta\bar{\lambda}$	19.82	19.82	19.82	19.83	19.82	19.82	19.83	19.83
σ	0.00128	0.00128	0.00128	0.00128	0.00128	0.00128	0.00128	0.00128
QT_{max}	0.082840	0.072269	0.072385	0.071116	0.076435	0.082818	0.075596	0.084301
$d\bar{\lambda}/d\alpha$	0.011	0.011	0.011	0.011	0.011	0.011	0.011	0.011
λ_p	6558.85	6558.85	6558.85	6558.85	6558.85	6558.85	6558.85	6558.84
$\langle\lambda\rangle$	6558.86	6558.86	6558.86	6558.85	6558.86	6558.86	6558.85	6558.85
λ_{max}	6559.00	6559.00	6559.00	6559.00	6559.00	6559.00	6559.00	6559.00

F658N	W1	W2	W3	W4	P5	P6	P7	P8
$\int QT d\lambda/\lambda$	0.000239	0.000209	0.000209	0.000205	0.000221	0.000239	0.000218	0.000243
$\bar{\lambda}$	6576.45	6576.45	6576.45	6576.45	6576.46	6576.46	6576.45	6576.44
$\delta\bar{\lambda}$	20.01	20.01	20.01	20.01	20.01	20.01	20.01	20.01
σ	0.00129	0.00129	0.00129	0.00129	0.00129	0.00129	0.00129	0.00129
QT_{max}	0.082834	0.072271	0.072368	0.071063	0.076488	0.082885	0.075514	0.084086
$d\bar{\lambda}/d\alpha$	0.011	0.011	0.011	0.011	0.011	0.011	0.011	0.011
λ_p	6576.46	6576.46	6576.46	6576.46	6576.47	6576.47	6576.46	6576.45
$<\lambda>$	6576.47	6576.47	6576.47	6576.47	6576.47	6576.47	6576.46	6576.46
λ_{max}	6576.00	6576.00	6576.00	6576.00	6576.00	6576.00	6576.00	6576.00

F664N	W1	W2	W3	W4	P5	P6	P7	P8
$\int QT d\lambda/\lambda$	0.002703	0.002359	0.002360	0.002313	0.002503	0.002713	0.002455	0.002721
$\bar{\lambda}$	6637.00	6637.01	6636.96	6636.86	6637.14	6637.16	6636.81	6636.57
$\delta\bar{\lambda}$	131.71	131.71	131.70	131.70	131.71	131.71	131.70	131.70
σ	0.00843	0.00843	0.00843	0.00843	0.00843	0.00843	0.00843	0.00843
QT_{max}	0.106247	0.092710	0.092800	0.091060	0.098213	0.106446	0.096719	0.107470
$d\bar{\lambda}/d\alpha$	0.471	0.471	0.471	0.471	0.471	0.471	0.471	0.471
λ_p	6637.47	6637.48	6637.43	6637.33	6637.61	6637.64	6637.28	6637.04
$<\lambda>$	6637.71	6637.72	6637.67	6637.57	6637.85	6637.87	6637.52	6637.27
λ_{max}	6600.00	6600.00	6600.00	6600.00	6600.00	6601.00	6600.00	6600.00

F673N	W1	W2	W3	W4	P5	P6	P7	P8
$\int QT d\lambda/\lambda$	0.001105	0.000965	0.000964	0.000942	0.001027	0.001114	0.000999	0.001100
$\bar{\lambda}$	6722.56	6722.56	6722.56	6722.54	6722.58	6722.59	6722.54	6722.51
$\delta\bar{\lambda}$	50.41	50.41	50.41	50.41	50.40	50.40	50.42	50.44
σ	0.00318	0.00318	0.00318	0.00318	0.00318	0.00318	0.00318	0.00319
QT_{max}	0.157864	0.137787	0.137660	0.134568	0.146690	0.159123	0.142672	0.157126
$d\bar{\lambda}/d\alpha$	0.068	0.068	0.068	0.068	0.068	0.068	0.068	0.068
λ_p	6722.63	6722.63	6722.62	6722.61	6722.65	6722.65	6722.60	6722.57
$\langle\lambda\rangle$	6722.67	6722.67	6722.66	6722.64	6722.69	6722.69	6722.64	6722.61
λ_{max}	6718.00	6718.00	6718.00	6718.00	6718.00	6718.00	6718.00	6718.00

F675W	W1	W2	W3	W4	P5	P6	P7	P8
$\int QT d\lambda/\lambda$	0.031871	0.027767	0.027762	0.027116	0.029512	0.032011	0.028851	0.032174
$\bar{\lambda}$	6674.73	6674.40	6672.29	6667.30	6679.57	6680.43	6665.71	6658.00
$\delta\bar{\lambda}$	905.67	904.76	904.11	901.24	906.27	906.62	901.94	903.23
σ	0.05762	0.05757	0.05754	0.05740	0.05762	0.05763	0.05746	0.05761
QT_{max}	0.186825	0.162839	0.163540	0.161402	0.171108	0.185212	0.172170	0.195006
$d\bar{\lambda}/d\alpha$	22.161	22.118	22.093	21.969	22.174	22.189	22.008	22.097
λ_p	6697.05	6696.68	6694.54	6689.44	6701.89	6702.76	6687.90	6680.30
$\langle\lambda\rangle$	6708.27	6707.88	6705.73	6700.58	6713.10	6713.98	6699.05	6691.51
λ_{max}	6390.00	6390.00	6390.00	6390.00	6390.00	6390.00	6390.00	6380.00

F702W	W1	W2	W3	W4	P5	P6	P7	P8
$\int QT d\lambda/\lambda$	0.049598	0.042984	0.042981	0.041618	0.045807	0.049755	0.044336	0.049853
$\bar{\lambda}$	6867.70	6861.76	6859.79	6845.56	6870.61	6872.95	6843.74	6840.00
$\delta\bar{\lambda}$	1473.17	1462.57	1465.89	1454.24	1464.48	1466.76	1456.11	1470.81
σ	0.09109	0.09052	0.09075	0.09021	0.09052	0.09063	0.09035	0.09131
QT_{max}	0.198620	0.173135	0.173827	0.171486	0.182140	0.197194	0.182879	0.207349
$d\bar{\lambda}/d\alpha$	56.988	56.219	56.491	55.712	56.293	56.450	55.870	57.035
λ_p	6926.02	6919.29	6917.64	6902.68	6928.16	6930.65	6901.03	6898.52
$\langle\lambda\rangle$	6955.63	6948.49	6947.02	6931.71	6957.36	6959.93	6930.15	6928.27
λ_{max}	6410.00	6411.00	6410.00	6400.00	6430.00	6430.00	6400.00	6340.00

F718M	W1	W2	W3	W4	P5	P6	P7	P8
$\int QT d\lambda/\lambda$	0.008244	0.007166	0.007119	0.006835	0.007735	0.008413	0.007248	0.007936
$\bar{\lambda}$	7154.60	7153.64	7153.04	7150.20	7155.03	7155.34	7150.60	7152.01
$\delta\bar{\lambda}$	594.52	593.90	594.07	593.30	593.45	593.46	593.70	596.37
σ	0.03529	0.03526	0.03527	0.03524	0.03522	0.03522	0.03526	0.03541
QT_{max}	0.097398	0.085004	0.084818	0.082723	0.090766	0.098522	0.087637	0.096059
$d\bar{\lambda}/d\alpha$	8.909	8.892	8.897	8.878	8.877	8.876	8.890	8.968
λ_p	7163.53	7162.56	7161.96	7159.10	7163.93	7164.23	7159.51	7161.00
$\langle\lambda\rangle$	7168.00	7167.02	7166.43	7163.56	7168.38	7168.69	7163.98	7165.51
λ_{max}	6790.00	6790.00	6790.00	6790.00	6790.00	6790.00	6790.00	6790.00

F725LP	W1	W2	W3	W4	P5	P6	P7	P8
$\int QT d\lambda/\lambda$	0.030443	0.024684	0.025457	0.023559	0.027256	0.030108	0.025116	0.028181
$\bar{\lambda}$	8424.25	8378.15	8407.60	8395.87	8401.82	8412.20	8402.84	8395.24
$\delta\bar{\lambda}$	1950.65	1927.94	1942.52	1941.48	1960.64	1964.94	1959.63	1940.39
σ	0.09833	0.09772	0.09812	0.09820	0.09910	0.09919	0.09904	0.09815
QT_{max}	0.110217	0.095233	0.094331	0.089108	0.103396	0.112627	0.094788	0.105460
$d\bar{\lambda}/d\alpha$	81.454	80.006	80.937	80.963	82.510	82.770	82.415	80.878
λ_p	8506.86	8459.68	8489.80	8478.17	8485.81	8496.35	8486.69	8477.65
$\langle\lambda\rangle$	8548.63	8500.99	8531.39	8519.83	8528.35	8538.95	8529.14	8519.41
λ_{max}	7510.00	7510.00	7510.00	7510.00	7510.00	7510.00	7510.00	7580.00

F785LP	W1	W2	W3	W4	P5	P6	P7	P8
$\int QT d\lambda/\lambda$	0.021863	0.017199	0.018088	0.016584	0.019176	0.021329	0.017699	0.019887
$\bar{\lambda}$	8874.66	8845.22	8864.53	8860.66	8869.83	8876.38	8870.05	8852.73
$\delta\bar{\lambda}$	1549.25	1547.90	1545.75	1544.55	1572.26	1570.58	1566.77	1566.66
σ	0.07413	0.07431	0.07405	0.07403	0.07527	0.07514	0.07501	0.07515
QT_{max}	0.094059	0.077598	0.078833	0.072339	0.083563	0.091671	0.076849	0.090495
$d\bar{\lambda}/d\alpha$	48.772	48.850	48.608	48.554	50.259	50.115	49.908	49.999
λ_p	8923.78	8894.55	8913.53	8909.61	8920.52	8926.90	8920.39	8903.26
$\langle\lambda\rangle$	8948.50	8919.39	8938.18	8934.24	8946.04	8952.32	8945.72	8928.73
λ_{max}	8340.00	8230.00	8340.00	8340.00	8230.00	8340.00	8340.00	8340.00

F791W	W1	W2	W3	W4	P5	P6	P7	P8
$\int QTd\lambda/\lambda$	0.023267	0.019548	0.019720	0.018435	0.021209	0.023235	0.019566	0.022073
$\bar{\lambda}$	7880.78	7860.49	7872.84	7863.73	7862.70	7867.12	7862.43	7870.66
$\delta\bar{\lambda}$	1312.81	1296.56	1309.52	1308.89	1300.51	1304.66	1305.55	1295.70
σ	0.07074	0.07005	0.07064	0.07068	0.07024	0.07042	0.07051	0.06991
QT_{max}	0.116196	0.100849	0.099960	0.095290	0.109426	0.119119	0.101110	0.110614
$d\bar{\lambda}/d\alpha$	39.438	38.568	39.280	39.288	38.792	39.018	39.094	38.466
λ_p	7920.60	7899.50	7912.53	7903.46	7901.93	7906.57	7901.97	7909.51
$<\lambda>$	7940.64	7919.16	7932.52	7923.48	7921.70	7926.44	7921.89	7929.07
λ_{max}	7320.00	7320.00	7320.00	7310.00	7320.00	7320.00	7320.00	7330.00

F814W	W1	W2	W3	W4	P5	P6	P7	P8
$\int QTd\lambda/\lambda$	0.031137	0.025738	0.026255	0.024471	0.028074	0.030888	0.025939	0.029089
$\bar{\lambda}$	8086.40	8049.53	8072.87	8060.33	8058.69	8067.49	8058.26	8059.06
$\delta\bar{\lambda}$	1740.24	1714.35	1734.01	1733.79	1726.31	1733.09	1732.31	1712.93
σ	0.09139	0.09044	0.09121	0.09134	0.09097	0.09123	0.09129	0.09026
QT_{max}	0.122057	0.106038	0.105149	0.100513	0.114974	0.125134	0.106585	0.116242
$d\bar{\lambda}/d\alpha$	67.538	65.843	67.167	67.255	66.690	67.141	67.157	65.657
λ_p	8154.74	8116.40	8140.92	8128.54	8126.39	8135.60	8126.40	8125.66
$<\lambda>$	8189.24	8150.21	8175.29	8163.00	8160.63	8170.02	8160.84	8159.31
λ_{max}	7270.00	7270.00	7260.00	7260.00	7270.00	7270.00	7260.00	7270.00

F850LP	W1	W2	W3	W4	P5	P6	P7	P8
$\int QTd\lambda/\lambda$	0.013966	0.010650	0.011451	0.010468	0.012101	0.013562	0.011194	0.012309
$\bar{\lambda}$	9266.84	9256.64	9261.41	9259.14	9276.09	9277.39	9273.01	9268.67
$\delta\bar{\lambda}$	1150.81	1154.01	1149.10	1147.52	1172.16	1169.20	1168.67	1177.40
σ	0.05274	0.05294	0.05269	0.05263	0.05366	0.05352	0.05352	0.05394
QT_{max}	0.088899	0.067433	0.073176	0.067228	0.075214	0.084934	0.070229	0.075677
$d\bar{\lambda}/d\alpha$	25.772	25.945	25.711	25.647	26.711	26.573	26.561	26.972
λ_p	9292.78	9282.76	9287.29	9284.96	9302.98	9304.14	9299.74	9295.82
$<\lambda>$	9305.81	9295.88	9300.29	9297.93	9316.48	9317.57	9313.17	9309.46
λ_{max}	9200.00	9060.00	9060.00	9040.00	9060.00	9040.00	9040.00	9060.00

F875M	W1	W2	W3	W4	P5	P6	P7	P8
$\int QTd\lambda/\lambda$	0.006612	0.005185	0.005486	0.005035	0.005698	0.006350	0.005295	0.005937
$\bar{\lambda}$	8755.66	8749.57	8754.41	8754.59	8752.68	8754.67	8753.42	8746.07
$\delta\bar{\lambda}$	554.16	554.34	554.06	553.91	554.39	554.69	553.99	553.97
σ	0.02688	0.02690	0.02688	0.02687	0.02690	0.02691	0.02688	0.02690
QT_{max}	0.085194	0.066755	0.070658	0.064843	0.073282	0.081542	0.068165	0.076576
$d\bar{\lambda}/d\alpha$	6.325	6.333	6.324	6.320	6.333	6.338	6.323	6.328
λ_p	8761.99	8755.91	8760.75	8760.93	8759.03	8761.01	8759.76	8752.41
$<\lambda>$	8765.16	8759.09	8763.92	8764.10	8762.20	8764.19	8762.93	8755.59
λ_{max}	8750.00	8740.00	8740.00	8750.00	8740.00	8750.00	8740.00	8720.00

F889N	W1	W2	W3	W4	P5	P6	P7	P8
$\int QT d\lambda/\lambda$	0.000441	0.000338	0.000365	0.000336	0.000378	0.000423	0.000352	0.000381
$\bar{\lambda}$	8888.01	8887.95	8888.00	8888.01	8887.99	8888.02	8888.00	8887.90
$\delta\bar{\lambda}$	51.05	51.11	51.07	51.05	51.05	51.05	51.05	51.15
σ	0.00244	0.00244	0.00244	0.00244	0.00244	0.00244	0.00244	0.00244
QT_{max}	0.079760	0.061052	0.065893	0.060646	0.068243	0.076391	0.063585	0.068796
$d\bar{\lambda}/d\alpha$	0.053	0.053	0.053	0.053	0.053	0.053	0.053	0.053
λ_p	8888.06	8888.00	8888.05	8888.06	8888.04	8888.07	8888.05	8887.95
$<\lambda>$	8888.09	8888.03	8888.08	8888.08	8888.07	8888.09	8888.08	8887.98
λ_{max}	8885.00	8885.00	8885.00	8885.00	8885.00	8885.00	8885.00	8885.00

F1042M	W1	W2	W3	W4	P5	P6	P7	P8
$\int QT d\lambda/\lambda$	0.000867	0.000645	0.000698	0.000631	0.000813	0.000910	0.000741	0.000818
$\bar{\lambda}$	10161.00	10160.50	10160.40	10160.10	10170.30	10170.00	10169.50	10170.10
$\delta\bar{\lambda}$	470.18	469.88	470.08	469.84	482.93	482.54	481.75	482.42
σ	0.01965	0.01964	0.01965	0.01964	0.02016	0.02015	0.02012	0.02014
QT_{max}	0.025922	0.019319	0.020885	0.018931	0.023620	0.026446	0.021579	0.023770
$d\bar{\lambda}/d\alpha$	3.924	3.919	3.922	3.918	4.135	4.129	4.116	4.127
λ_p	10164.90	10164.50	10164.40	10164.10	10174.50	10174.20	10173.70	10174.30
$<\lambda>$	10166.90	10166.50	10166.40	10166.10	10176.60	10176.30	10175.70	10176.40
λ_{max}	10040.00	10040.00	10040.00	10040.00	10040.00	10040.00	10040.00	10040.00

F1083N	W1	W2	W3	W4	P5	P6	P7	P8
$\int QT d\lambda/\lambda$	0.000005	0.000004	0.000004	0.000003	0.000005	0.000006	0.000005	0.000005
$\bar{\lambda}$	10830.20	10830.10	10830.20	10830.20	10830.70	10830.50	10830.40	10830.70
$\delta\bar{\lambda}$	81.89	81.75	81.89	81.88	81.88	81.86	81.86	81.88
σ	0.00321	0.00321	0.00321	0.00321	0.00321	0.00321	0.00321	0.00321
QT_{max}	0.000523	0.000390	0.000421	0.000378	0.000586	0.000655	0.000526	0.000586
$d\bar{\lambda}/d\alpha$	0.112	0.111	0.112	0.112	0.112	0.112	0.112	0.112
λ_p	10830.30	10830.20	10830.30	10830.30	10830.80	10830.60	10830.50	10830.80
$<\lambda>$	10830.40	10830.20	10830.30	10830.40	10830.80	10830.70	10830.60	10830.80
λ_{max}	10810.00	10810.00	10810.00	10810.00	10810.00	10810.00	10810.00	10810.00

A.2 Filter Passbands

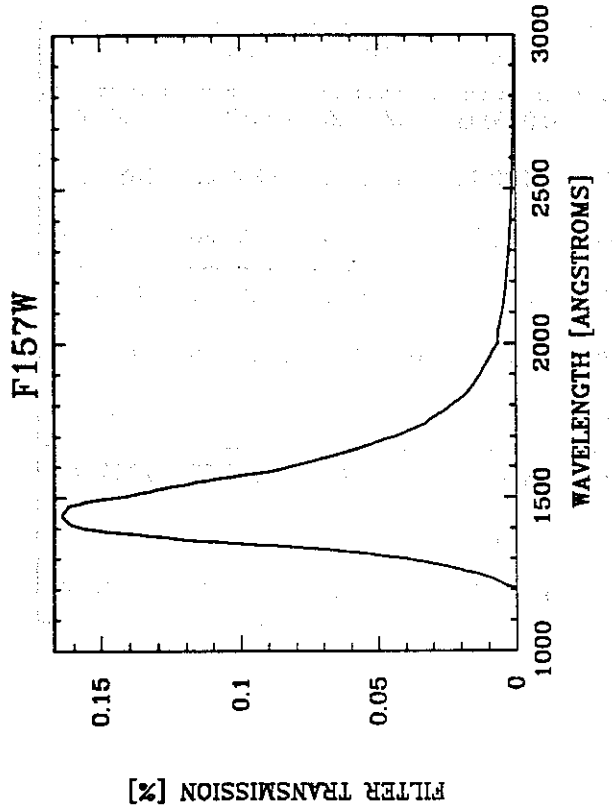

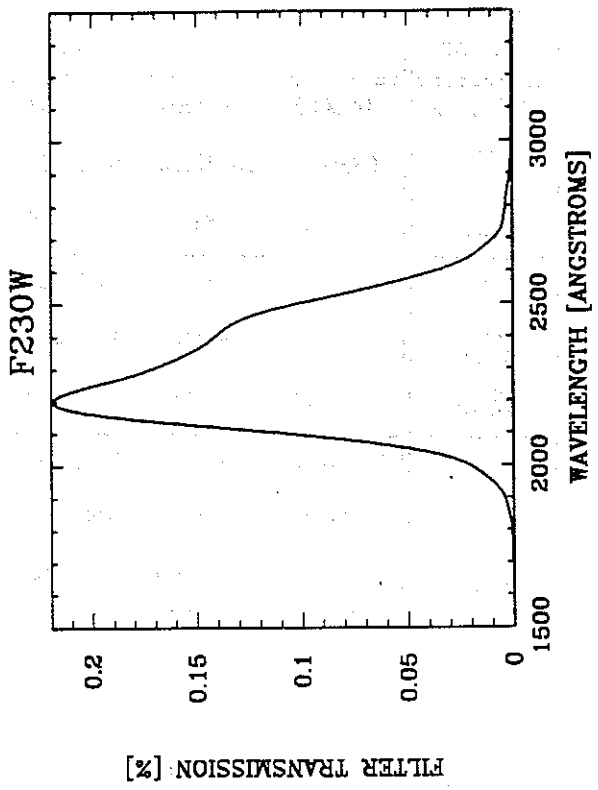

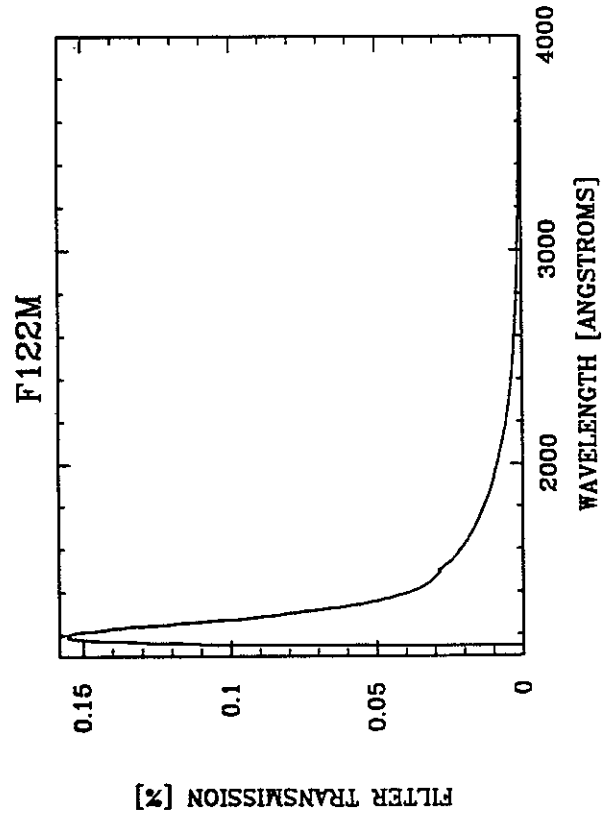

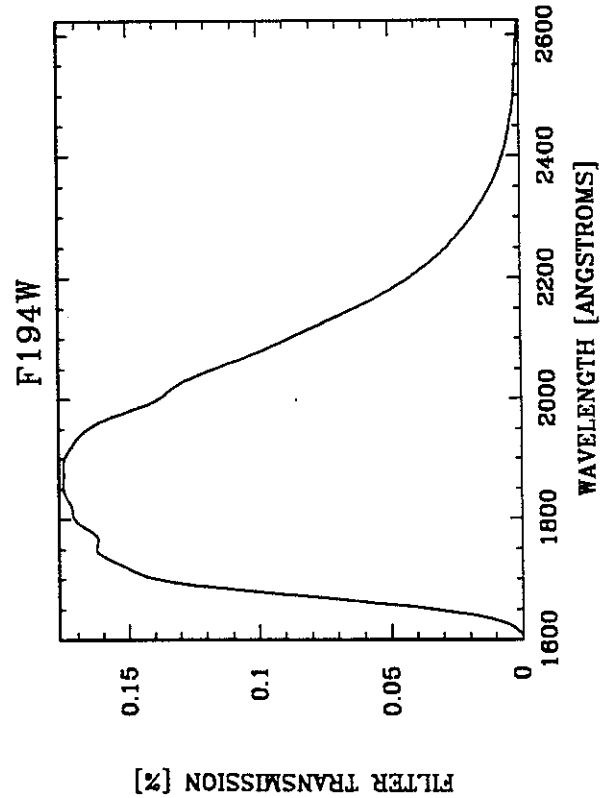

A.2 Filter Passbands (continued)

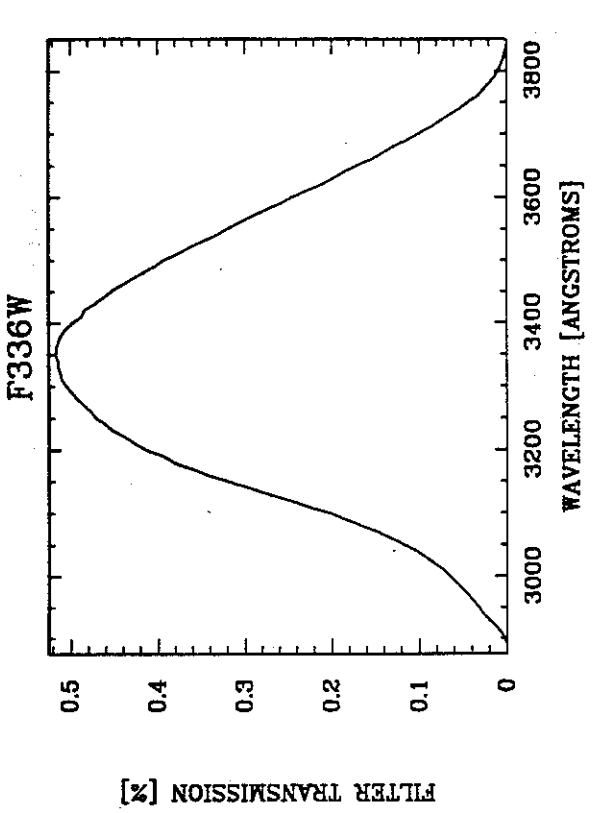

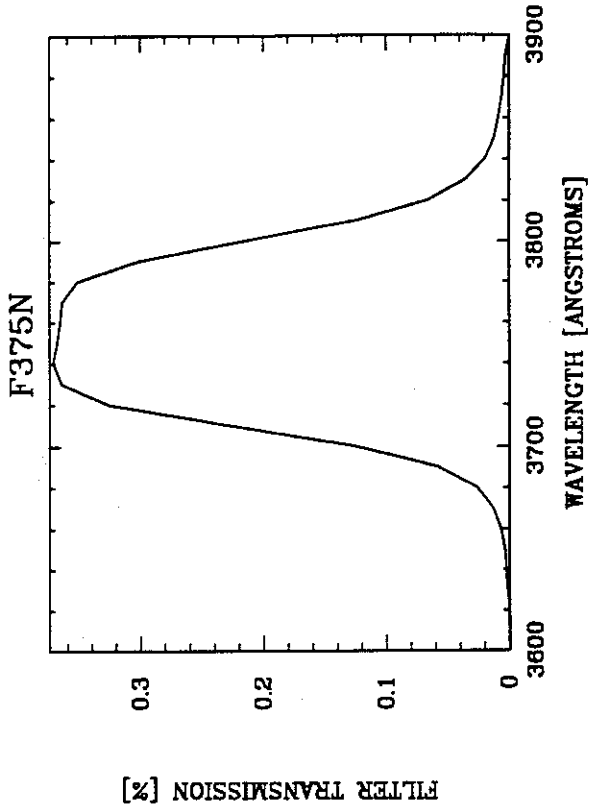

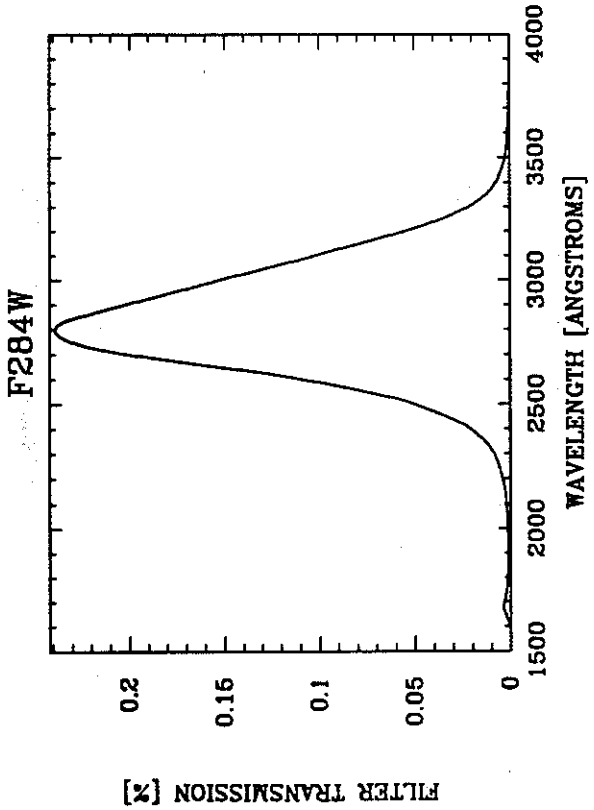

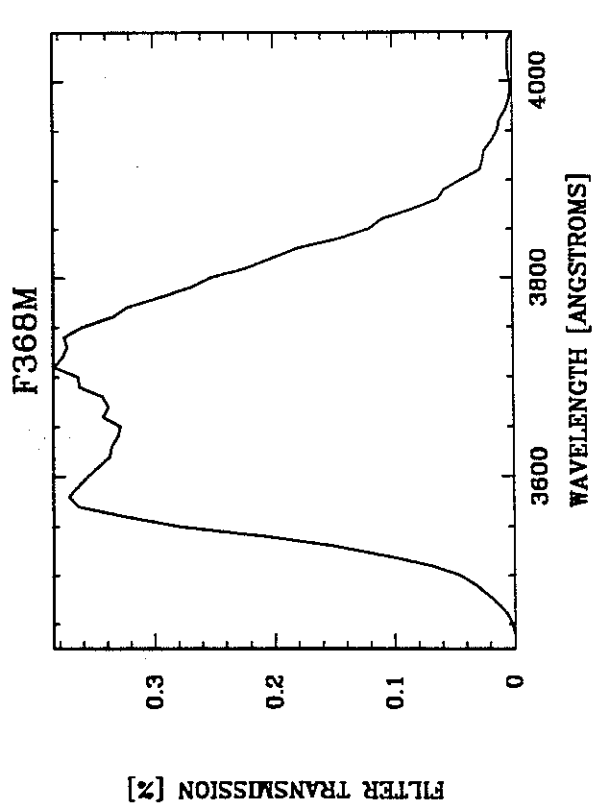

A.2 Filter Passbands (continued)

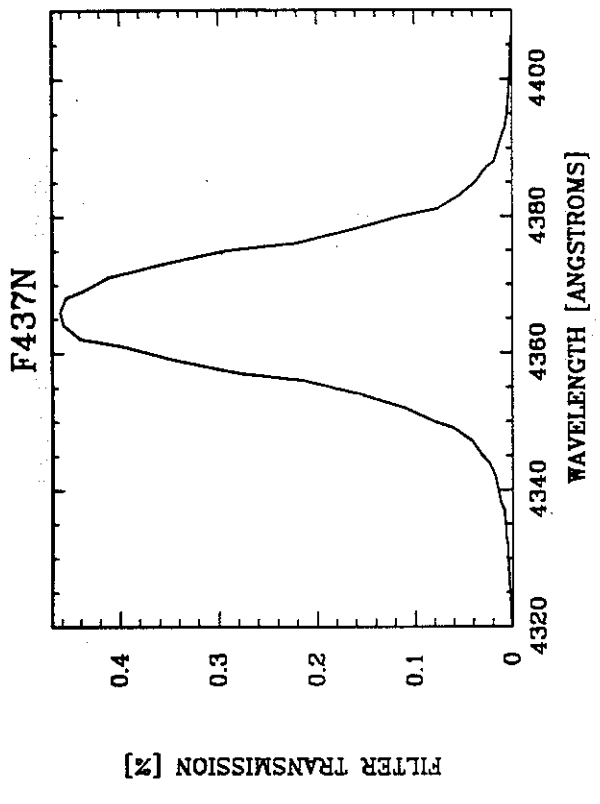

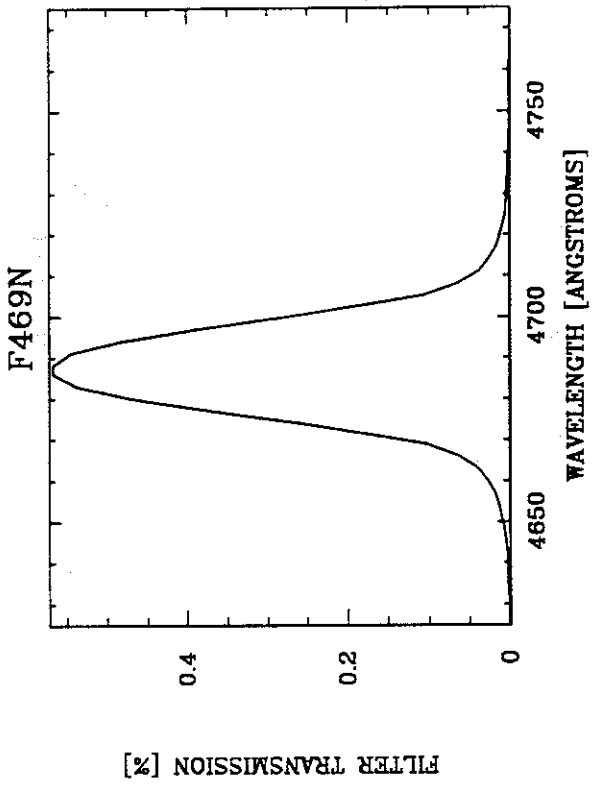

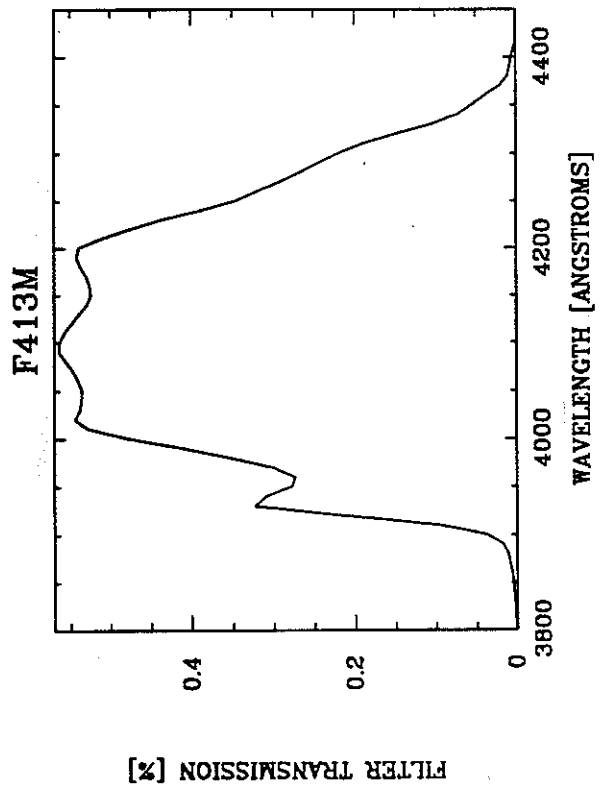

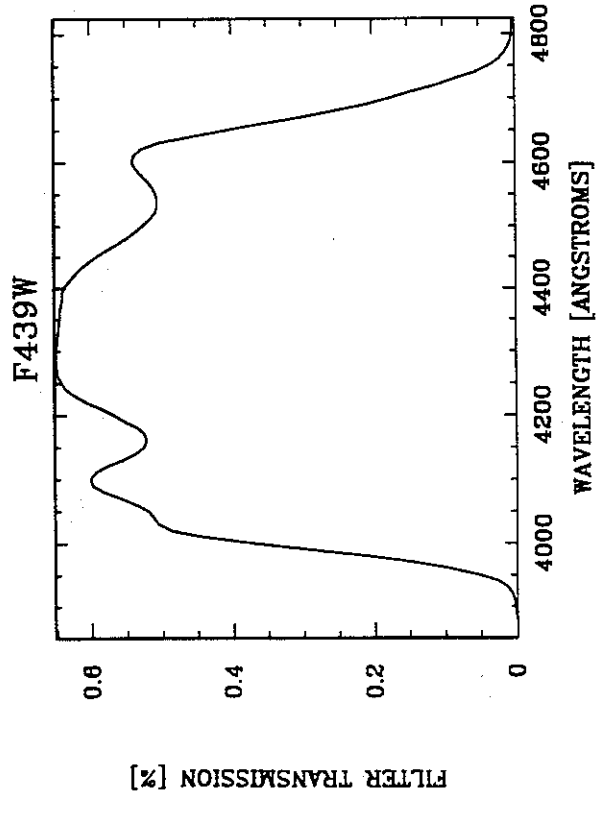

A.2 Filter Passbands (continued)

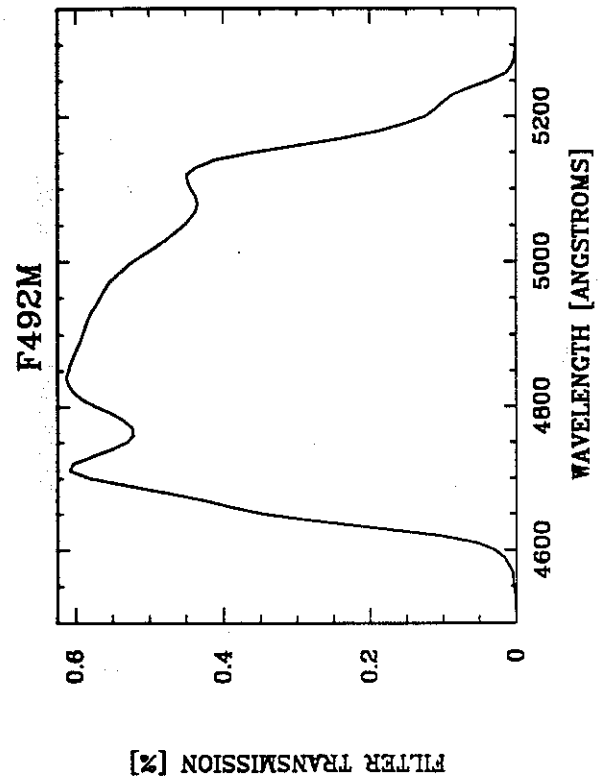

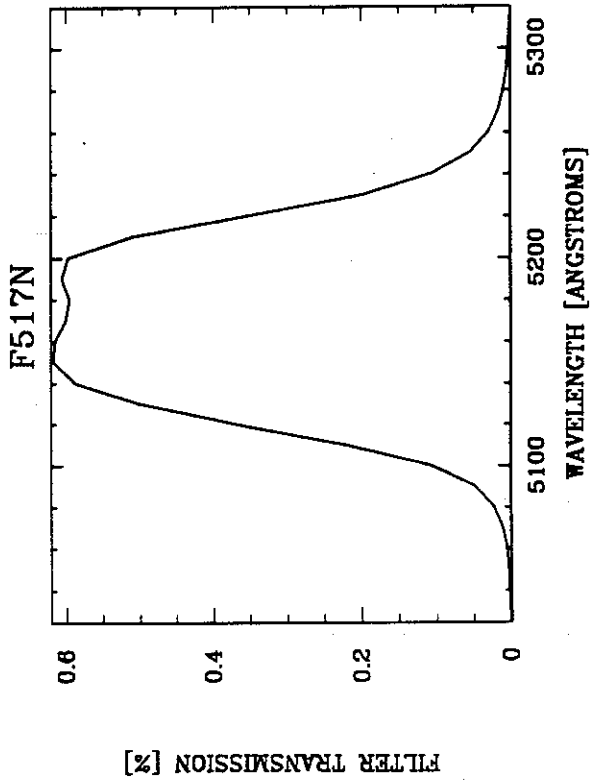

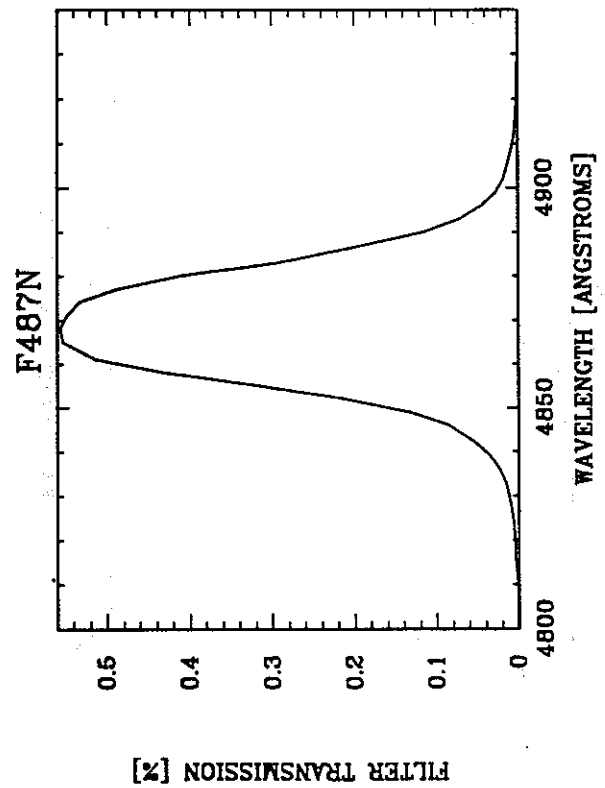

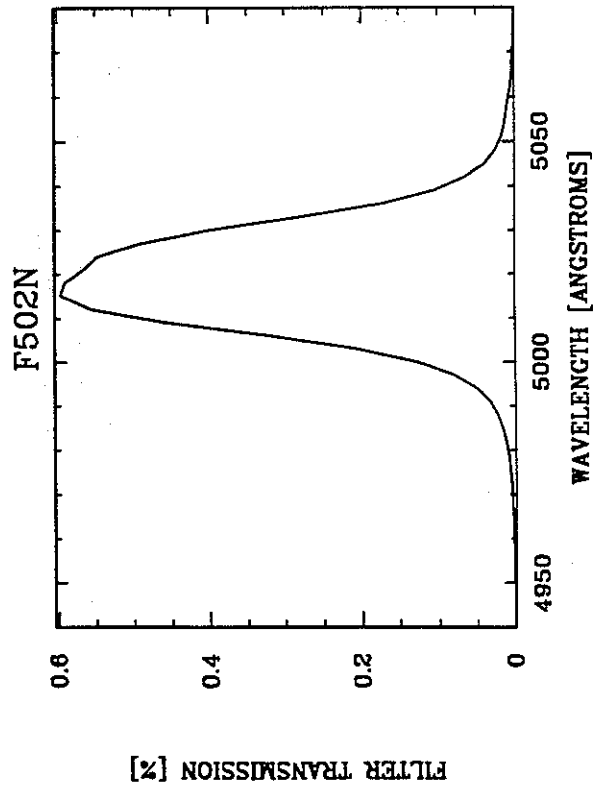

A.2 Filter Passbands (continued)

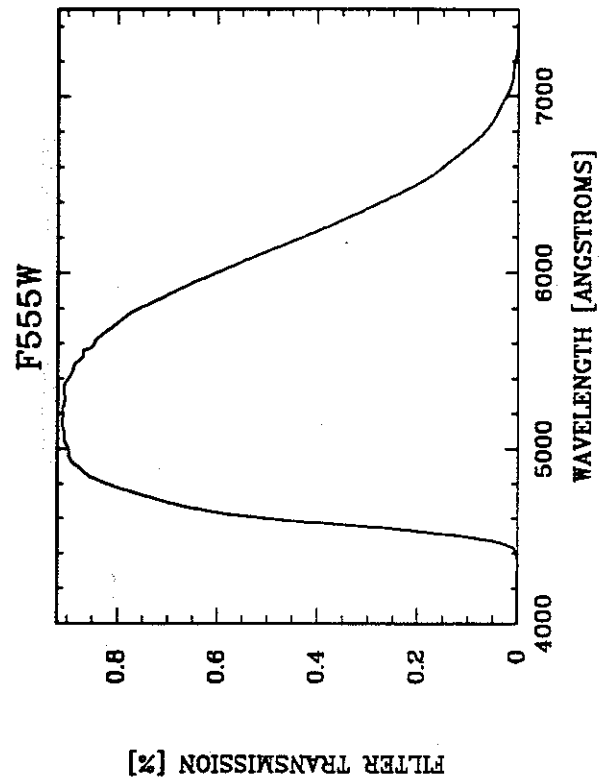

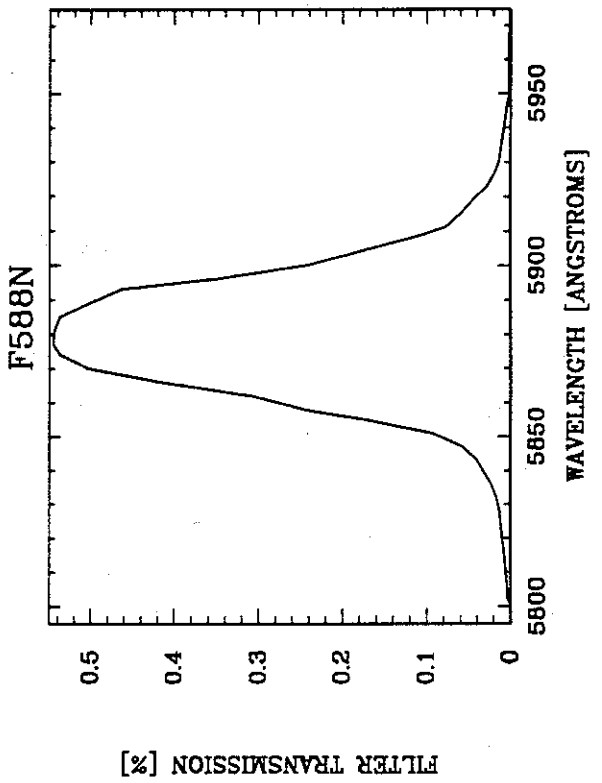

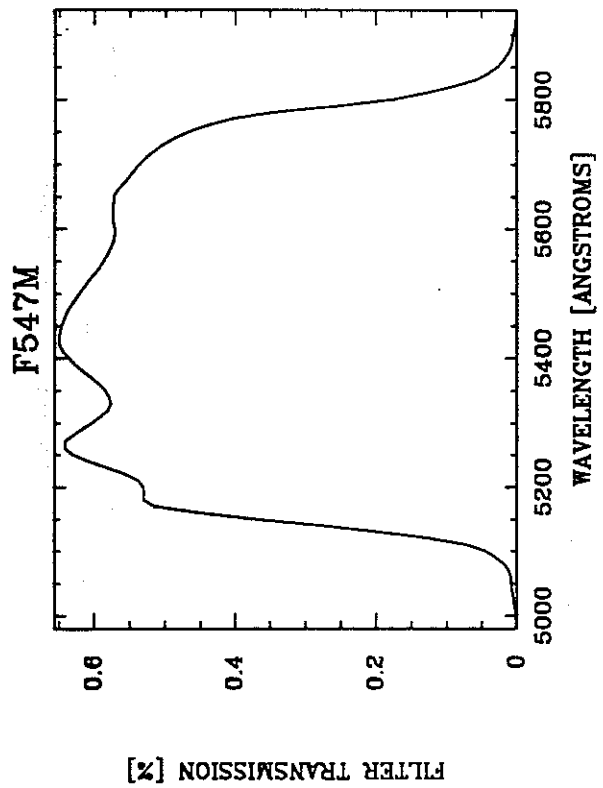

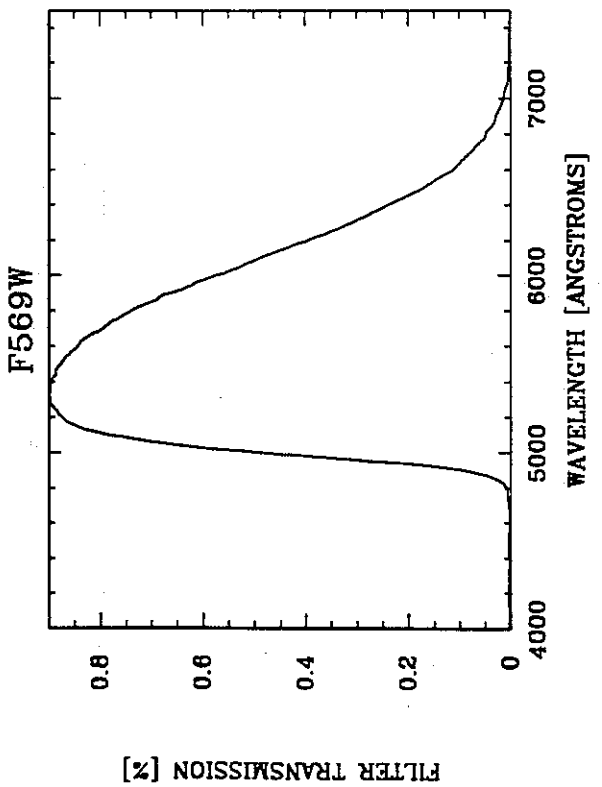

A.2 Filter Passbands (continued)

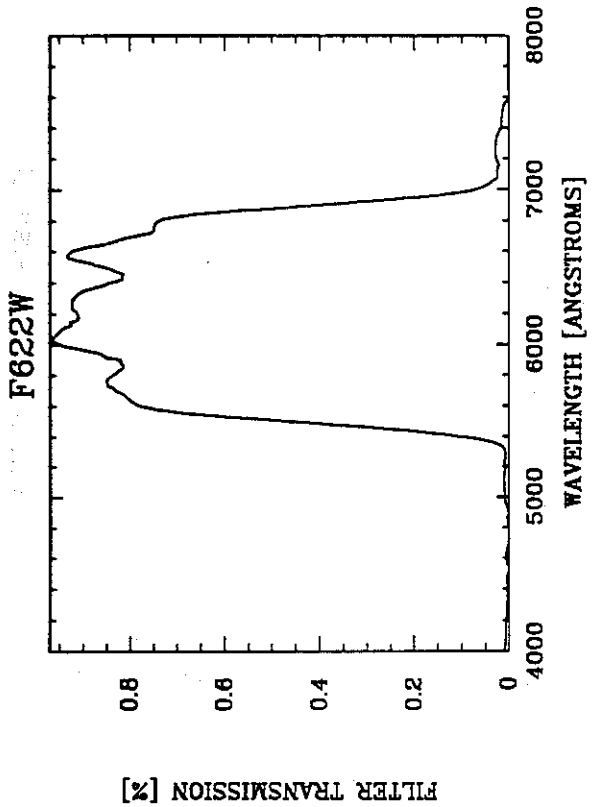

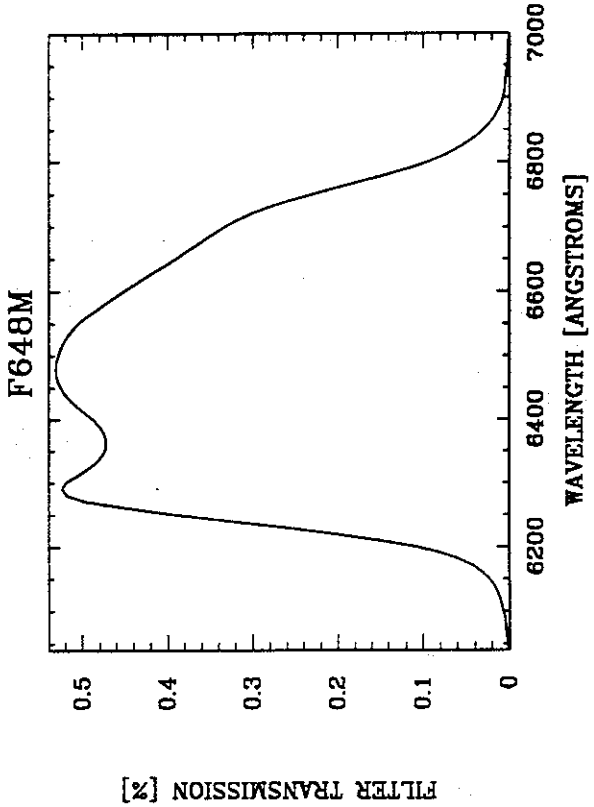

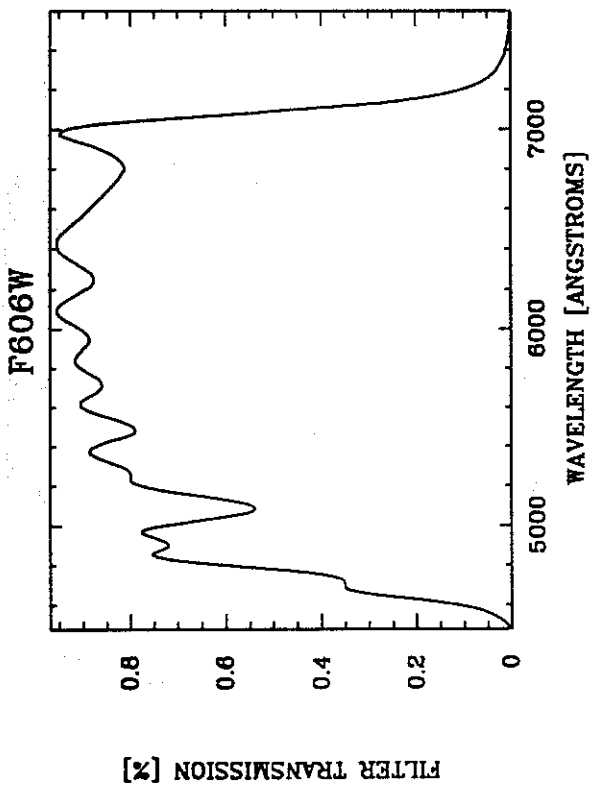

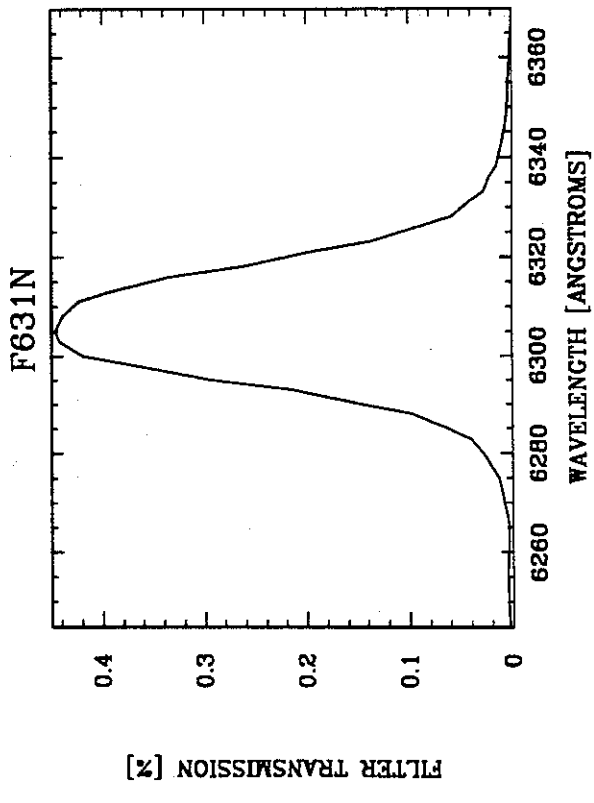

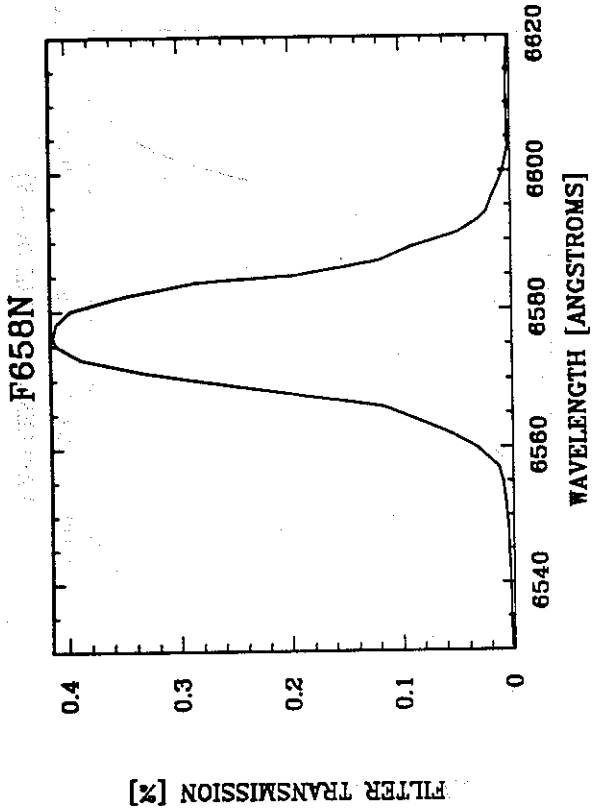
F658N
FILTER TRANSMISSION [%]
0
0.1
0.2
0.3
0.4
6540
6560
6580
6600
6620
WAVELENGTH [ANGSTROMS]

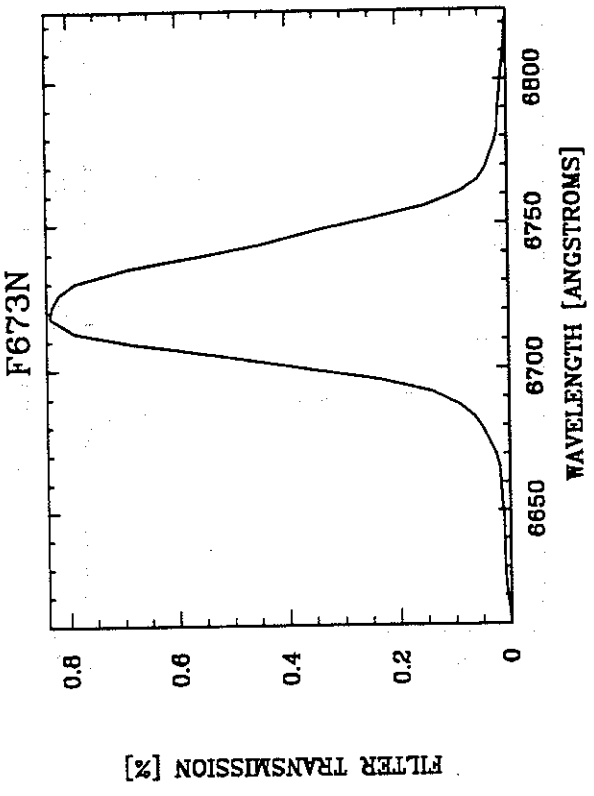
F673N
FILTER TRANSMISSION [%]
0
0.2
0.4
0.6
0.8
6650
6700
6750
6800
WAVELENGTH [ANGSTROMS]

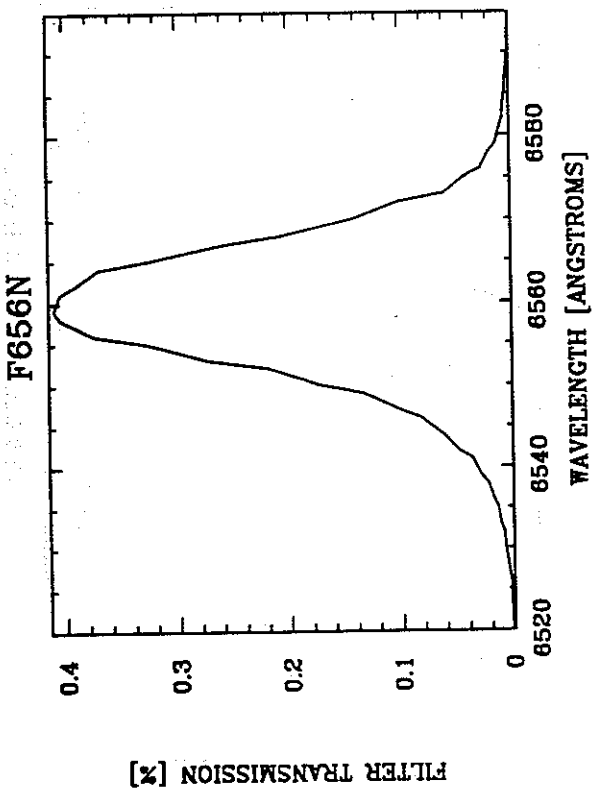
F656N
FILTER TRANSMISSION [%]
0
0.1
0.2
0.3
0.4
6520
6540
6560
6580
WAVELENGTH [ANGSTROMS]

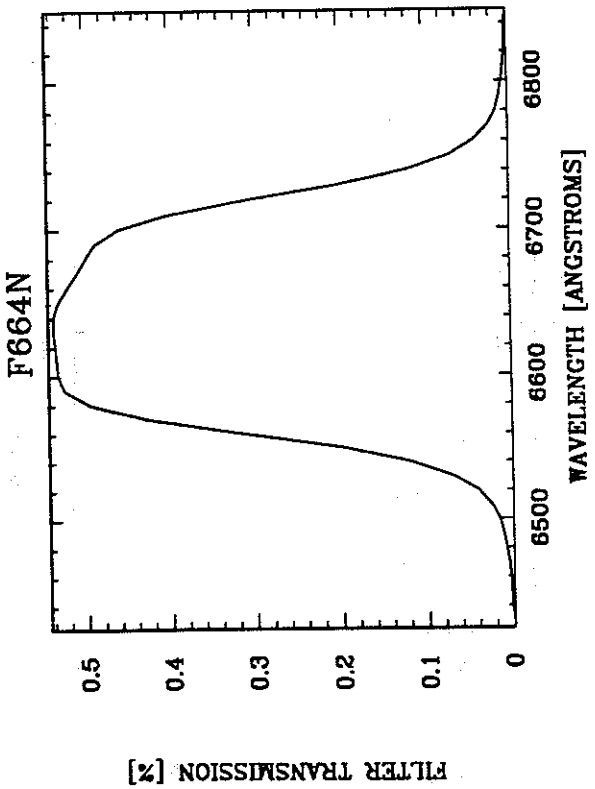
F664N
FILTER TRANSMISSION [%]
0
0.1
0.2
0.3
0.4
0.5
6500
6600
6700
6800
WAVELENGTH [ANGSTROMS]

A.2 Filter Passbands (continued)

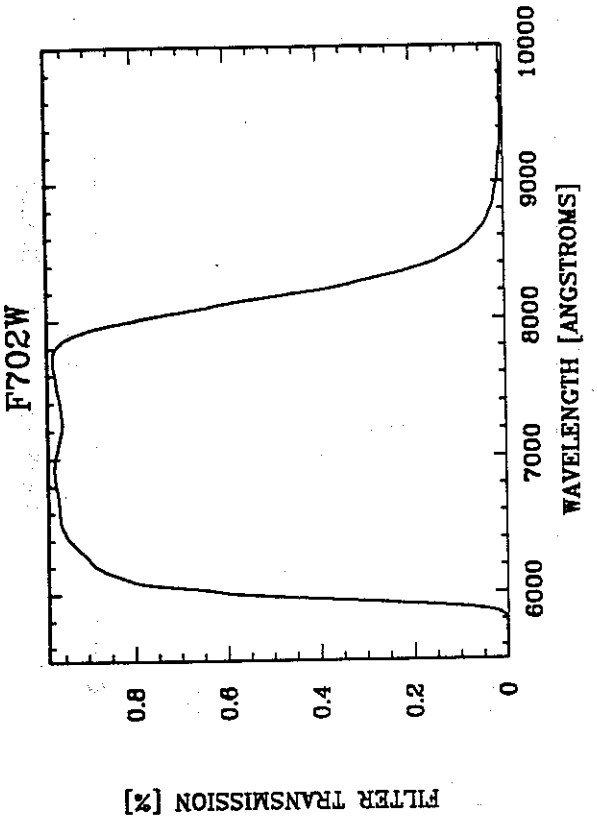

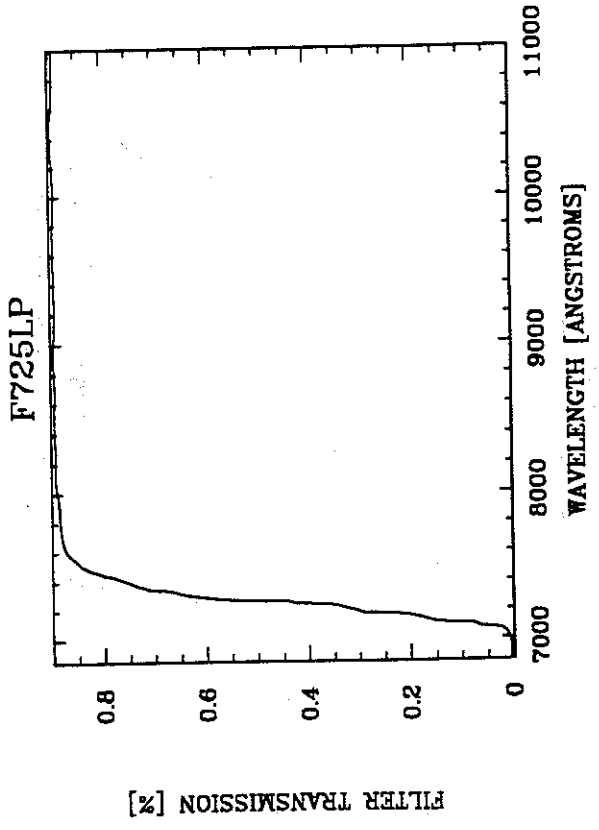

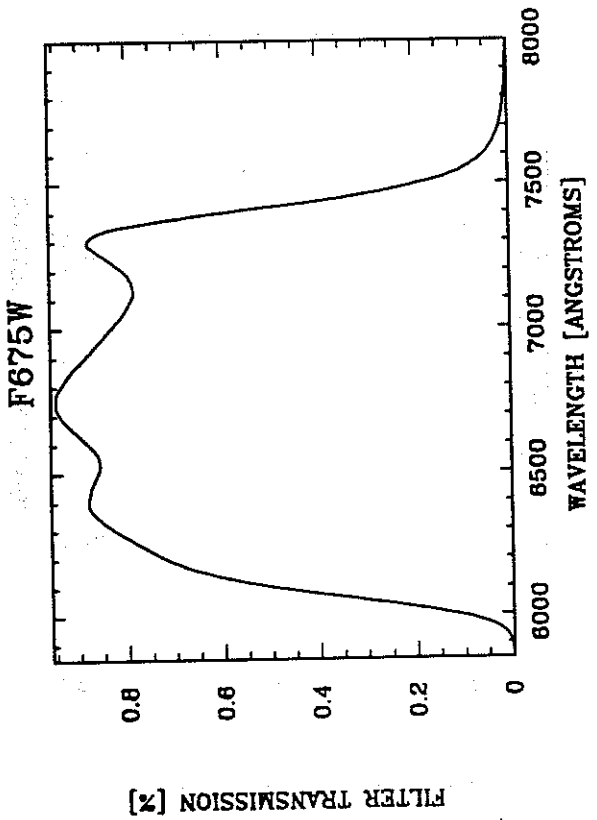

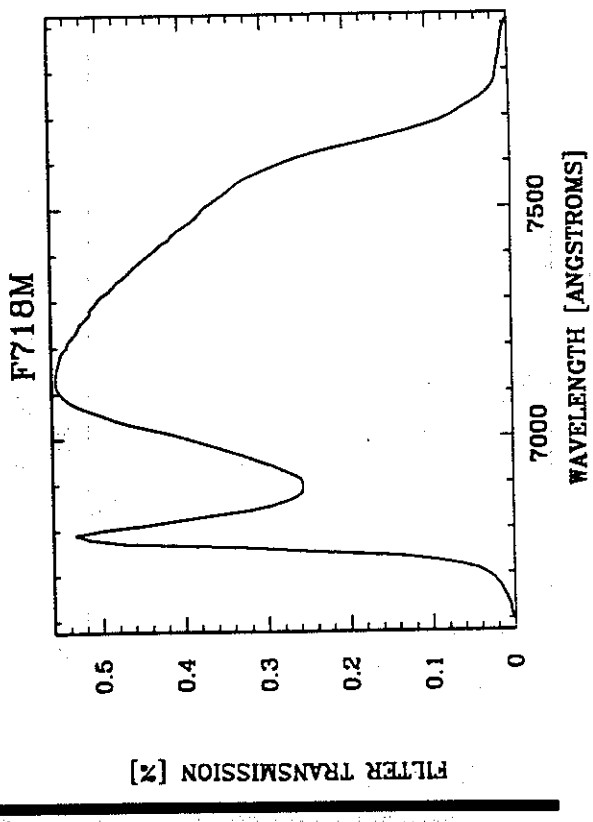

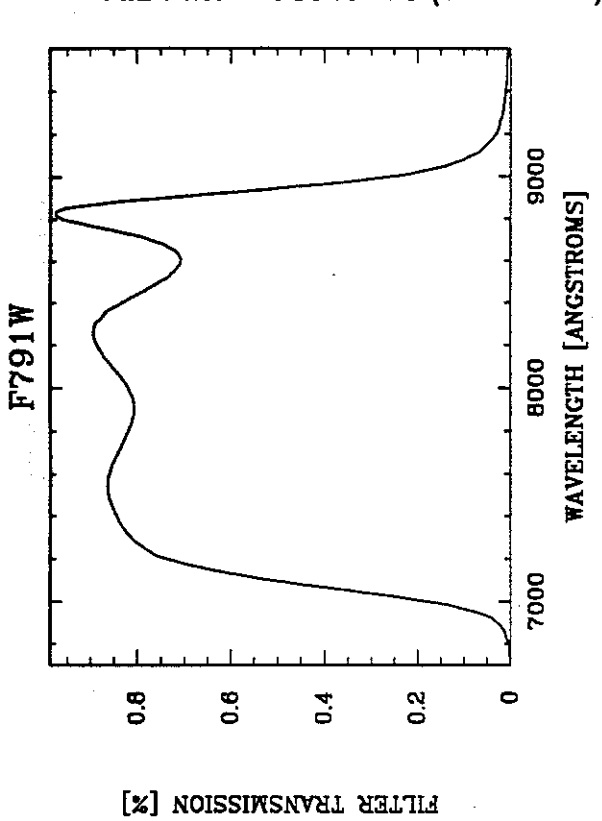
F791W
FILTER TRANSMISSION [%]
0
0.2
0.4
0.6
0.8
7000
8000
9000
WAVELENGTH [ANGSTROMS]

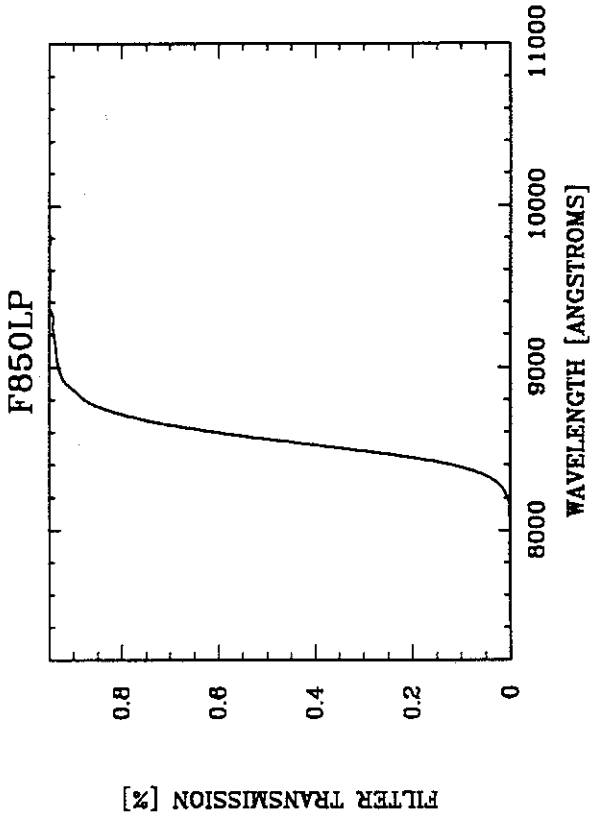
F850LP
FILTER TRANSMISSION [%]
0
0.2
0.4
0.6
0.8
8000
9000
10000
11000
WAVELENGTH [ANGSTROMS]

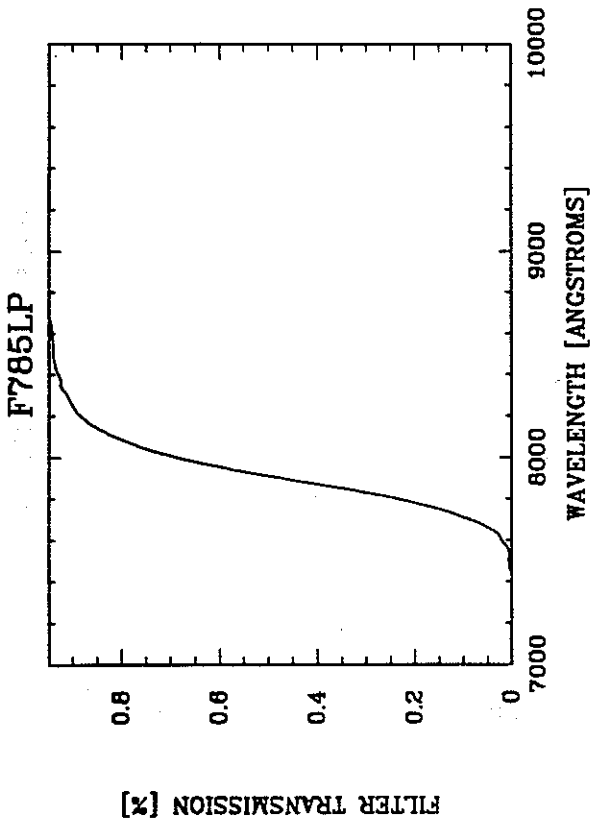
F785LP
FILTER TRANSMISSION [%]
0
0.2
0.4
0.6
0.8
7000
8000
9000
10000
WAVELENGTH [ANGSTROMS]

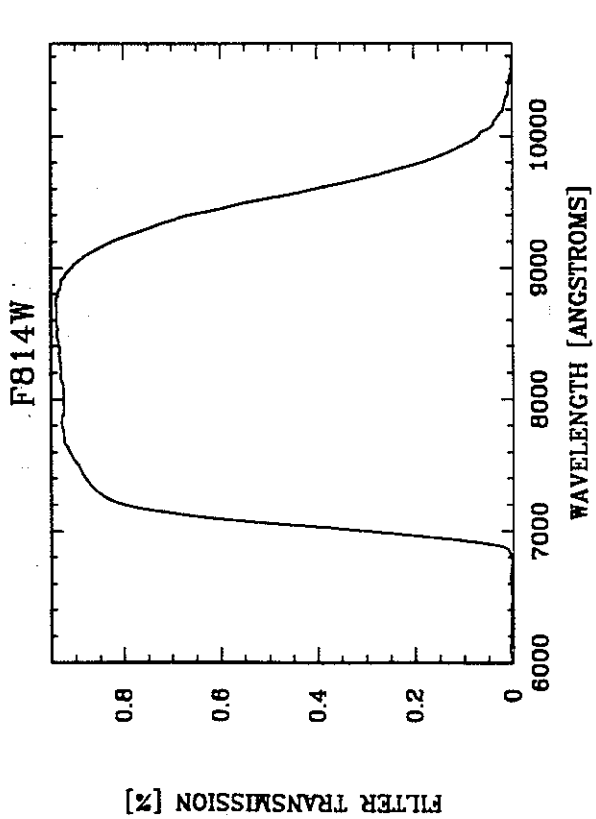
F814W
FILTER TRANSMISSION [%]
0
0.2
0.4
0.6
0.8
6000
7000
8000
9000
10000
WAVELENGTH [ANGSTROMS]

A.2 Filter Passbands (continued)

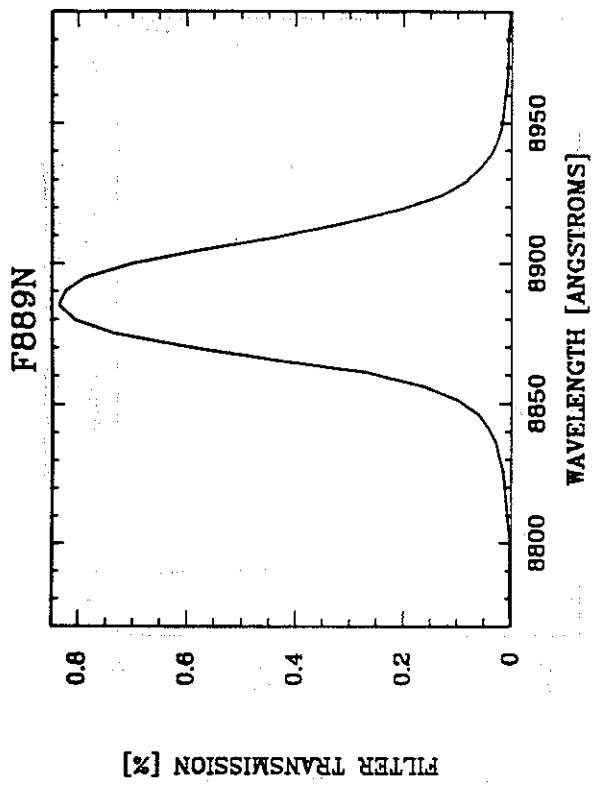

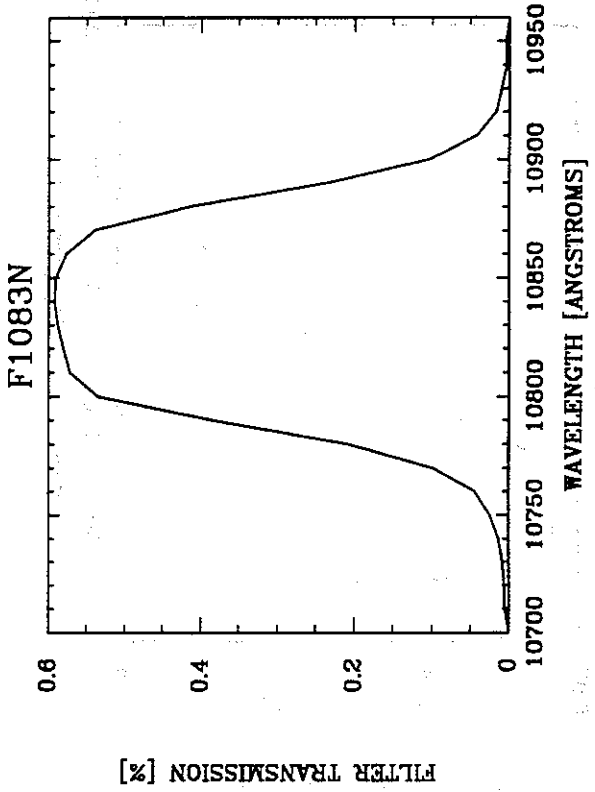

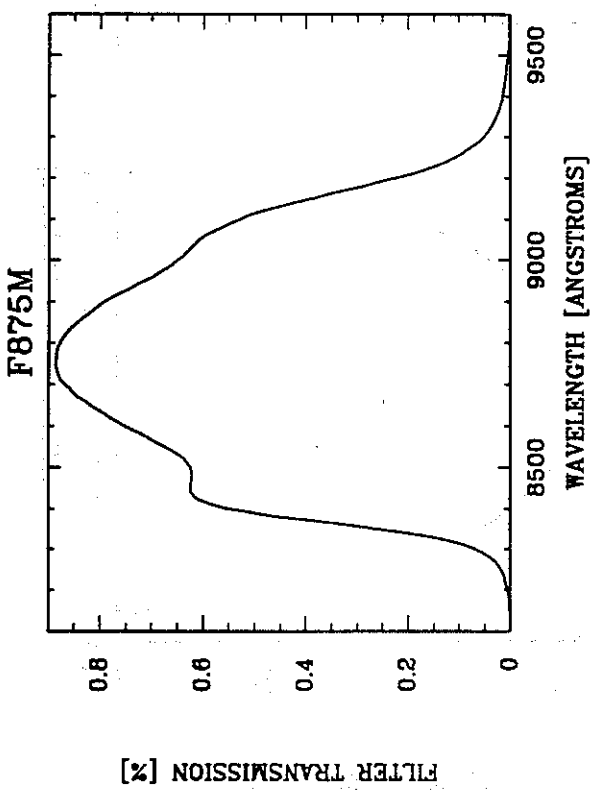

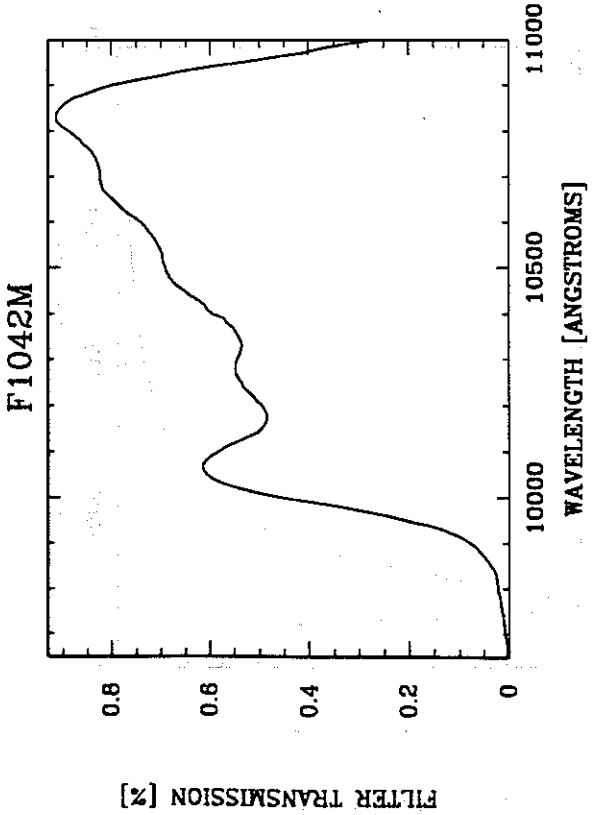

A.2 Filter Passbands (continued)

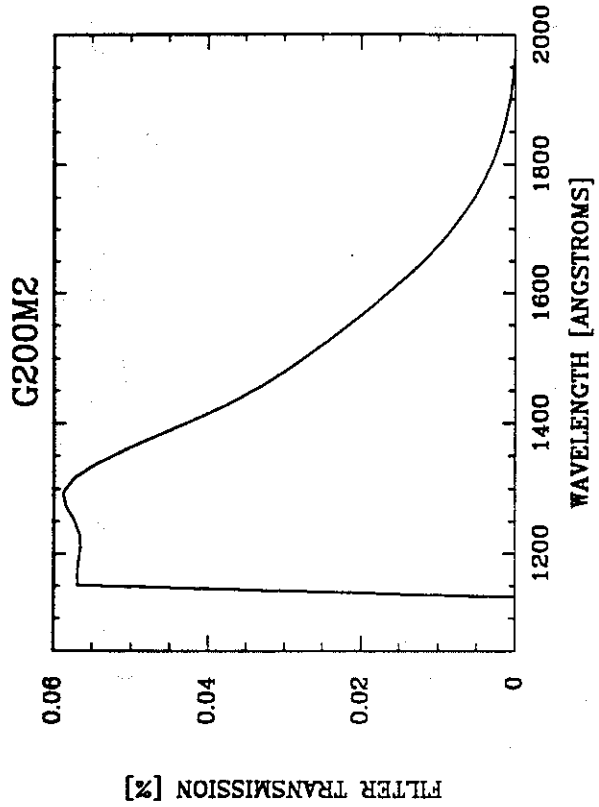

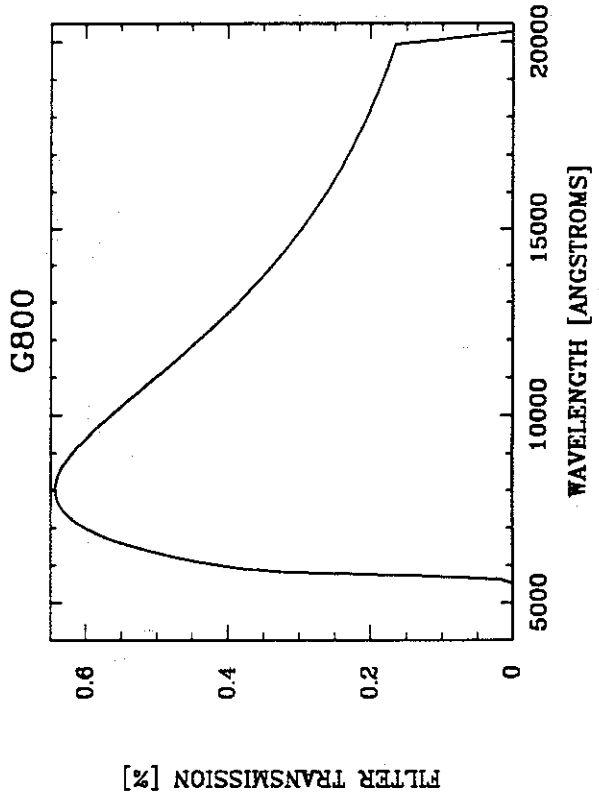

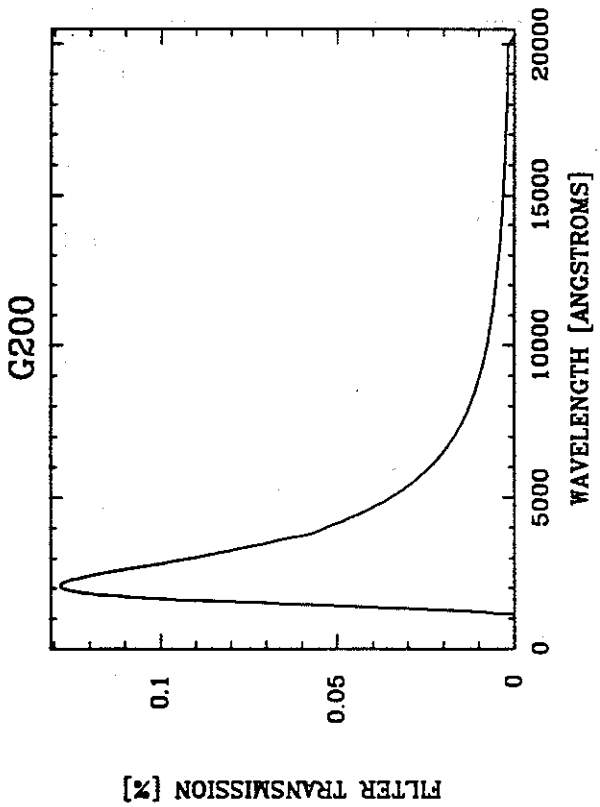

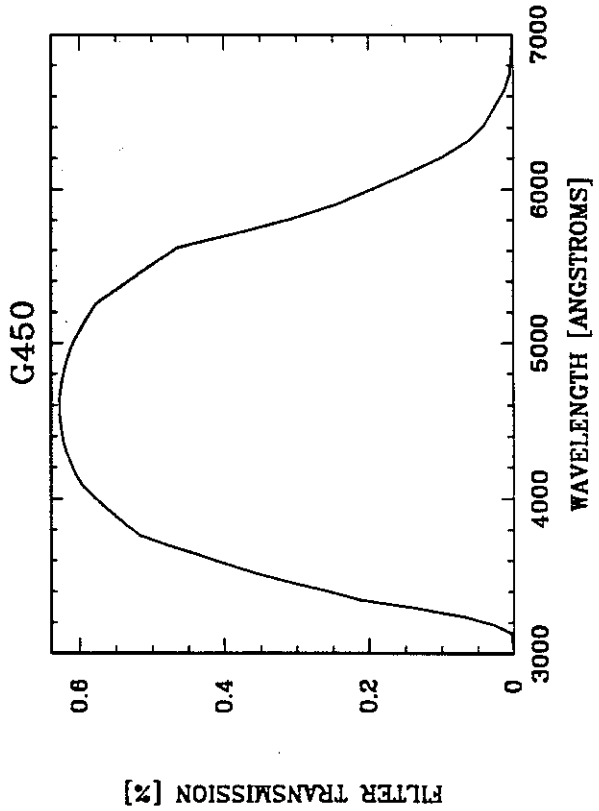

A.3 Filter Passbands including WF/PC + OTA Response

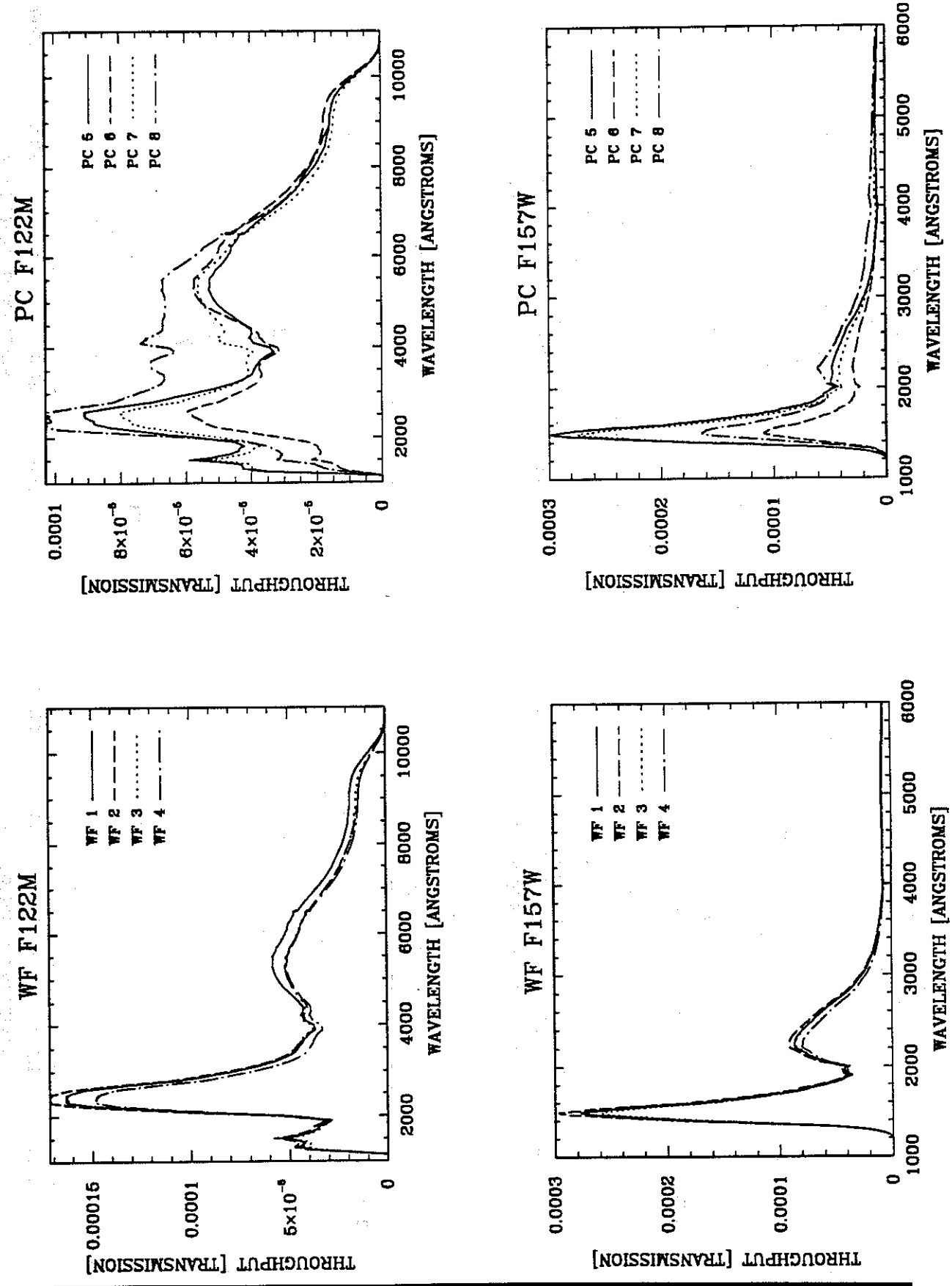

A.3 Filter Passbands including WF/PC + OTA Response (continued)

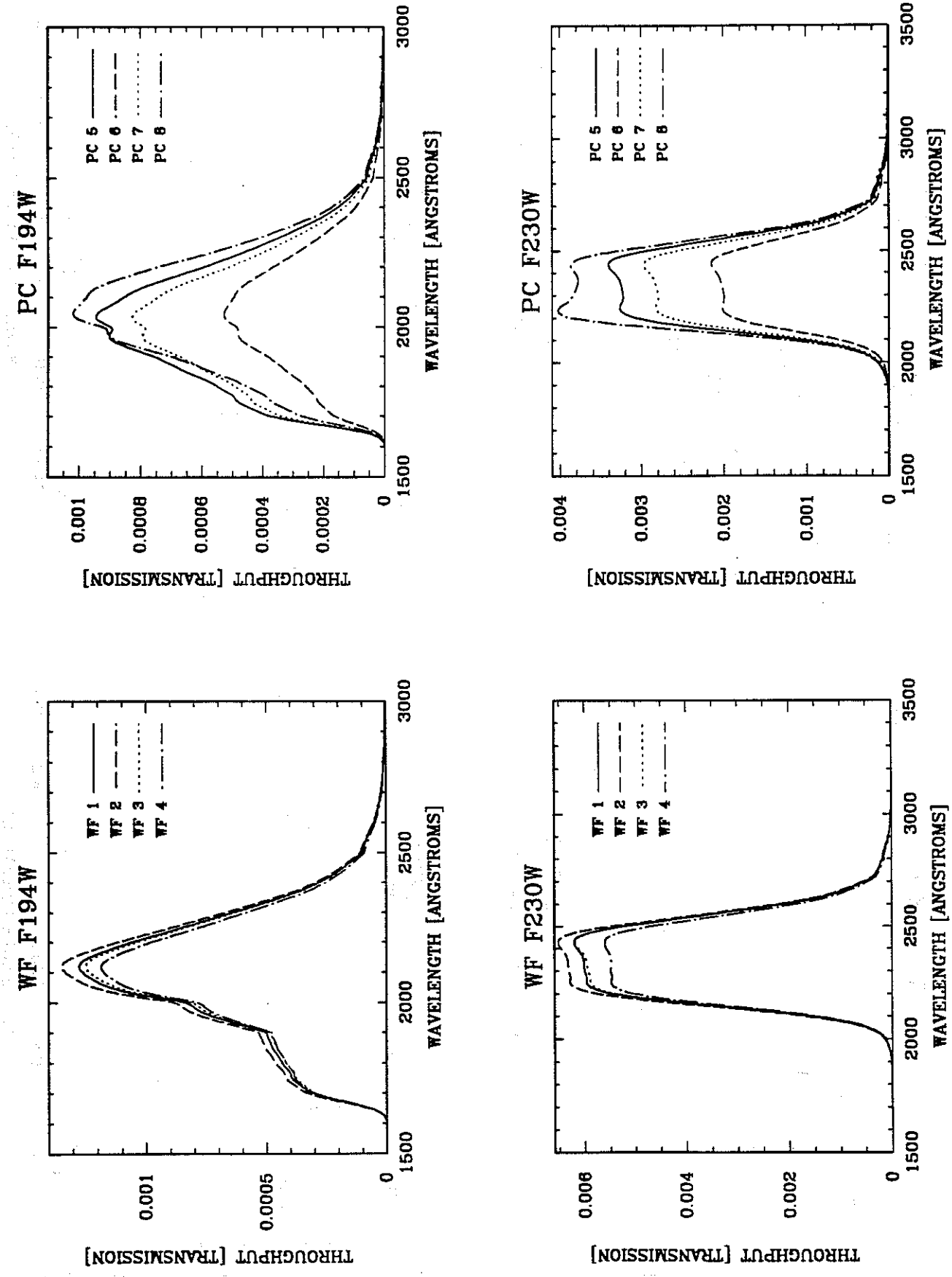

A.3 Filter Passbands including WF/PC + OTA Response (continued)

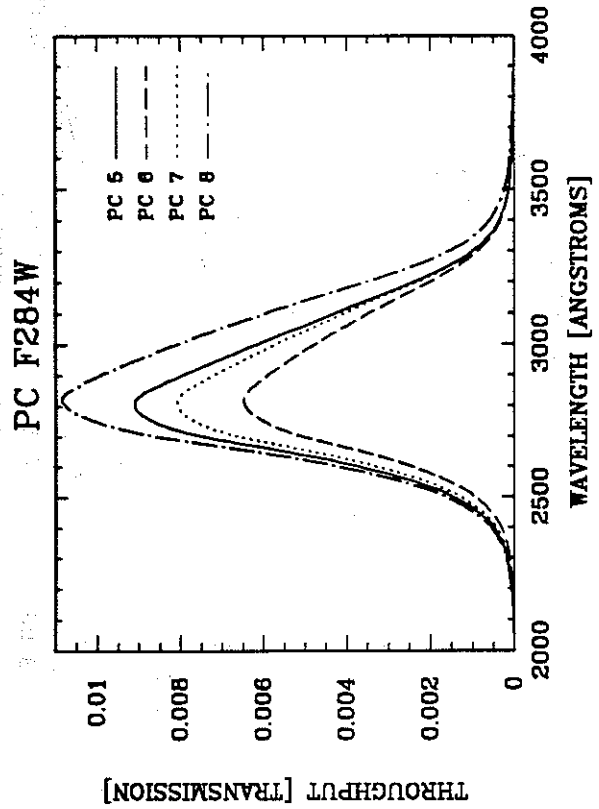

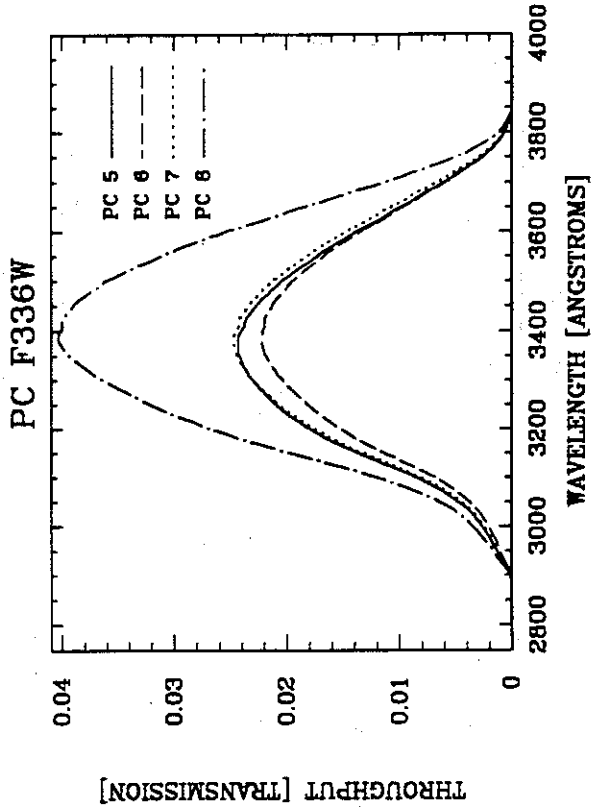

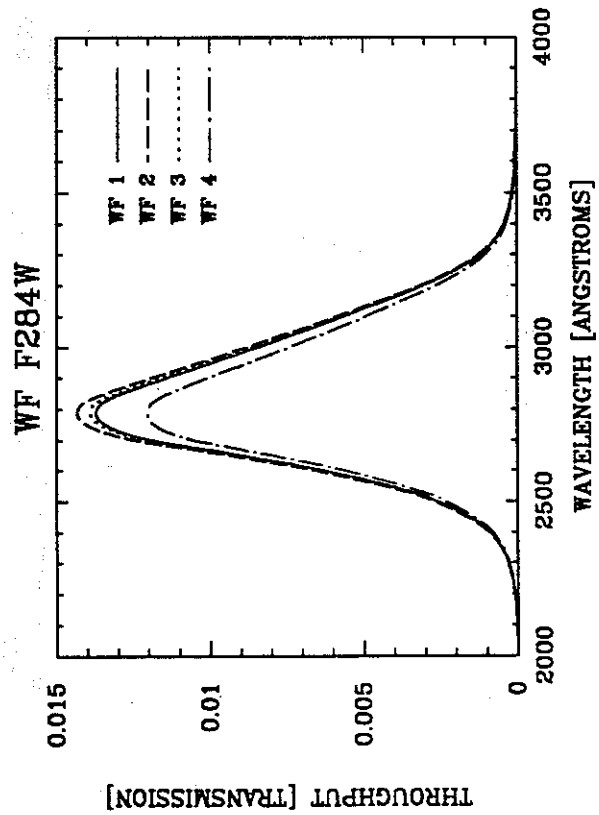

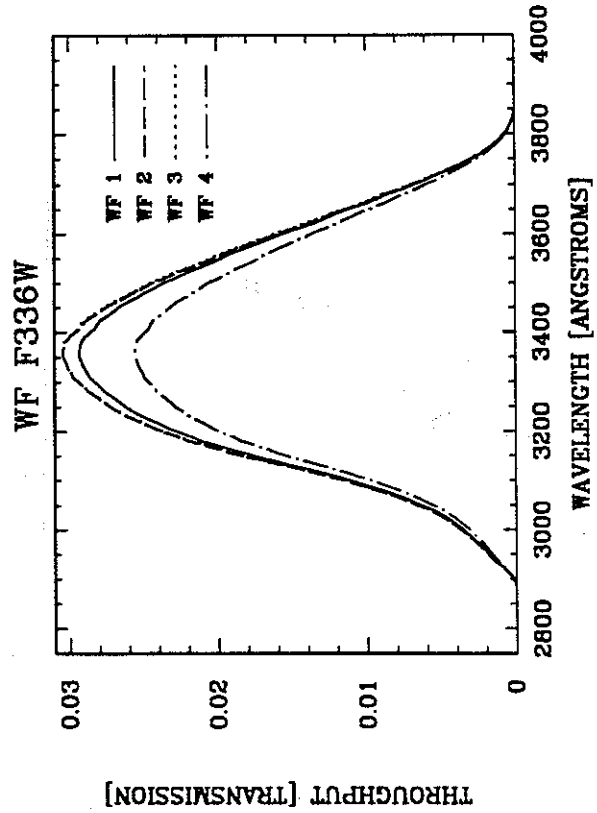

A.3 Filter Passbands including WF/PC + OTA Response (continued)

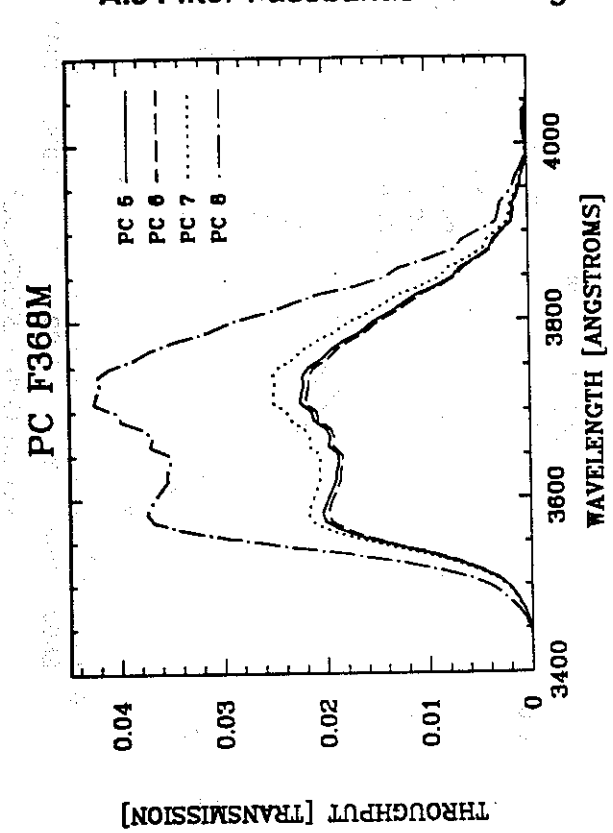

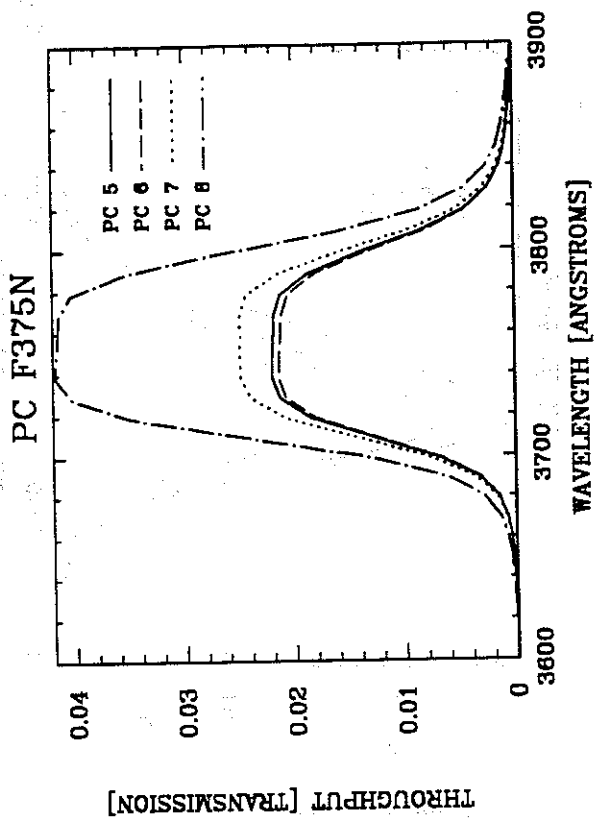

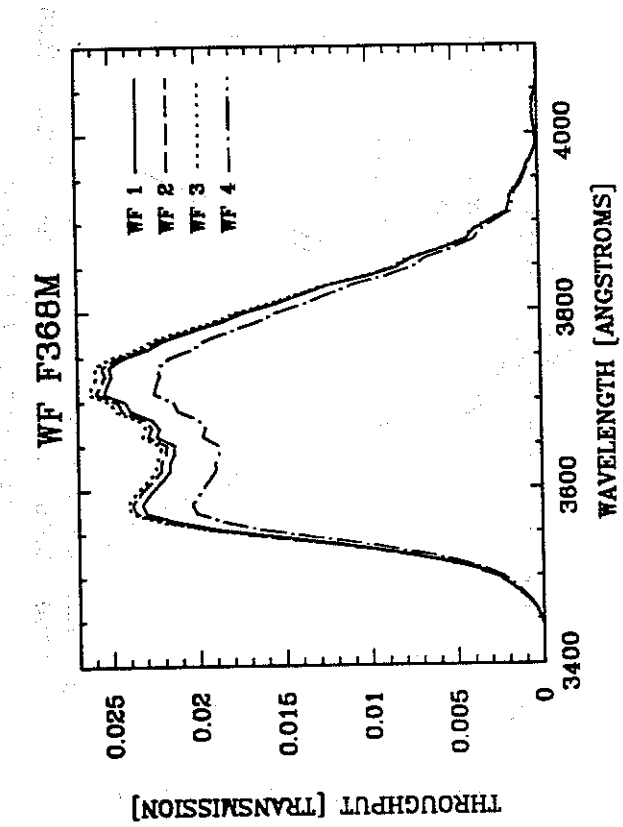

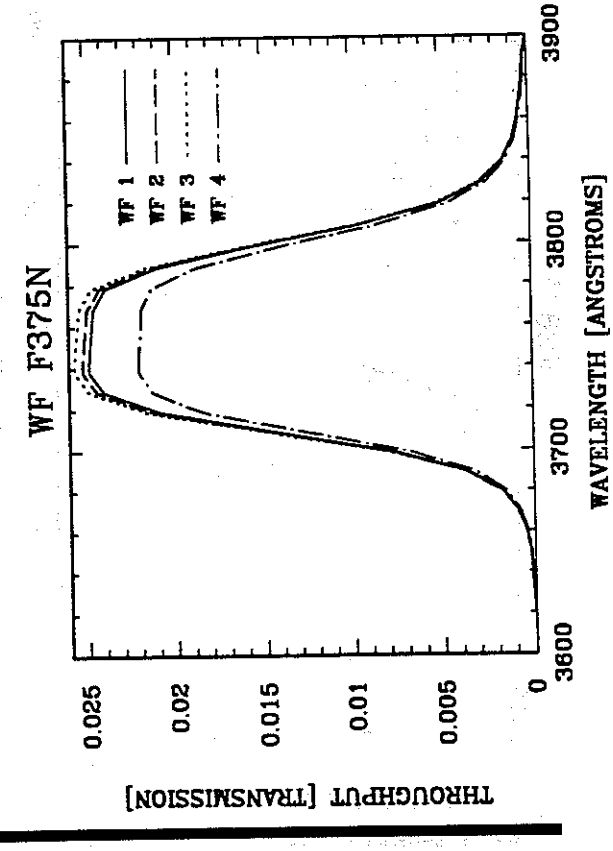

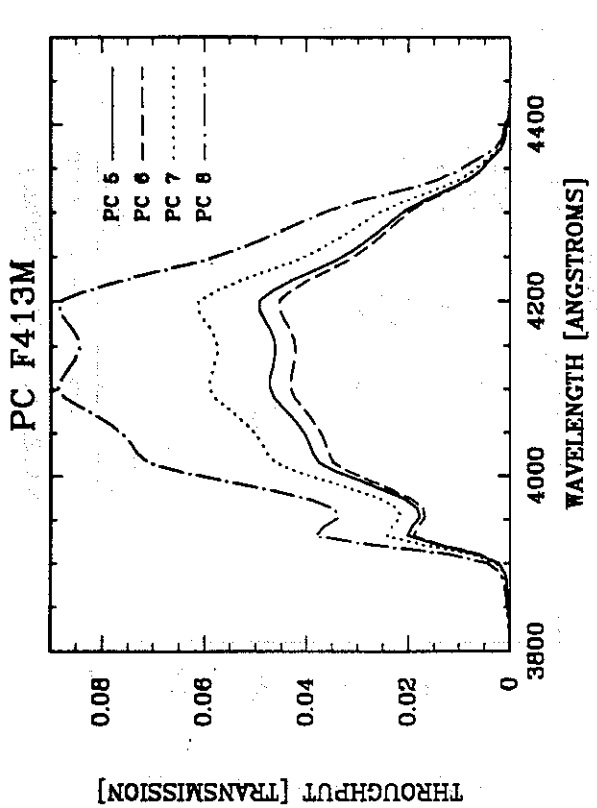
PC F413M
PC 5
PC 6
PC 7
PC 8
THROUGHPUT [TRANSMISSION]
WAVELENGTH [ANGSTROMS]
0
0.02
0.04
0.06
0.08
3800
4000
4200
4400

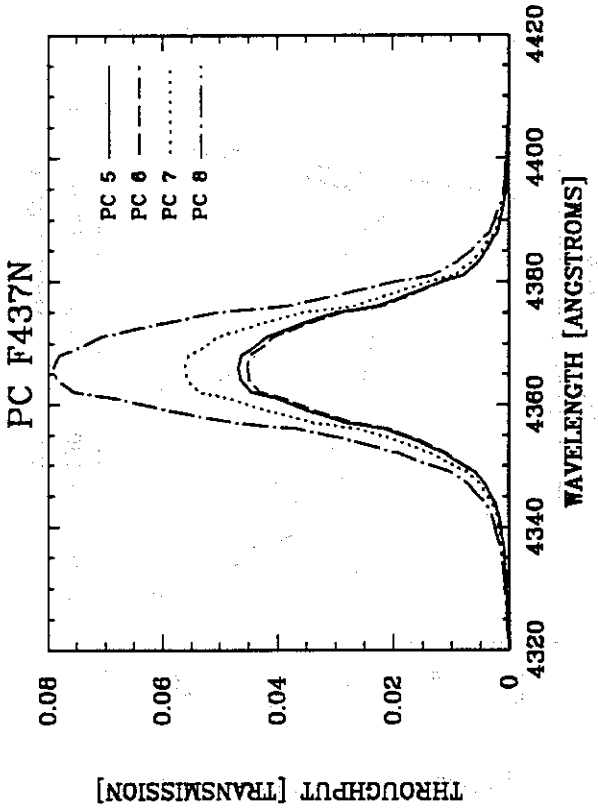
PC F437N
PC 5
PC 6
PC 7
PC 8
THROUGHPUT [TRANSMISSION]
WAVELENGTH [ANGSTROMS]
0
0.02
0.04
0.06
0.08
4320
4340
4360
4380
4400
4420

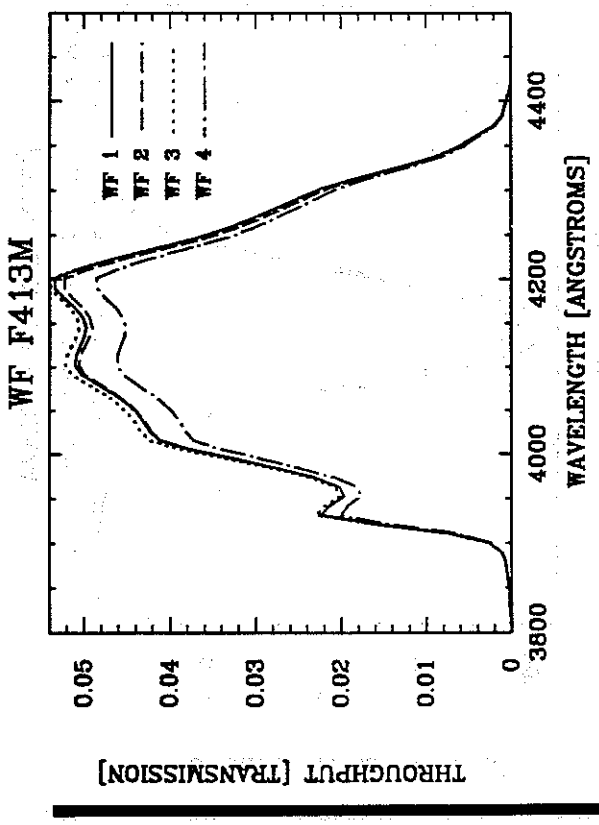
WF F413M
WF 1
WF 2
WF 3
WF 4
THROUGHPUT [TRANSMISSION]
WAVELENGTH [ANGSTROMS]
0
0.01
0.02
0.03
0.04
0.05
3800
4000
4200
4400

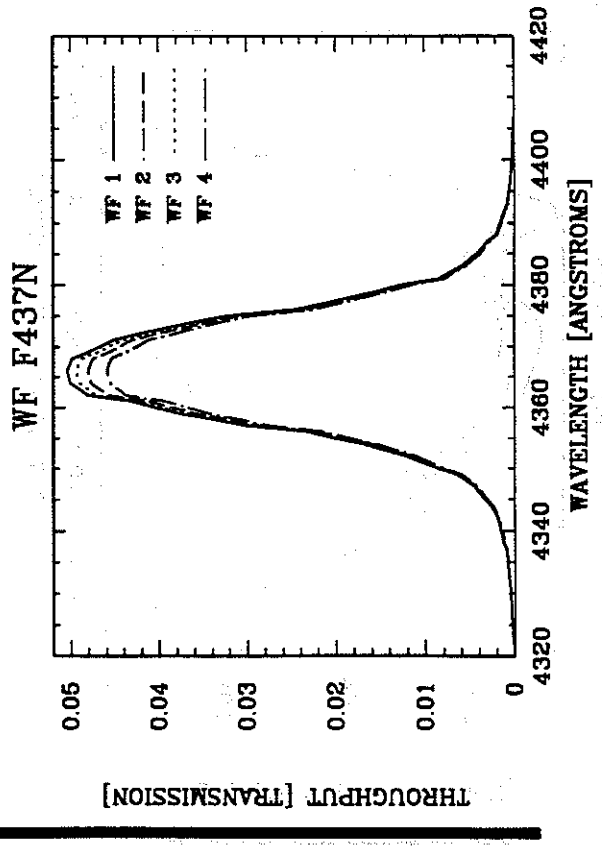
WF F437N
WF 1
WF 2
WF 3
WF 4
THROUGHPUT [TRANSMISSION]
WAVELENGTH [ANGSTROMS]
0
0.01
0.02
0.03
0.04
0.05
4320
4340
4360
4380
4400
4420

A.3 Filter Passbands including WF/PC + OTA Response (continued)

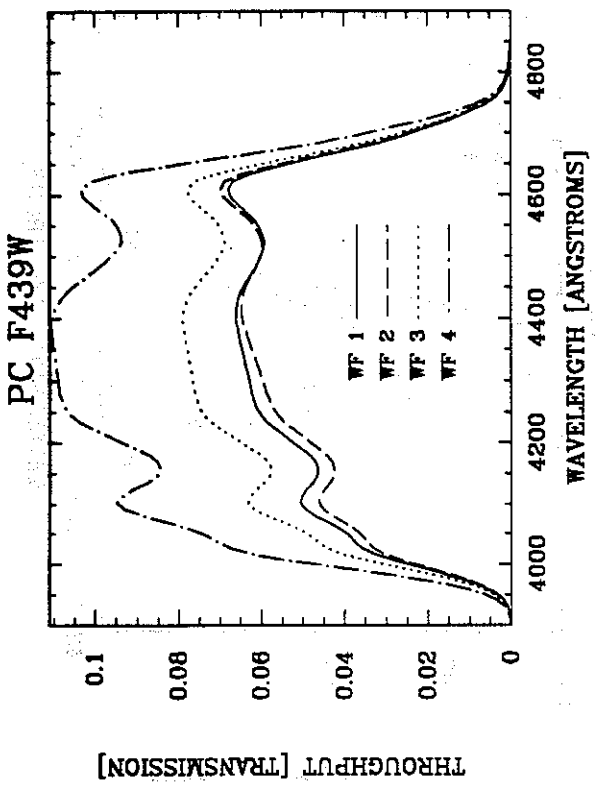

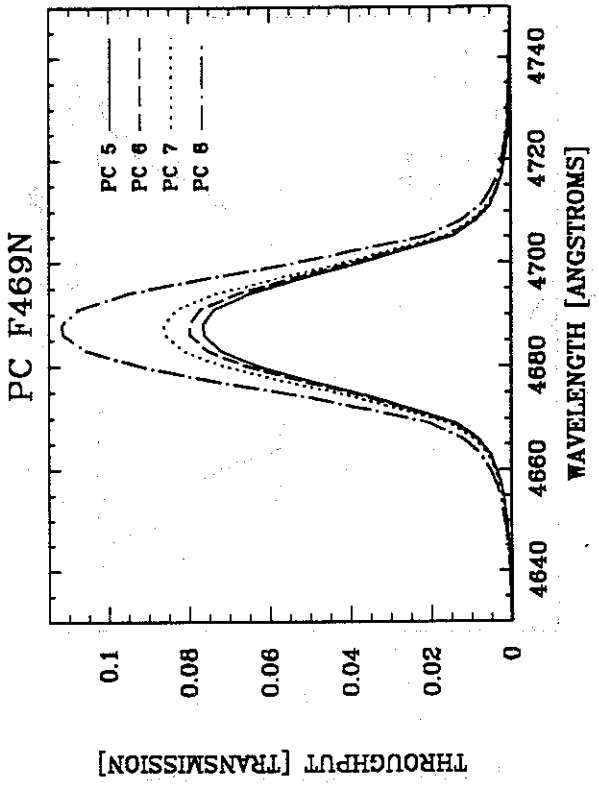

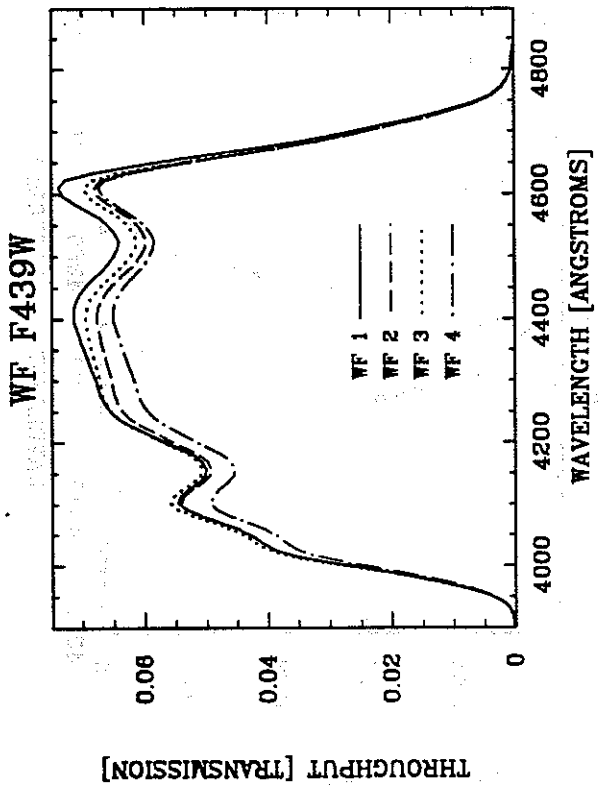

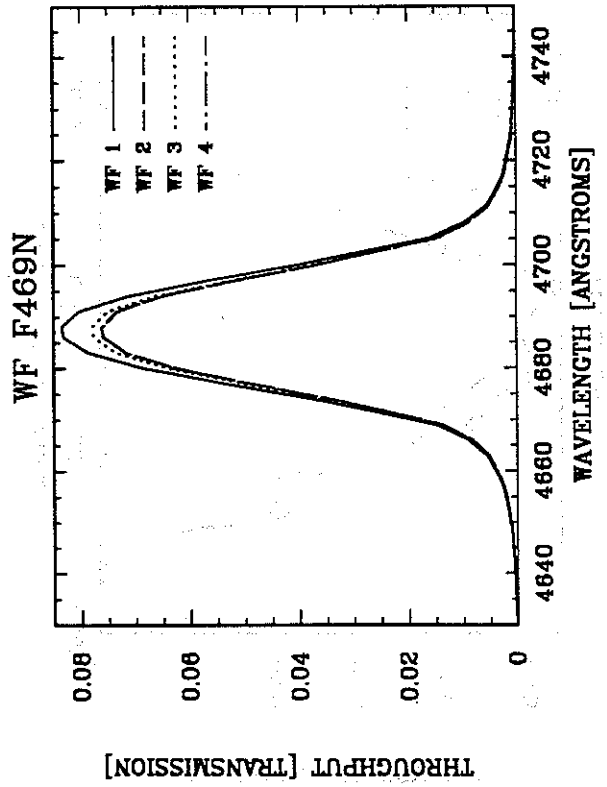

A.3 Filter Passbands including WF/PC + OTA Response (continued)

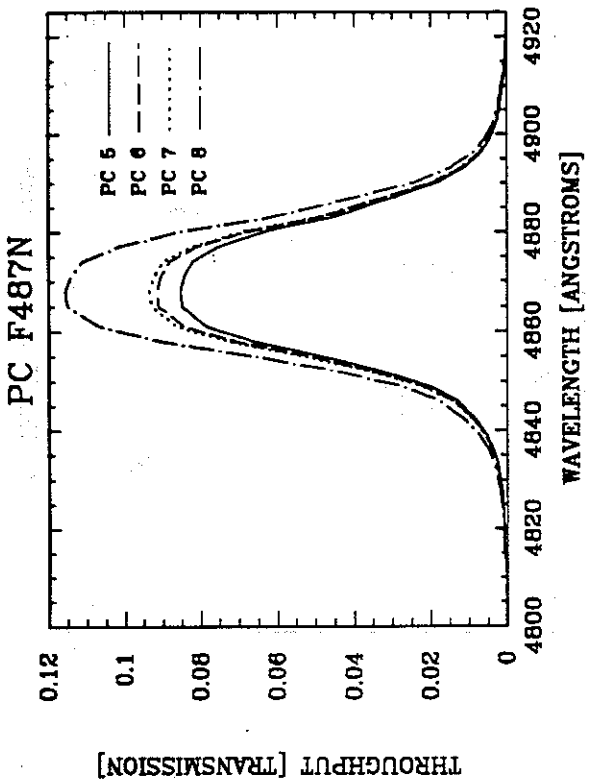

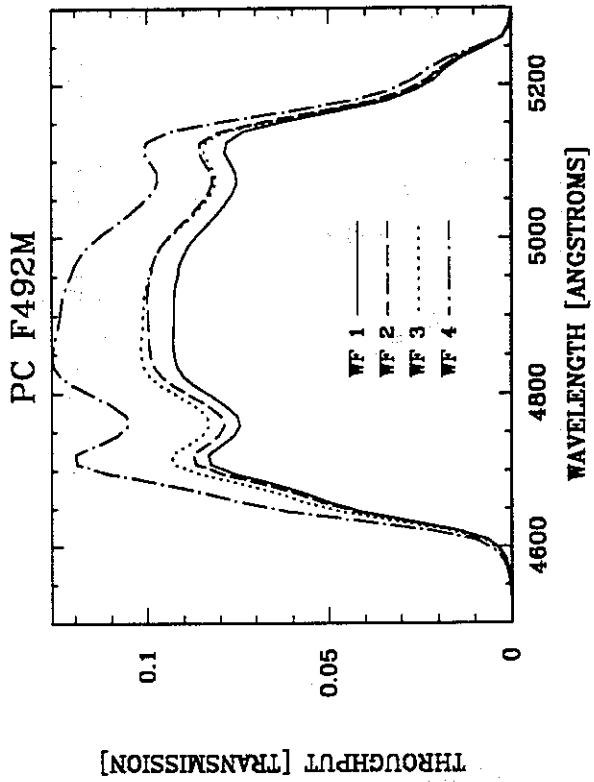

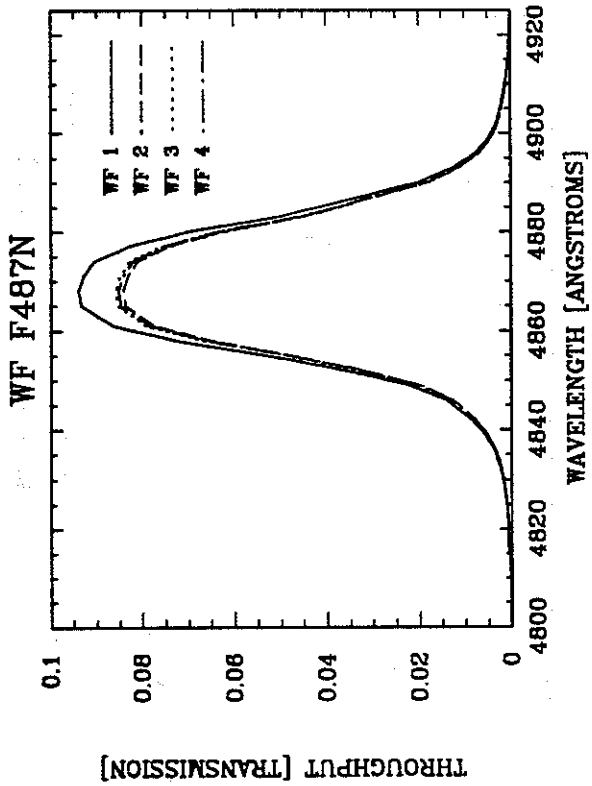

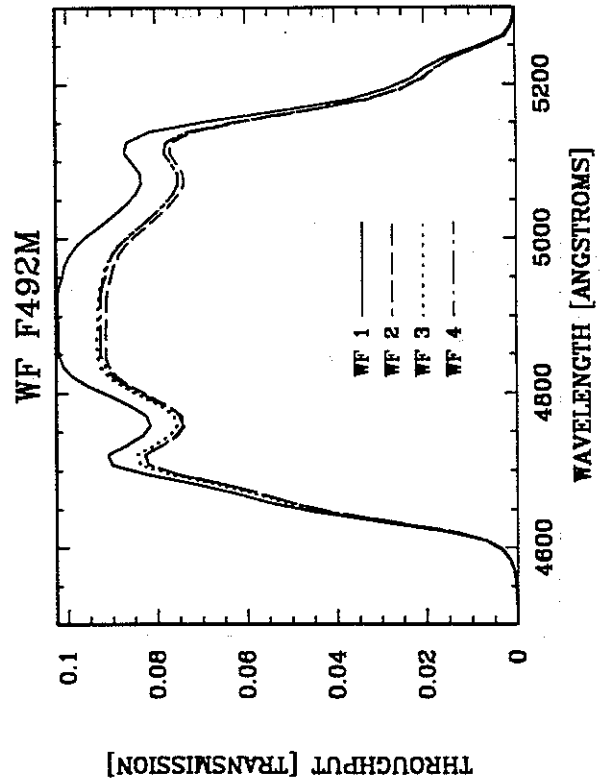

A.3 Filter Passbands including WF/PC + OTA Response (continued)

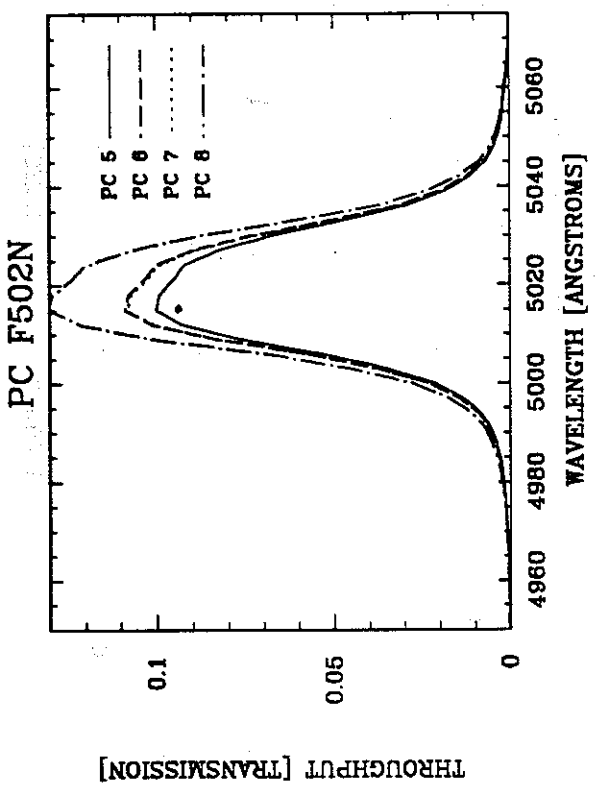

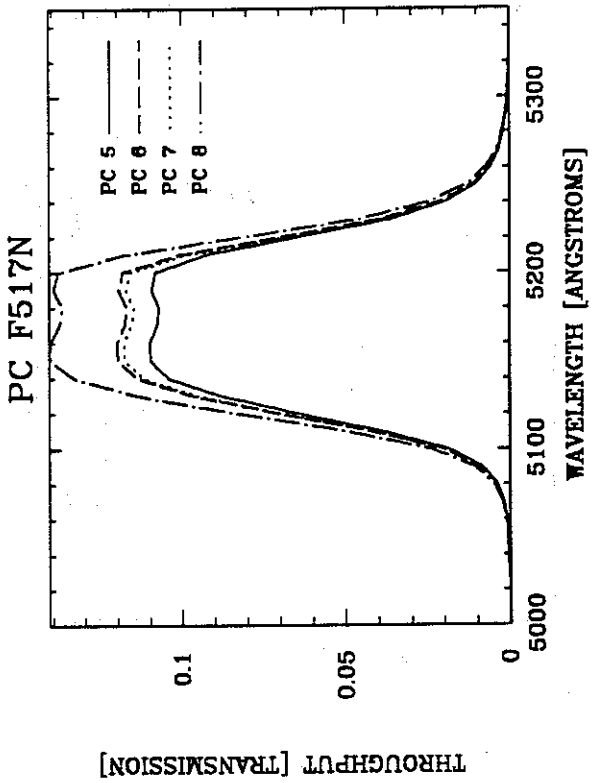

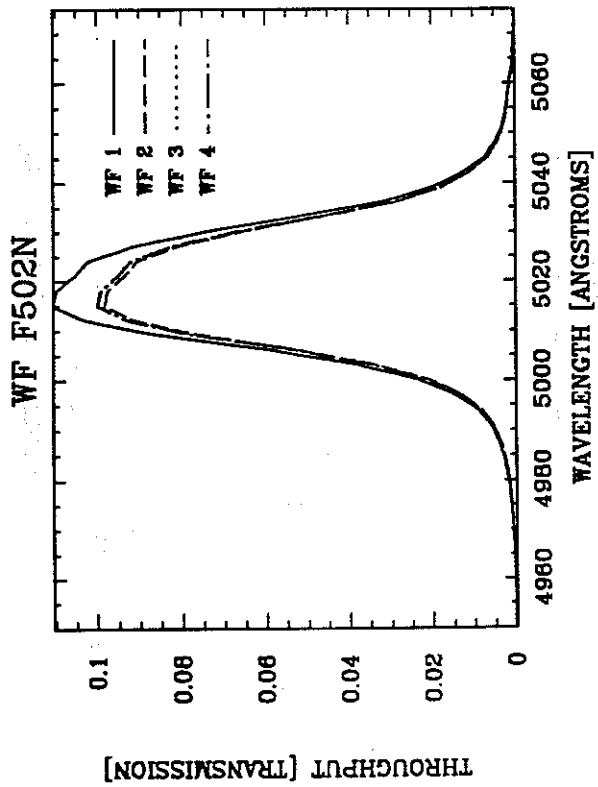

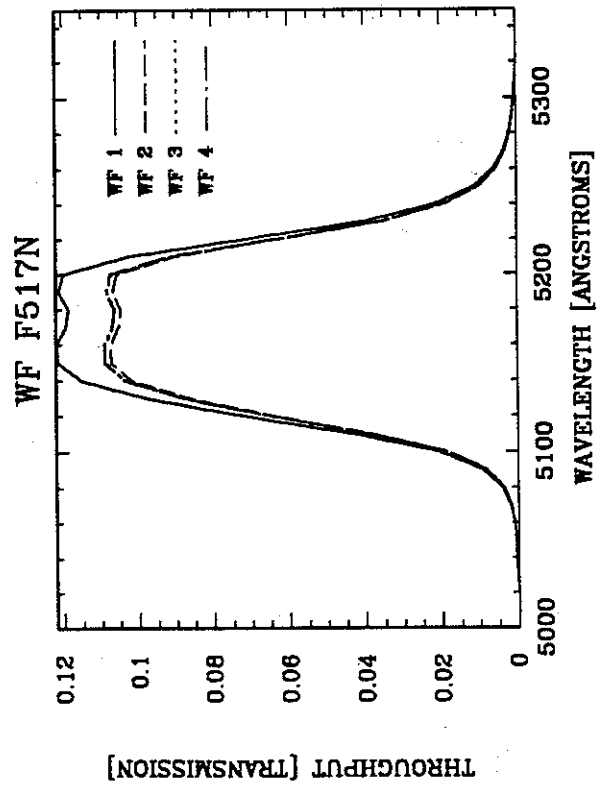

A.3 Filter Passbands including WF/PC + OTA Response (continued)

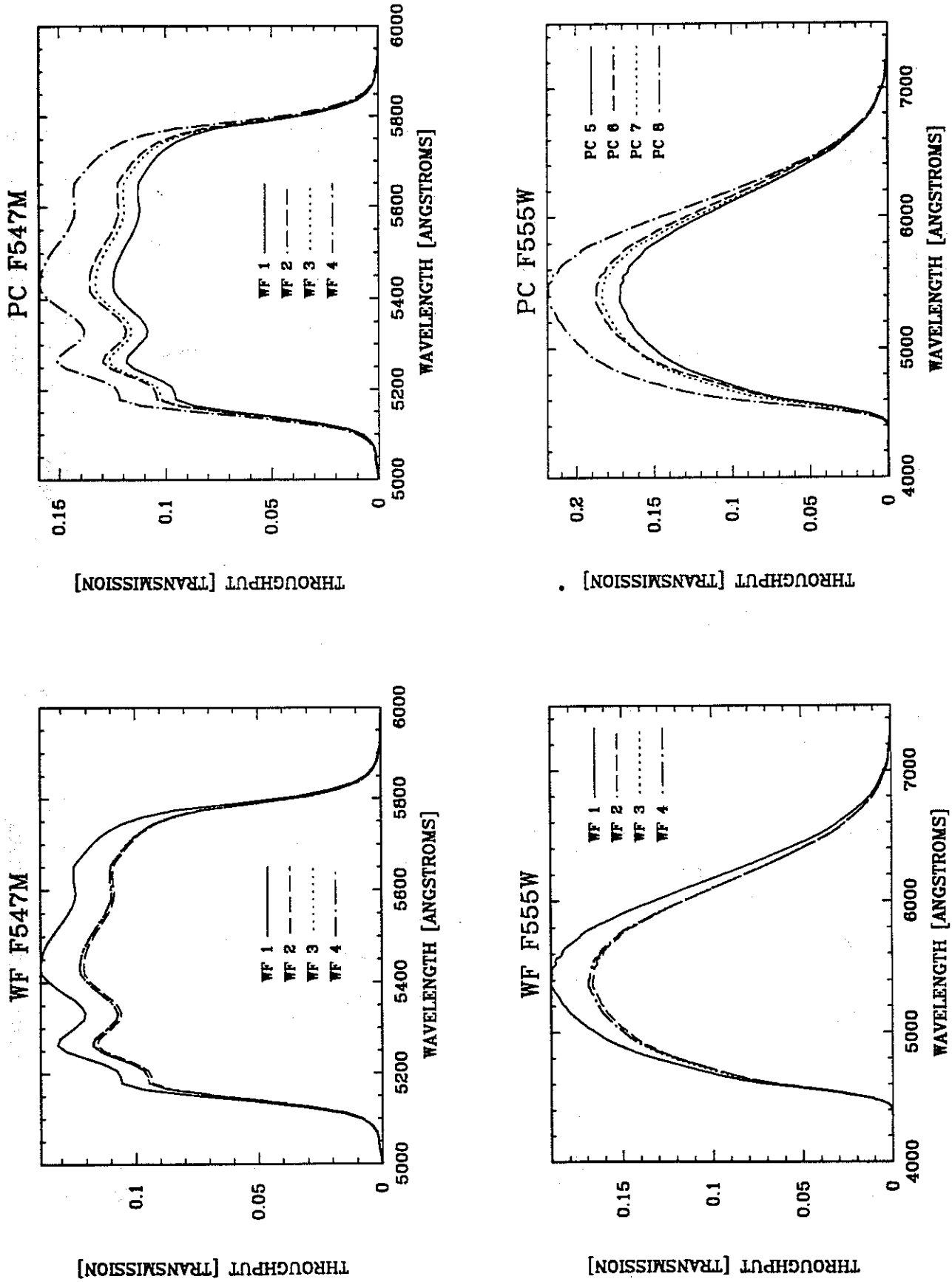

A.3 Filter Passbands including WF/PC + OTA Response (continued)

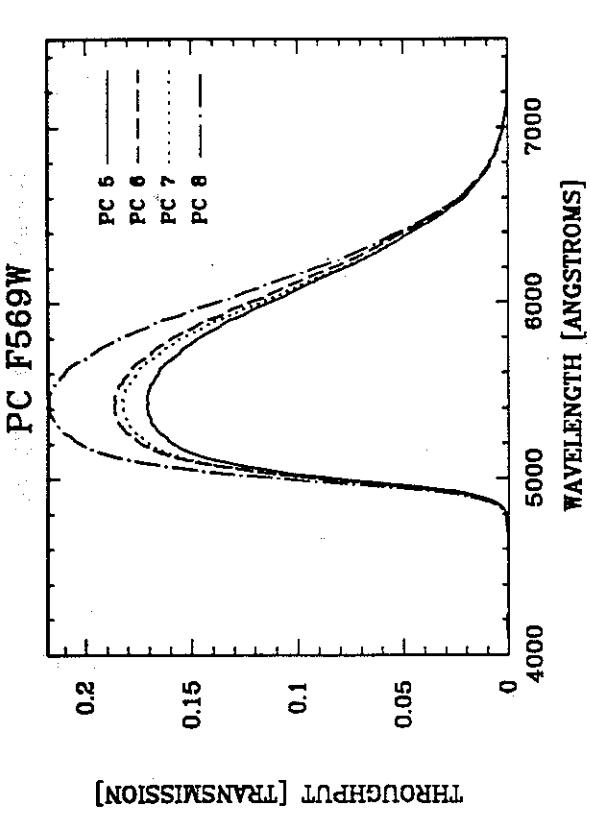

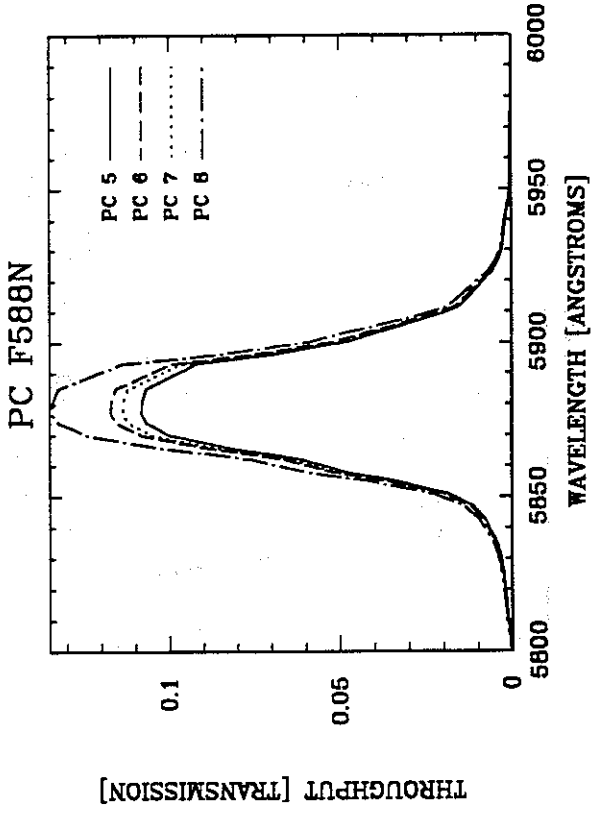

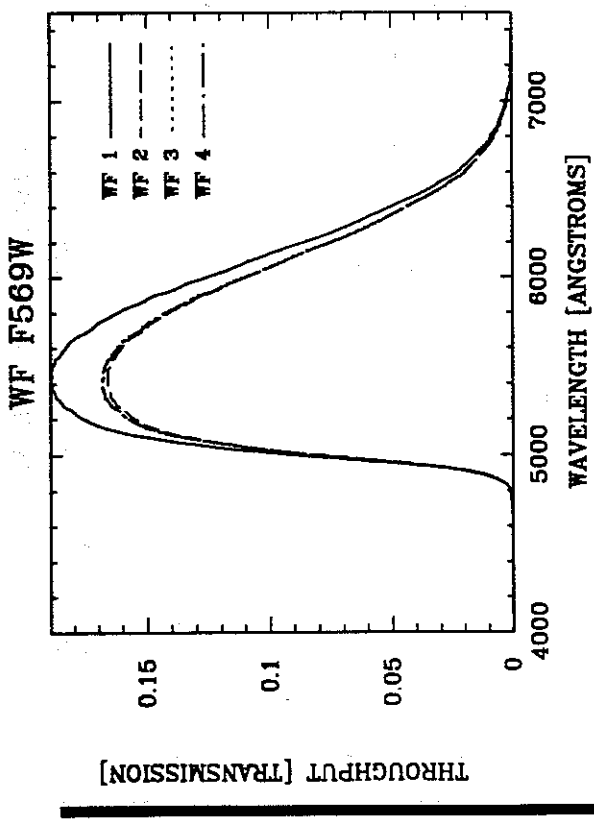

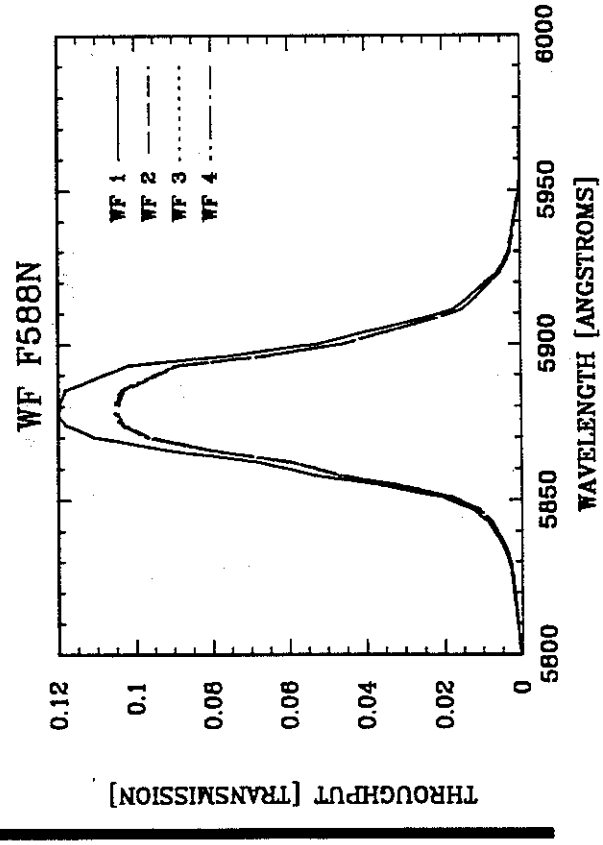

A.3 Filter Passbands including WF/PC + OTA Response (continued)

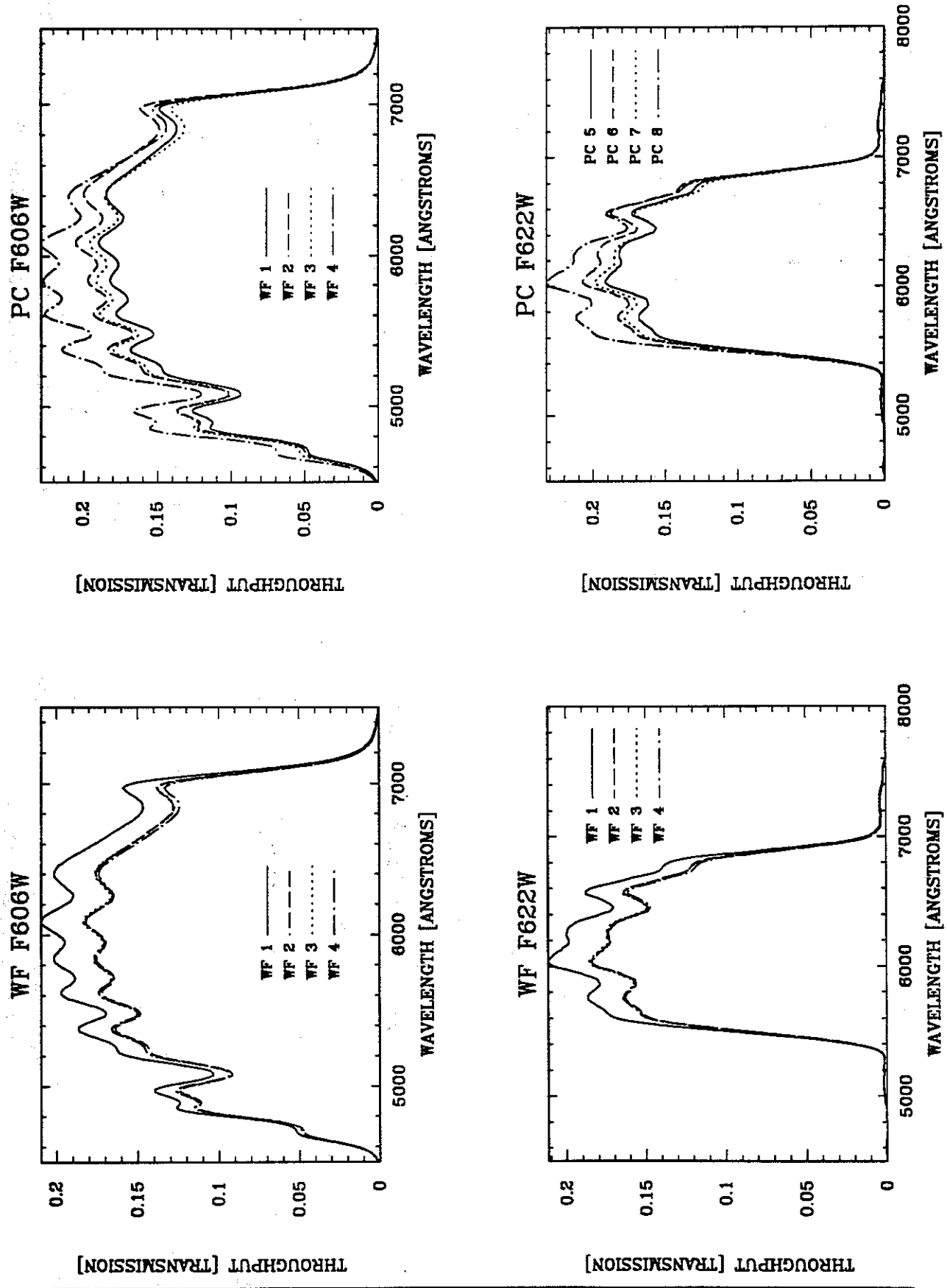

A.3 Filter Passbands including WF/PC + OTA Response (continued)

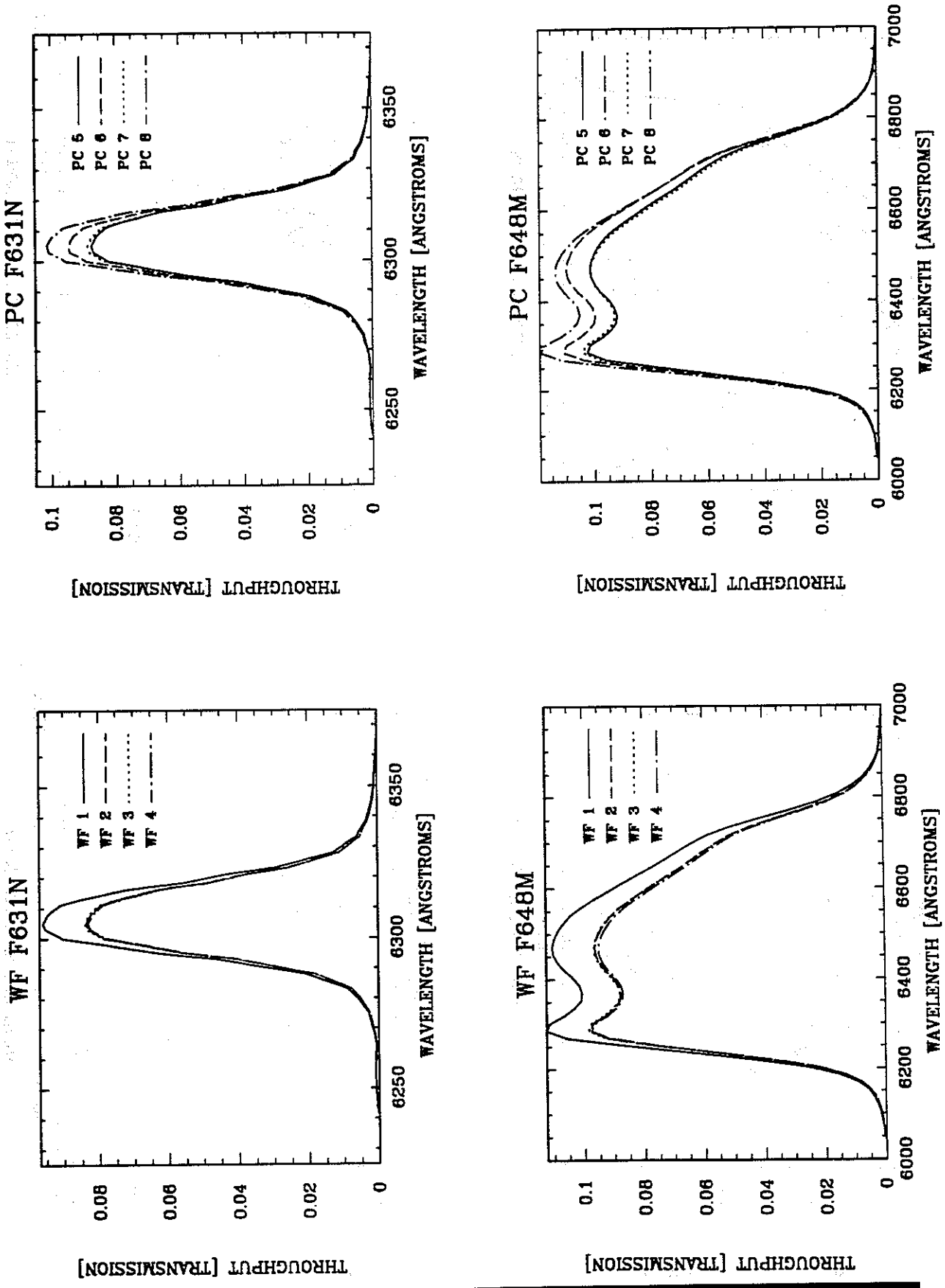

A.3 Filter Passbands including WF/PC + OTA Response (continued)

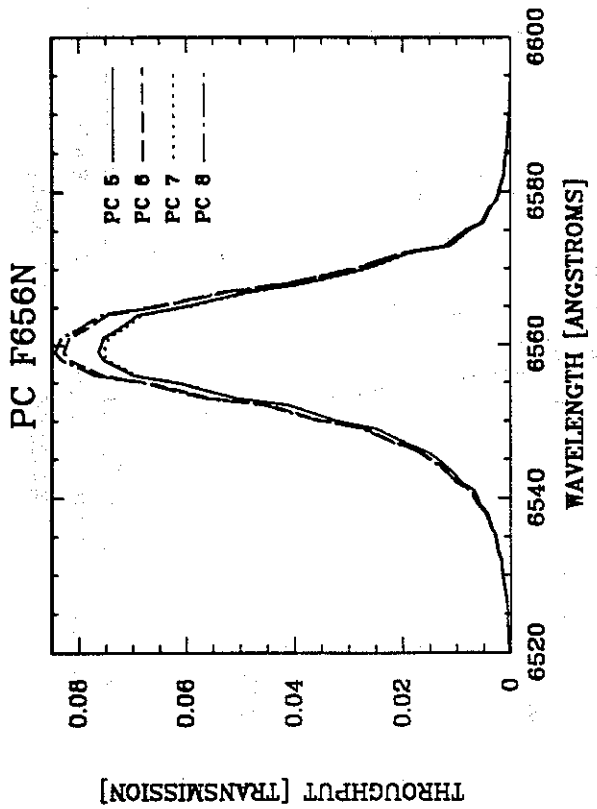

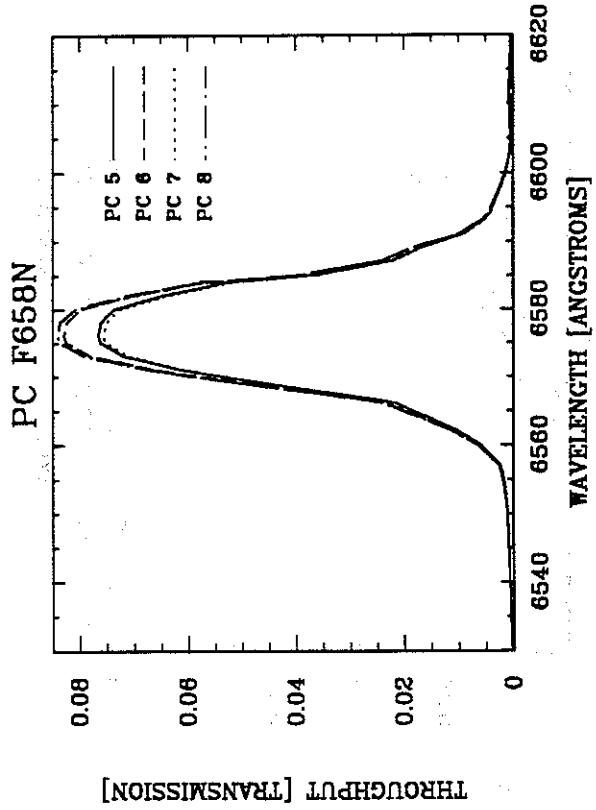

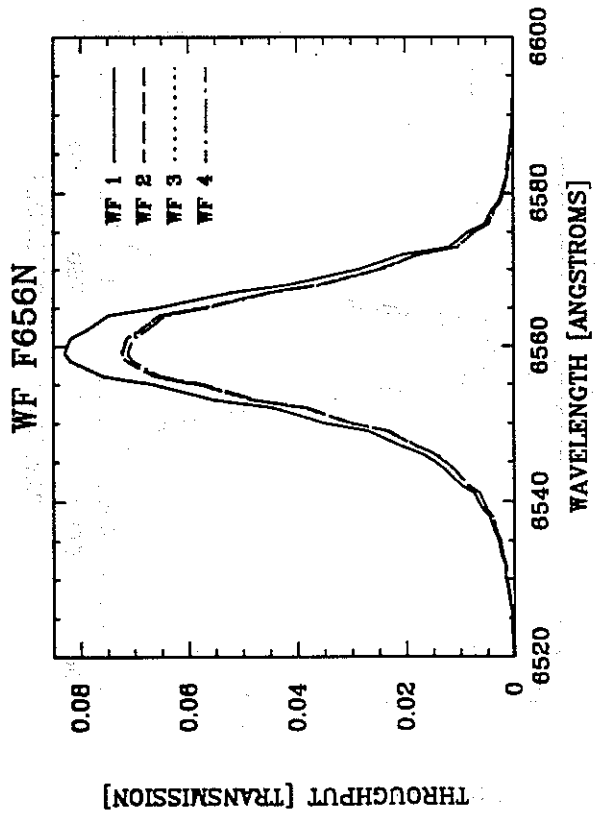

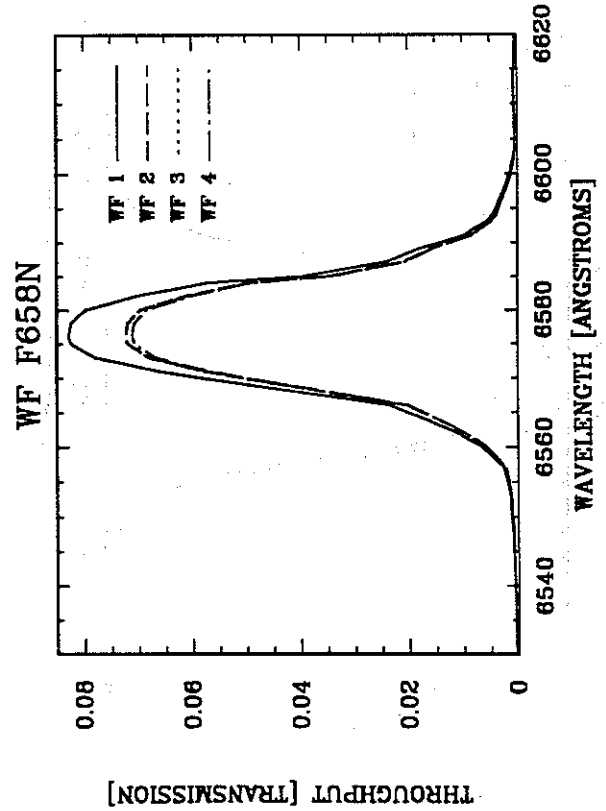

A.3 Filter Passbands including WF/PC + OTA Response (continued)

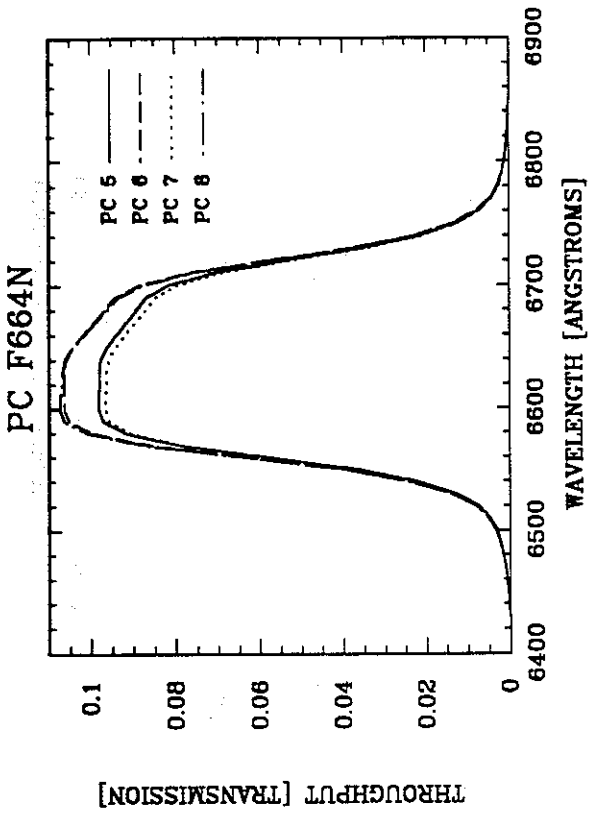

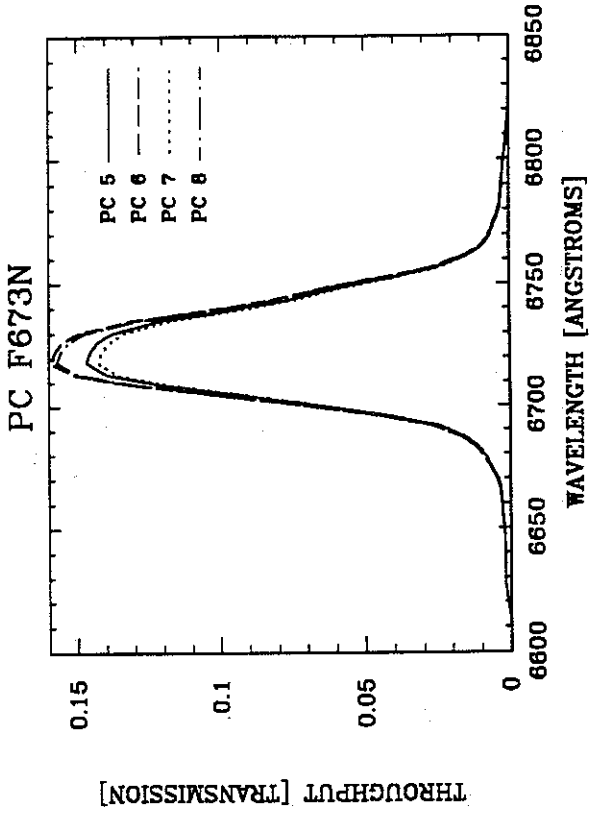

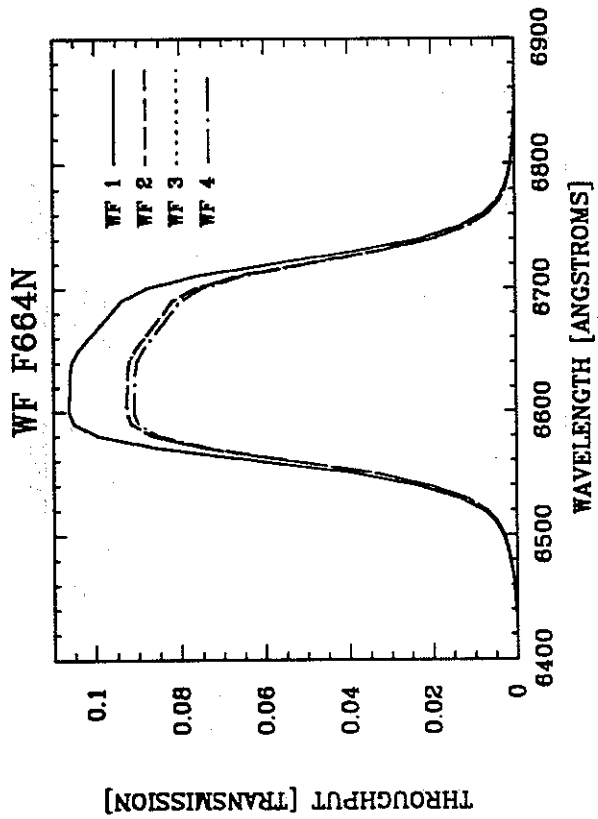

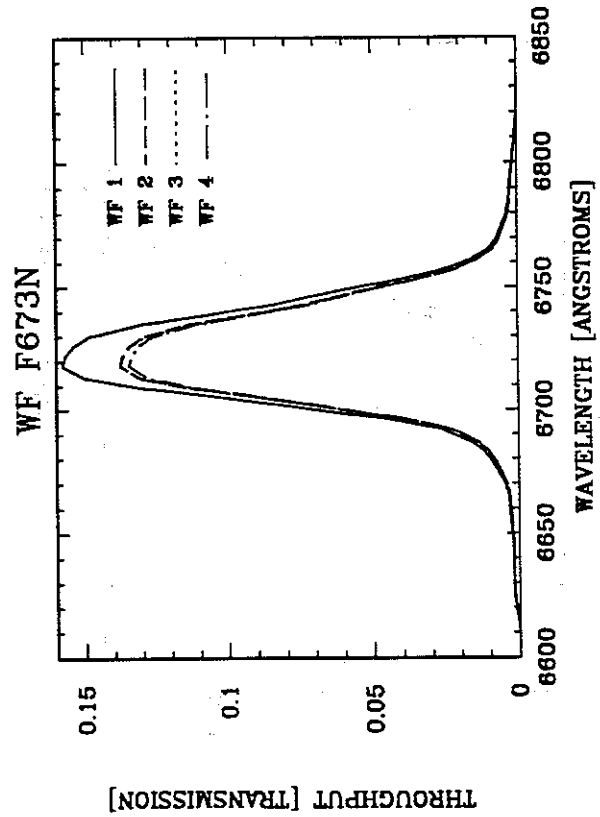

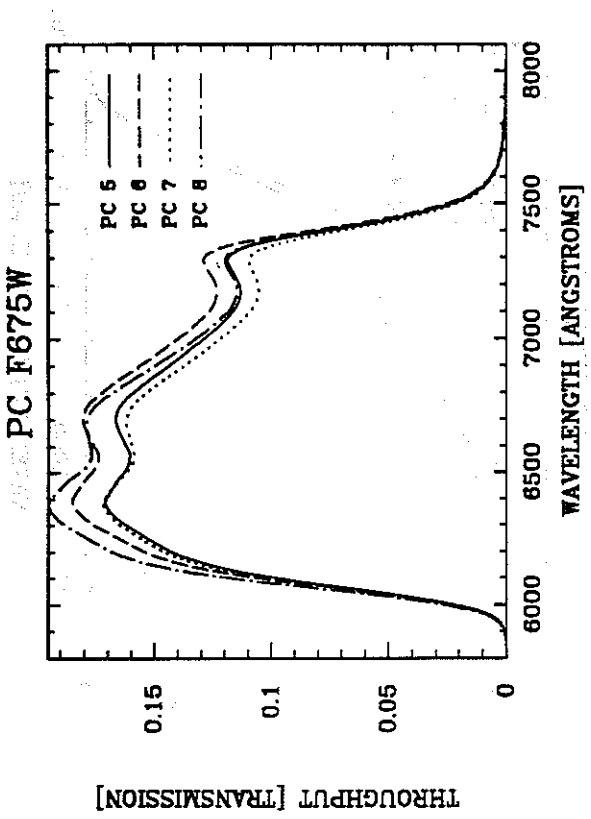
PC F675W
PC 5
PC 6
PC 7
PC 8
0
0.05
0.1
0.15
6000
6500
7000
7500
8000
WAVELENGTH [ANGSTROMS]
THROUGHPUT [TRANSMISSION]

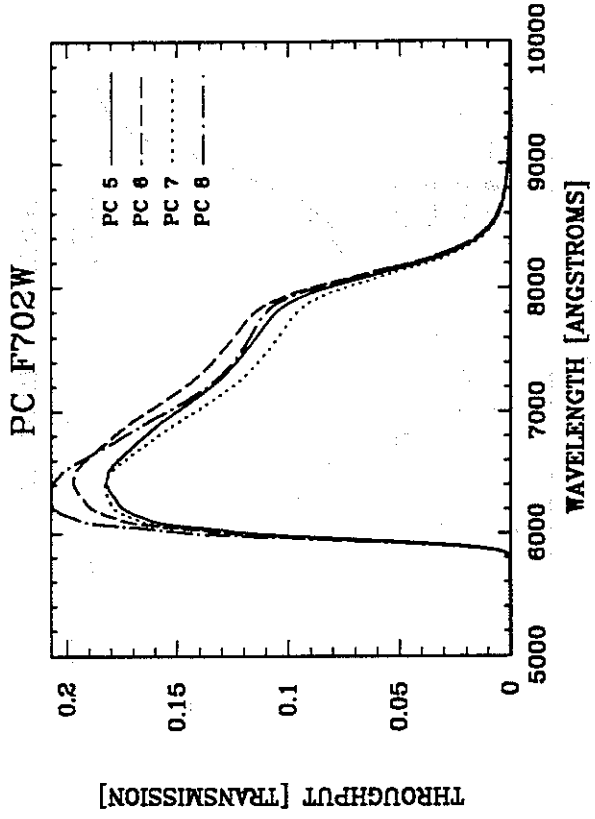
PC F702W
PC 5
PC 6
PC 7
PC 8
0
0.05
0.1
0.15
0.2
5000
6000
7000
8000
9000
10000
WAVELENGTH [ANGSTROMS]
THROUGHPUT [TRANSMISSION]

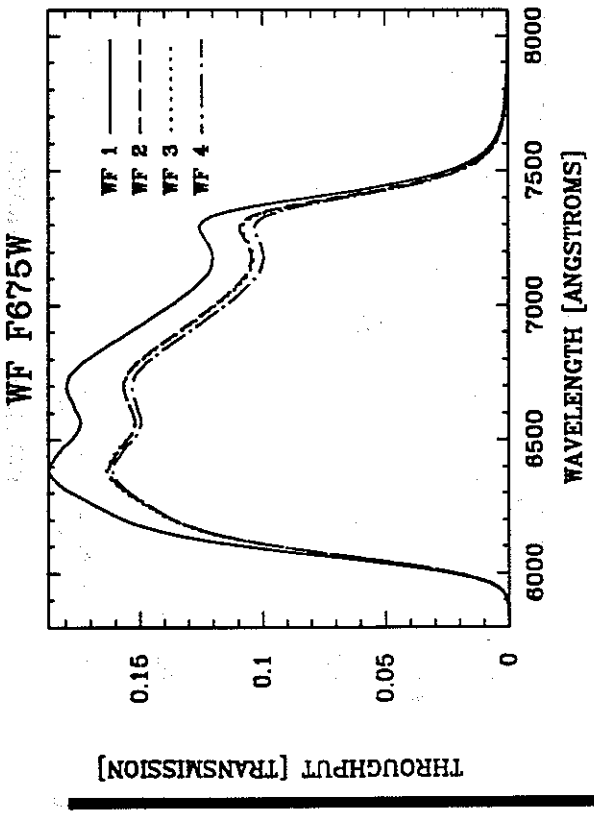
WF F675W
WF 1
WF 2
WF 3
WF 4
0
0.05
0.1
0.15
6000
6500
7000
7500
8000
WAVELENGTH [ANGSTROMS]
THROUGHPUT [TRANSMISSION]

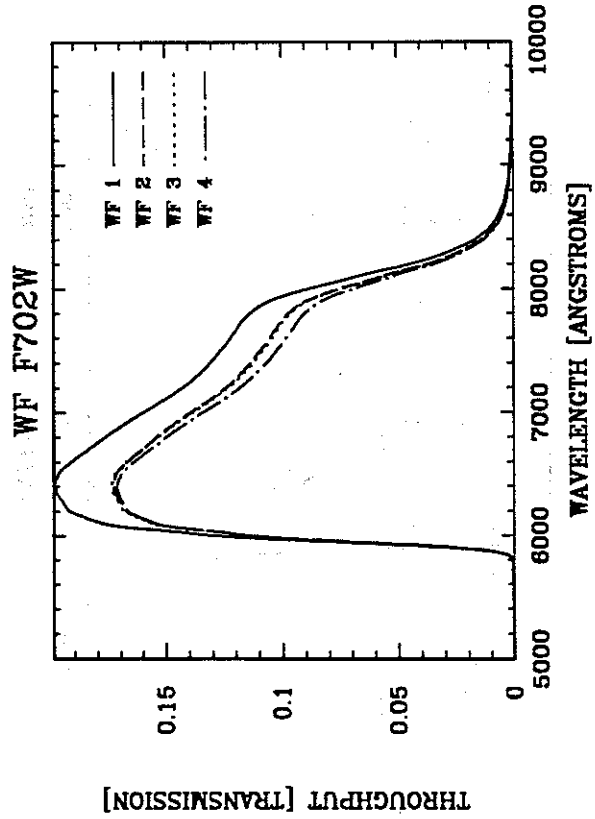
WF F702W
WF 1
WF 2
WF 3
WF 4
0
0.05
0.1
0.15
5000
6000
7000
8000
9000
10000
WAVELENGTH [ANGSTROMS]
THROUGHPUT [TRANSMISSION]

A.3 Filter Passbands including WF/PC + OTA Response (continued)

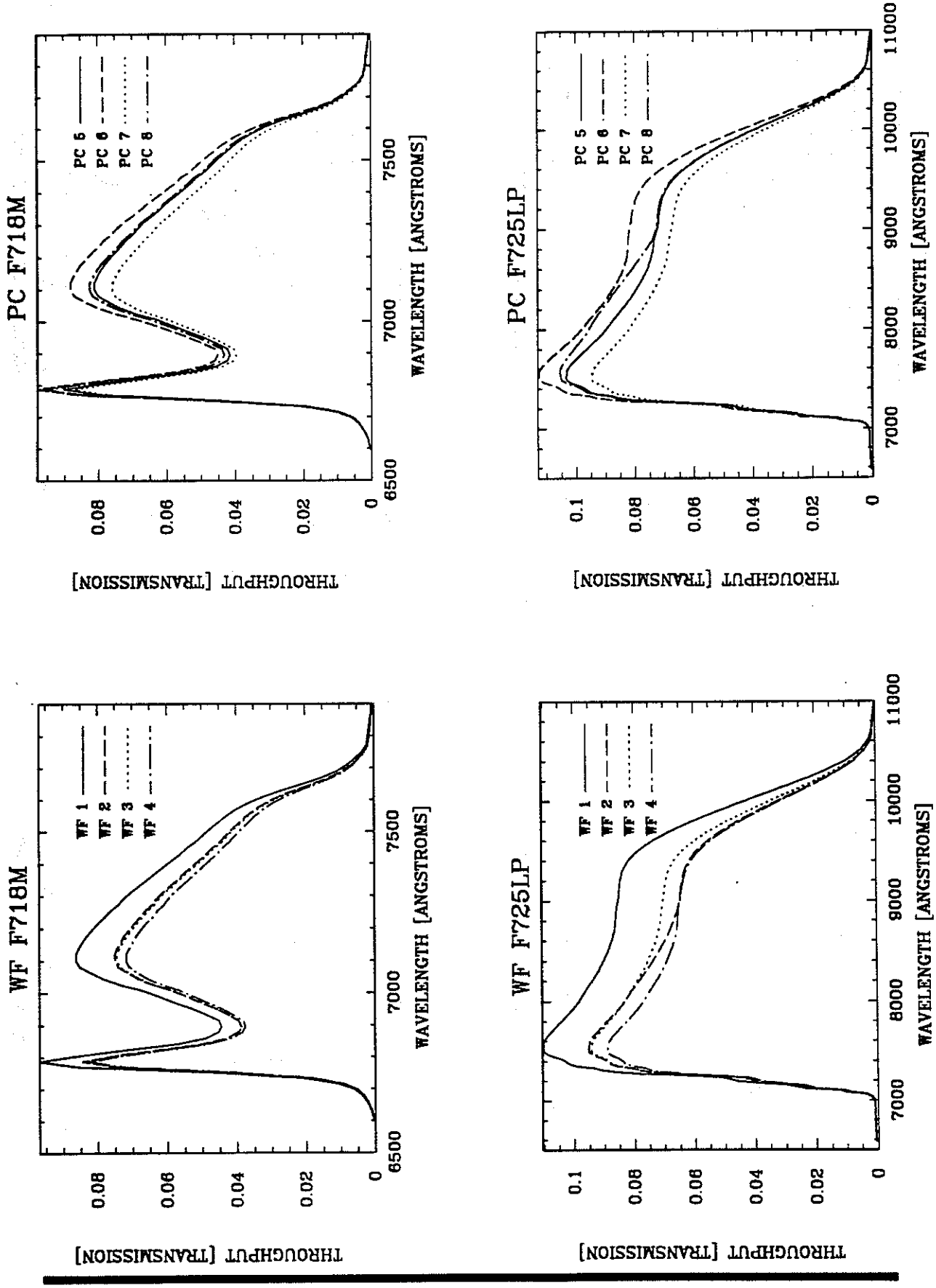

A.3 Filter Passbands including WF/PC + OTA Response (continued)

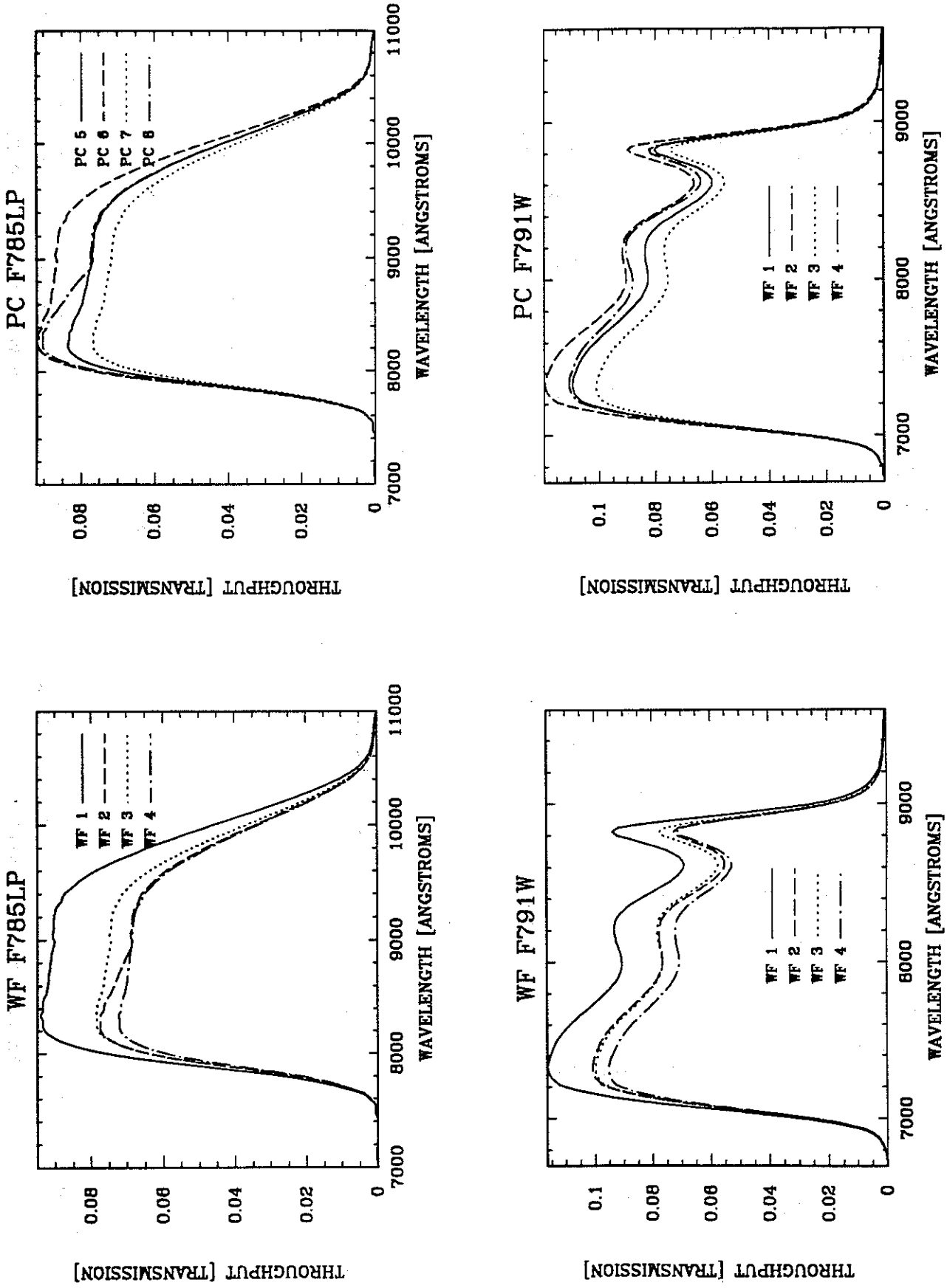

A.3 Filter Passbands including WF/PC + OTA Response (continued)

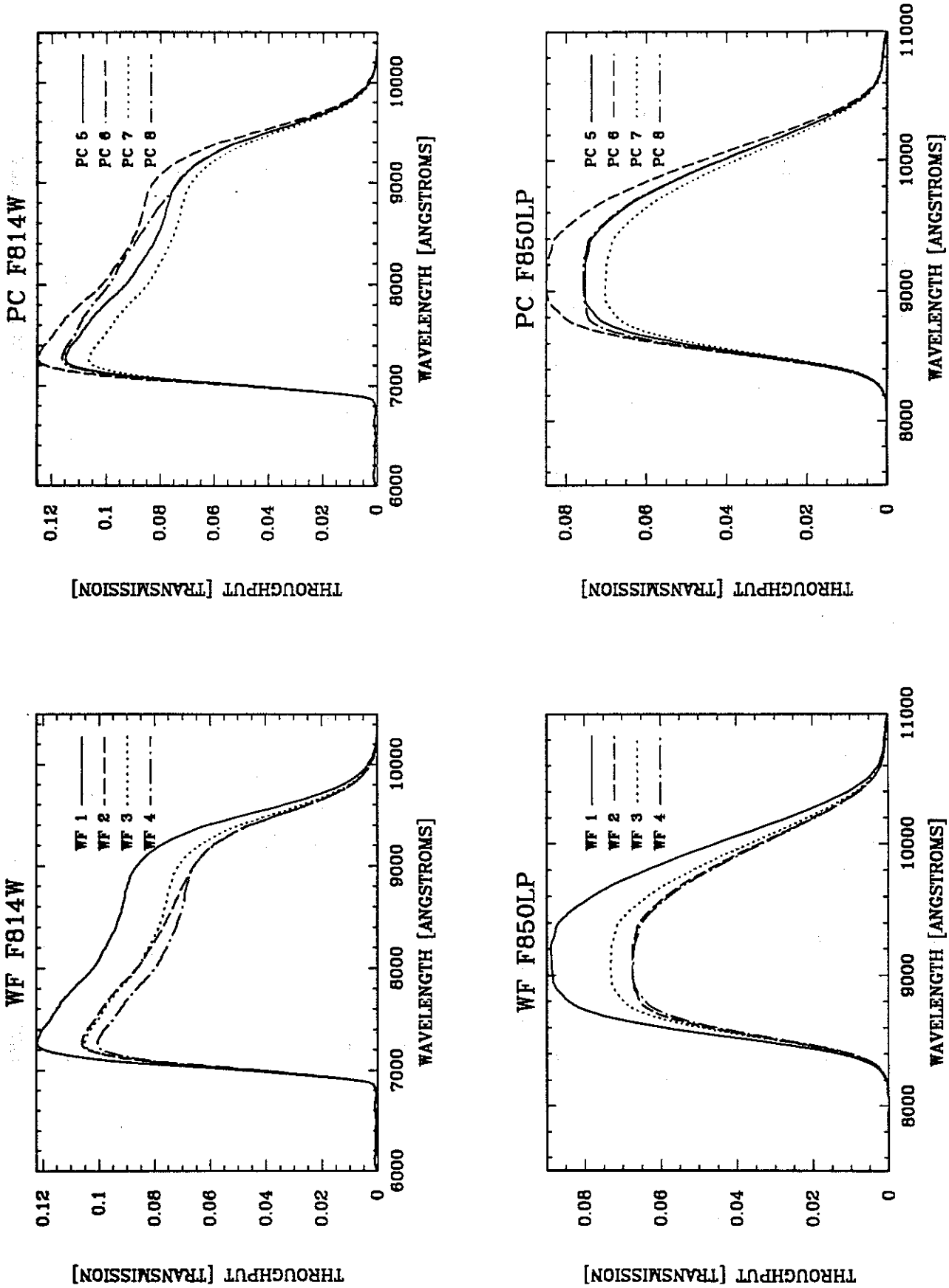

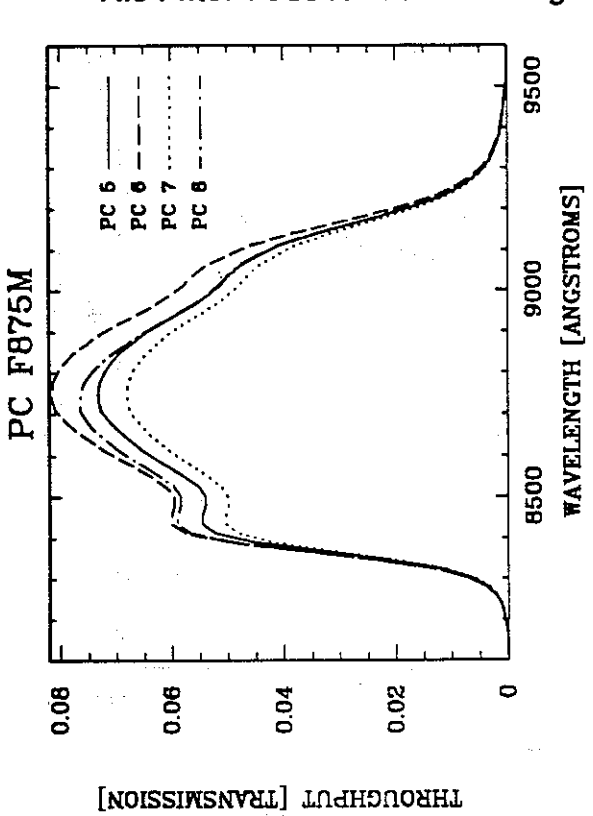
PC F875M
PC 5
PC 6
PC 7
PC 8
THROUGHPUT [TRANSMISSION]
0.08
0.06
0.04
0.02
0
8500
9000
9500
WAVELENGTH [ANGSTROMS]

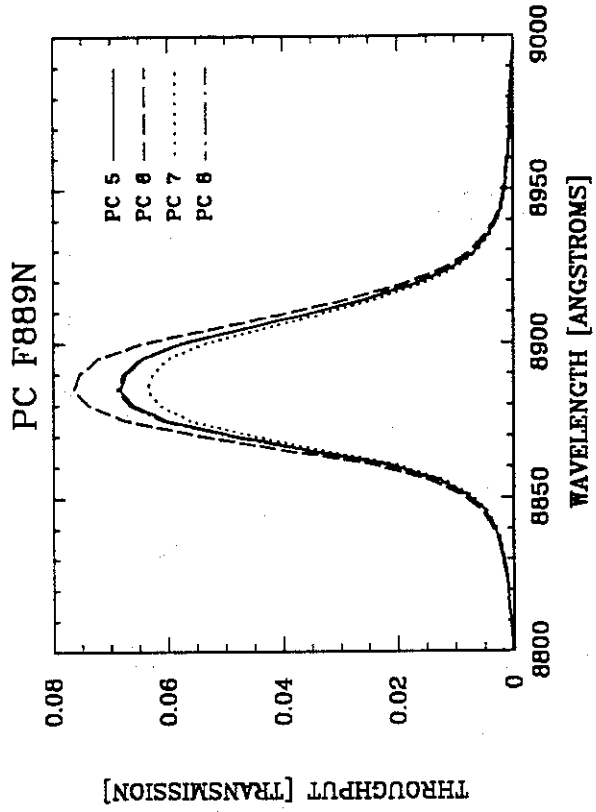
PC F889N
PC 5
PC 6
PC 7
PC 8
THROUGHPUT [TRANSMISSION]
0.08
0.06
0.04
0.02
0
8800
8850
8900
8950
9000
WAVELENGTH [ANGSTROMS]

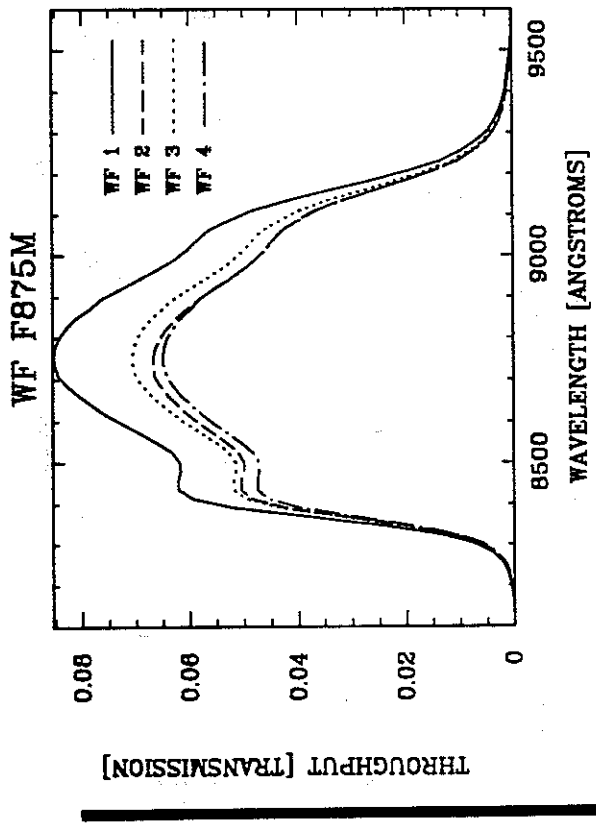
WF F875M
WF 1
WF 2
WF 3
WF 4
THROUGHPUT [TRANSMISSION]
0.08
0.06
0.04
0.02
0
8500
9000
9500
WAVELENGTH [ANGSTROMS]

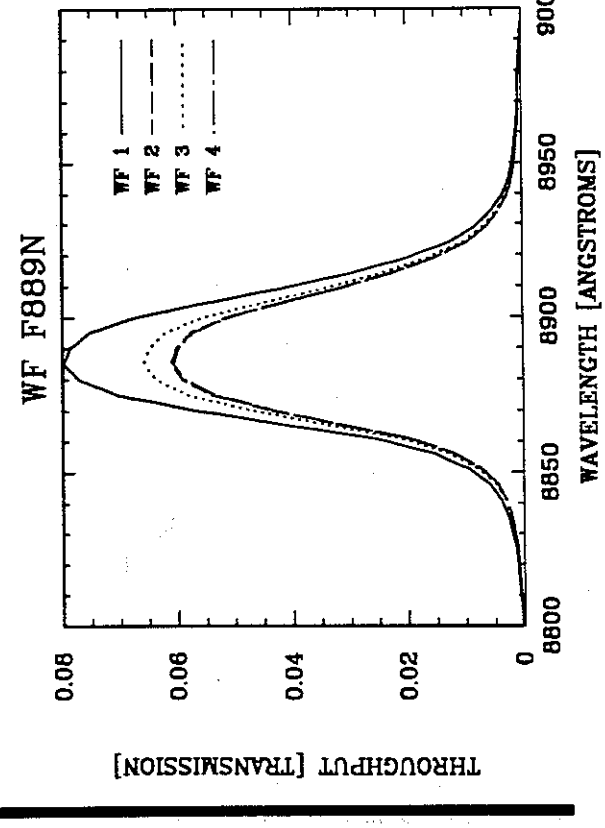
WF F889N
WF 1
WF 2
WF 3
WF 4
THROUGHPUT [TRANSMISSION]
0.08
0.06
0.04
0.02
0
8800
8850
8900
8950
9000
WAVELENGTH [ANGSTROMS]

A.3 Filter Passbands including WF/PC + OTA Response (continued)

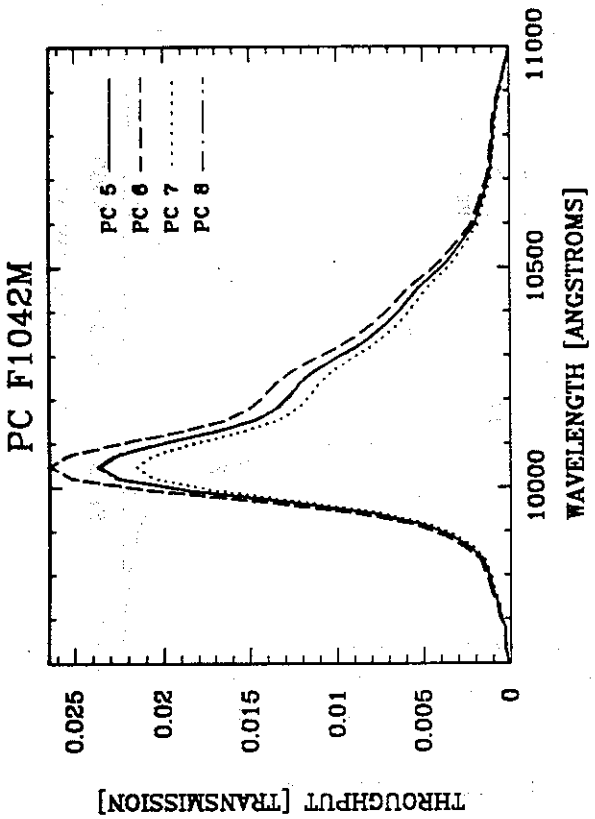

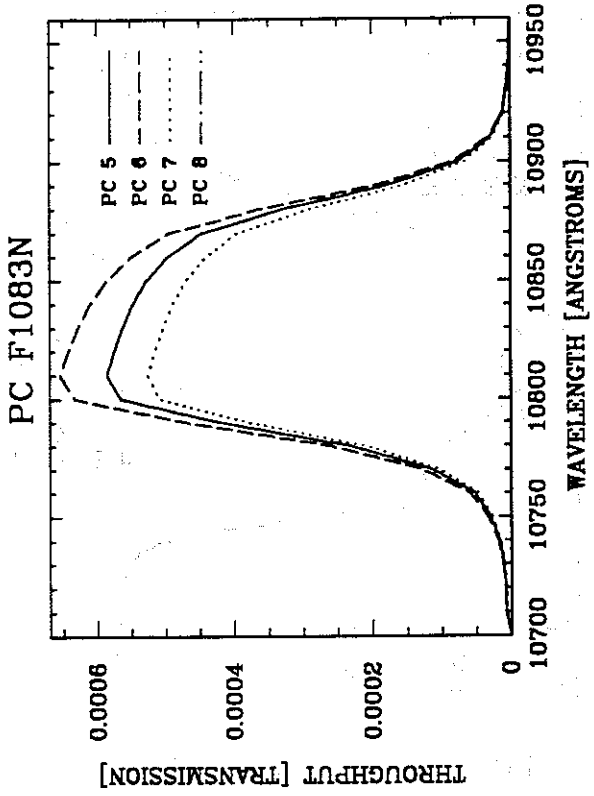

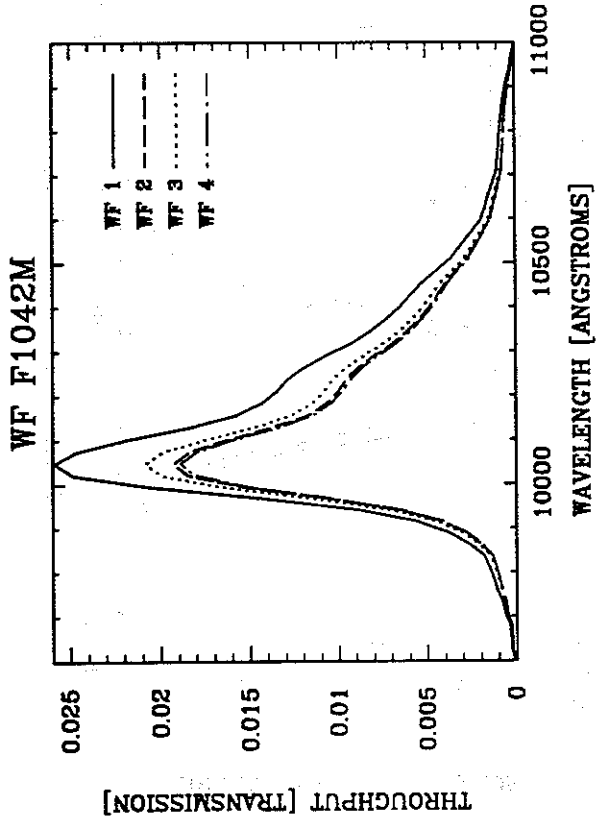

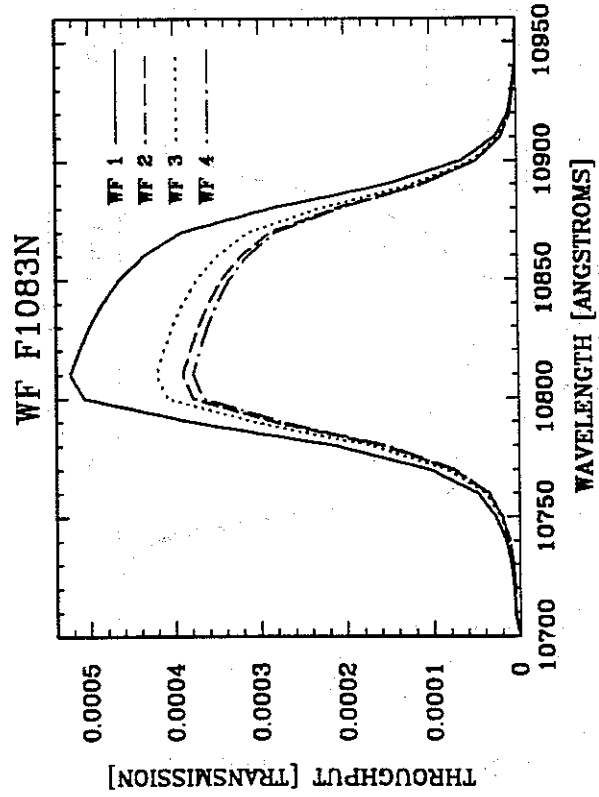

A.3 Filter Passbands including WF/PC + OTA Response (continued)

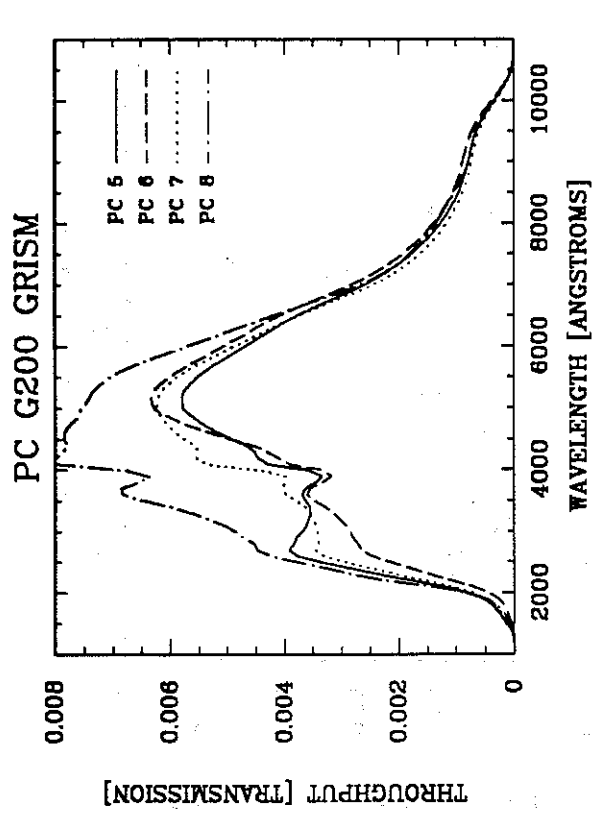

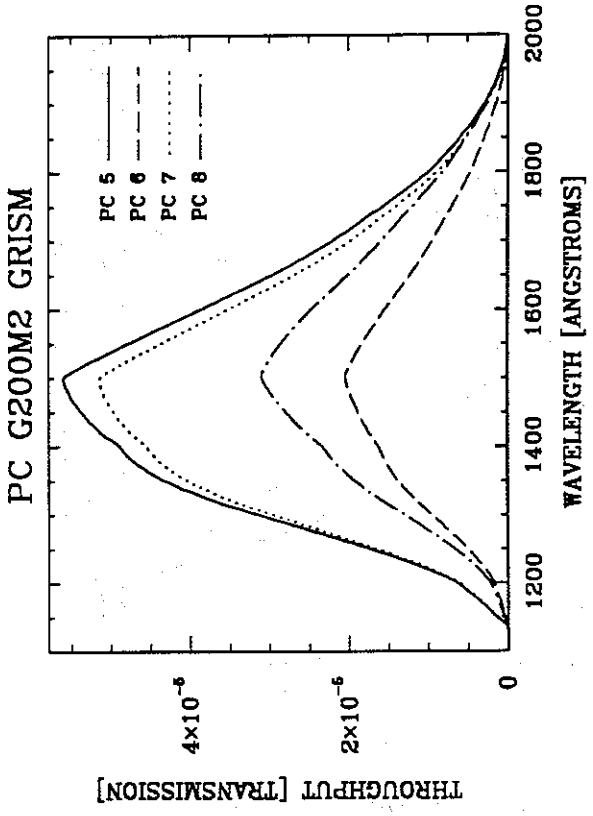

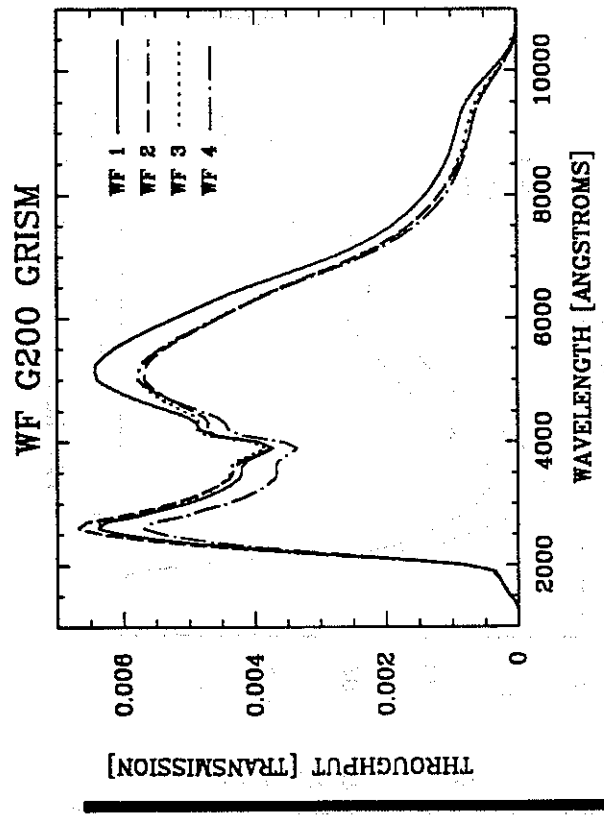

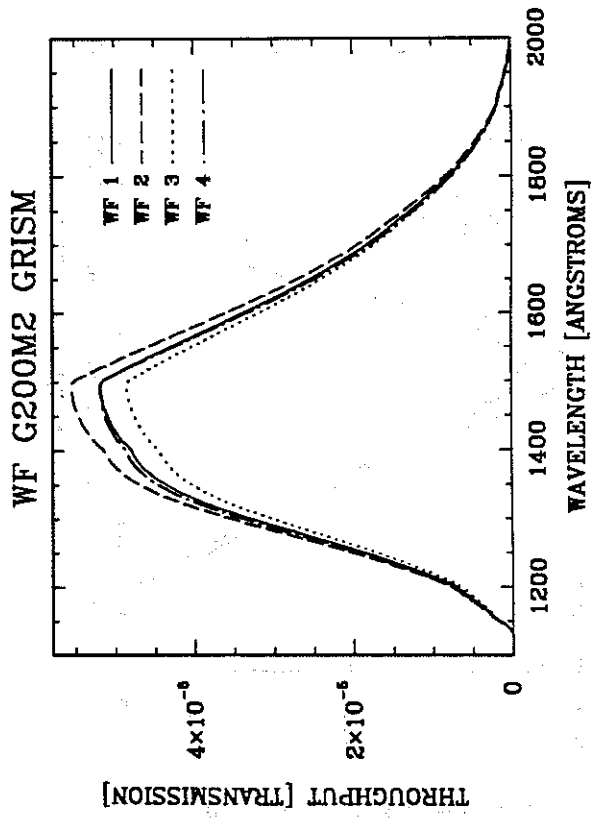

A.3 Filter Passbands including WF/PC + OTA Response (continued)

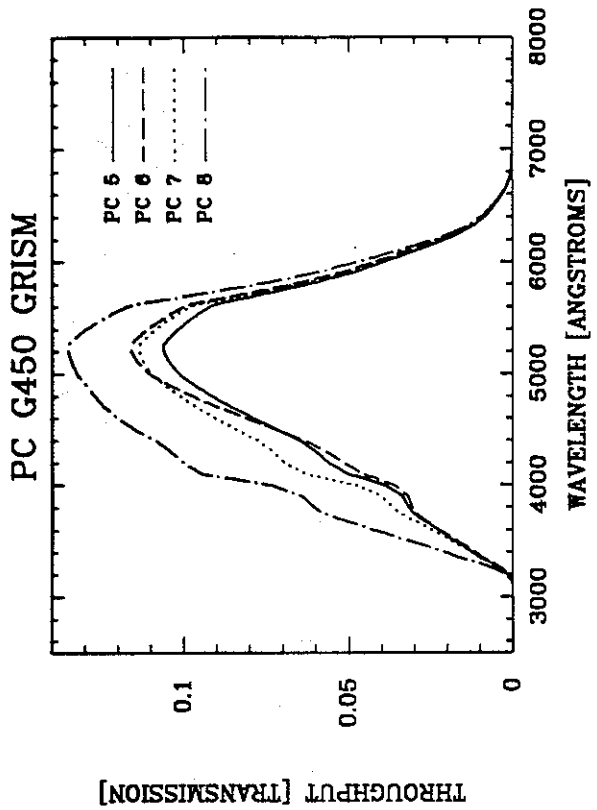

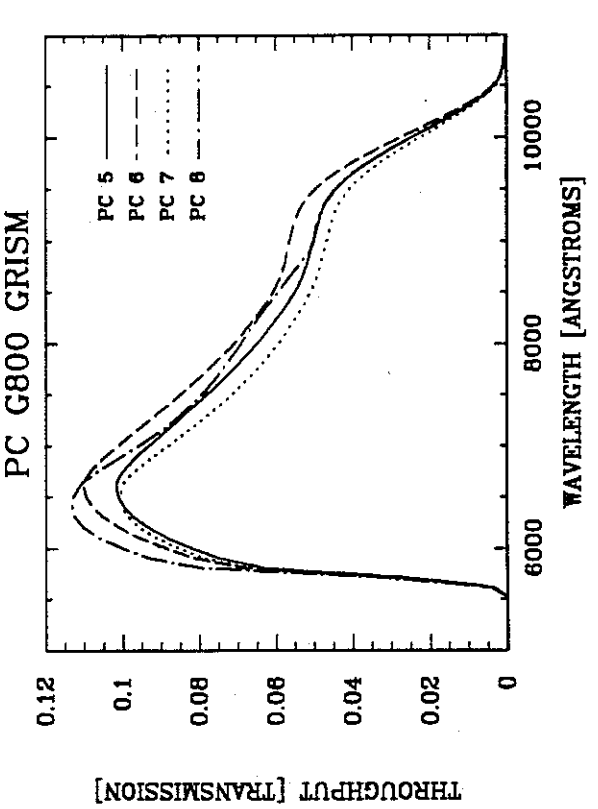

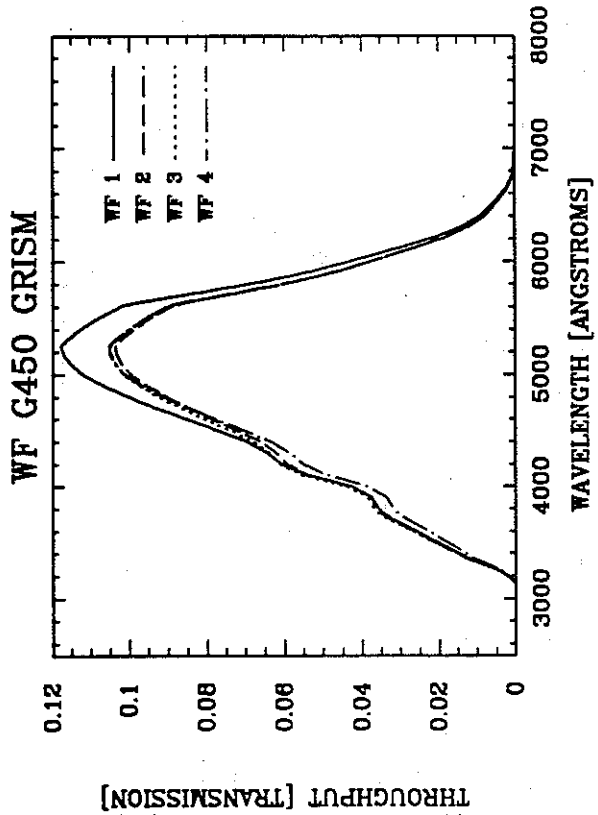

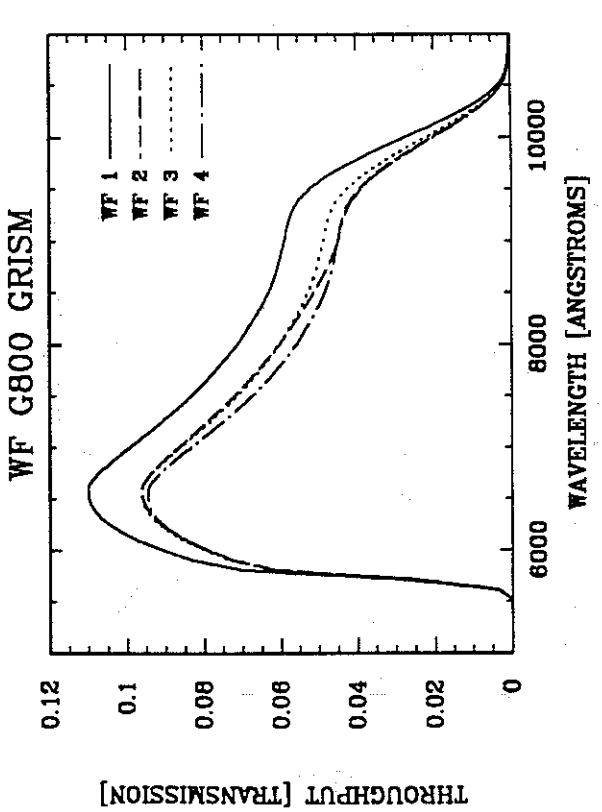

Table QEXPOSURE–WFPC

Field name	Type	Rule for Value		
CONTROL_ID	C*5	NØØØY	if	Mode = UVFLOOD
		YØØØY	if	Targname = [KSPOTS | INTFLAT | DARK | BIAS]
		YFAØY		otherwise
MODE		AREA	if	SUM = 2 X 2
		FULL		in all other cases.
ISZEROFR	C*3	YES		Targname = BIAS
		NO		otherwise
CAMERA	C*10	WF		Config = WFC
		PC		Config = PC
FILTER1	I*2	47	if	logsheet Col. 3 = DARK
				otherwise see WFPC Filter Table below
FILTER2	I*2	38	if	logsheet Col. 3 = DARK
				otherwise see WFPC Filter Table below
DATA_VOLUME	R*4			= SHP + SDP, See Algorithm for Data Volume below

Table WFPC Filter

commanding - sets filters for darks as F1083 + F437N

Find the filter being used (Column 7 from Exposure Logsheet) and fill in the corresponding number from the table.

FILTER #: FILTER :	1 F122M	2 F157W	3 F194W	4 F230W	5 F284W	6 F336W	7 F439W	
	8 F569W	9 F675W	10 F791W	11 F850LP	12 F606W	13 F725LP	14 F128LP	
	15 F673N	16 F8ND	17 POL0	18 POL60	19 POL120	20 G200L	21 G450L	22 G800L
	23 F702W	24 F368M	25 F413M	26 F622W	27 F492M	28 F547M	29 F555W	30 F648M
	31 F718M	32 F814W	33 F875M	34 F785LP	35 F1042M	36 F375N	37 F469N	
	38 F437N	39 F487N	40 F502N	41 F517N	42 F5888N	43 F631N	44 F656N	
	45 F664N	46 F889N	47 F1083N	48 F658N				

f122m 1
f1281p 14
f157w 2
f194w 3
f230w 4
f284w 5
f336w 6
f368m 24
f375n 36
f413m 25
f437n 38
f439w 7
f469n 37
f487n 39
f492m 27
f502n 40
f517n 41
f547m 28
f555w 29
f569w 8
f588n 42
f606w 12
f622w 26
f631n 43
f648m 30
f656n 44
f658n 48
f664n 45
f673n 15
f675w 9
f702w 23
f718m 31
f725lp 13
f785lp 34
f791w 10
f814w 32
f850lp 11
f875m 33
f889n 46
f8nd 16
f1042m 35
f1083n 47
g200l 20
g450l 21
g800l 22
pol0 17
pol60 18
pol120 19